ALMA MATER STUDIORUM – UNIVERSITÀ DI BOLOGNA
ARCES – ADVANCED RESEARCH CENTER ON ELECTRONIC SYSTEMS

Design and Computation of Warped Time-Frequency Transforms

Salvatore Caporale

SUPERVISOR
Professor Guido Masetti

COORDINATOR
Professor Claudio Fiegna

EDITH – EUROPEAN DOCTORATE ON INFORMATION TECHNOLOGY
JANUARY 2006 – DECEMBER 2008
XXI CYCLE – ING-INF/01

"If you try and take a cat apart to see how it works,
the first thing you have on your hands
is a non-working cat."

Douglas Adams

Preface

This work mainly concerns *warping* techniques for the manipulation of signals. Our approach on this topic will be guided by theoretical issues rather than experimental ones. So, we will not dedicate much space to explain what *warping* is in a practical sense. In order to compensate the excess of theory which will be experienced by the reader in the this work, here we want to introduce some basic concepts behind frequency warping in an easy way.

Generically, a signal is described as a measurable quantity which is able to vary through time and over space. Although warping could be applied on any kind of signals, as an example we consider those signals which are intrinsically perceived by human visual observation, i.e. images. As a signal has to be measured, the visual information related to a subject which produces an image can be stored in many ways, determining a different kind of measure. In modern electronic sensor devices are employed, in traditional cameras light was stored by a chemical reaction and in humans the storage process is devolved upon biological sensors. Referring to humans, the measurement is not completely carried out by the eyes, since the light information is reported to the brain which makes some further elaborations before memorizing it in synapses.

Since signals concern the transport of information, or rather the communication through time and space, before the inven-

Figure 1: Escher's lithograph "Print Gallery" (1956). M. C. Escher "Prentententoonstelling" © 2003 Cordon Art-Baarn-Holland. All rights reserved.

tion of cameras humans have developed alternative methods to store and communicate images beyond the time and place where they were living. Of course we are talking about *figurative art*. The measurement performed by a man and reported on a painting or any other kind of figurative representation shows the importance of the way the perceived information is weighted according to specific patterns which are enclosed in the measurement *instrument*. Figurative art taught that, since there is not a single way to represent reality, then there is not a single way to observe reality. Works of art are always affected by a kind of signal processing, including simple filtering operations or complicated non-linear effects. Furthermore, we can notice that during the last centuries, figurative art deliberately abandoned the aim of giving a faithful representation of reality and expressed the willing of going beyond what can be directly experienced by human senses.

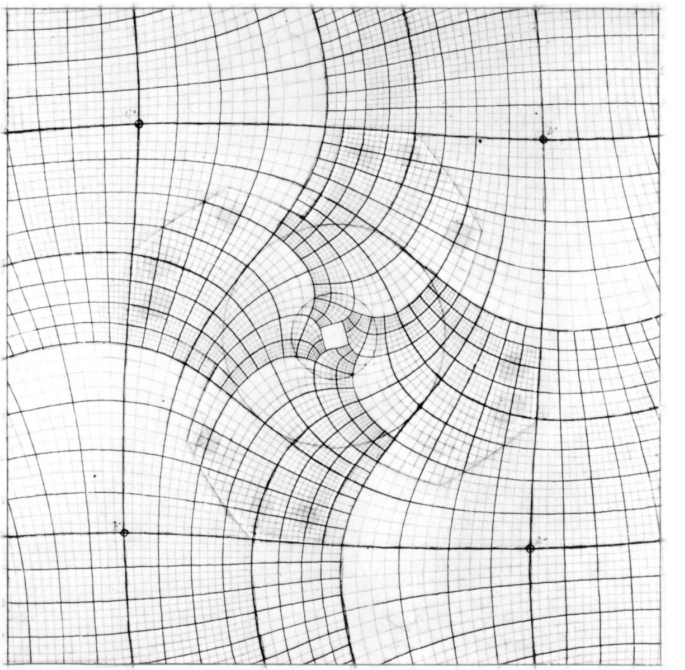

Figure 2: Warping Grid used by Escher to draw the "Print Gallery".

In this background, we consider the work of M. C. Escher. In his prints he took advantage of some concepts akin to mathematics, like self-reference, infinite and recursive processes. In particular, recursion is the main concept in his print titled the "Print Gallery", which is reported in figure 1. An accurate description of the mathematical structure of this work can be found in [1]. The print have been drawn starting from an *unwarped* image, representing a man observing a print which illustrates himself watching the same print recursively (this recursion is called Droste effect). On this image, a warping have bee applied according to grid which is shown in figure 2. The new warped image is created by making the tales of a square grid built on the original image correspond to the tales on the new grid. The performed operation is more than a deformation, since the grid is designed such that it contains a progressive scaling operation which makes the recursive spaces reconnect together. But apart from the scaling, we want to focus on the global effect that the

author's point of view has given to the content. Thanks to the grid, the tales of the image have been re-weighted according to a new sampling, so that some details which were not visible and recognizable in the original version have been increased in importance. A very interesting consideration to be done is that trough the warping operation there is no increase in the global information contained in the picture. Instead, the way the space of observation (the square frame) is split among the various part of the image has been modified.

It is quite intuitive that the problem of recovering the original image, which has been treated in [1], is actually the same problem as drawing the warping image. In fact, one can assume that the image in figure 1 is the original one, and then draw a new image through a grid which nullify the effect of the grid in figure 2.

Through this example, we have already illustrated some of the basic properties and concepts behind the warping technique. Possible aims of such an operation can be easily imagine by comparison with the shown example. For instance, one could need to exalt some parts of a signal despite to others in order to perform an accurate feature extraction. This approach can be categorized as a *direct* application of a warping technique, since the starting point is the unmodified signal. Otherwise, it could be necessary to remove the effects of an acquisition process which weights non-uniformly the different parts of the incoming signal. This approach would be labeled as an *inverse* use of a warping technique, since the starting point is an already warped signal. As we suggested before, there is an intrinsic duality between the direct and the inverse approach.

The possibility of recovering the original signal by the warped one, that is the capability of define an inverse unwarping which exactly inverts the direct one, is a very important issue when dealing with warping technique from a mathematical point of view. Invertibility is the major problem which will be considered in this work. Furthermore we will cope with the way the warping operation should to be designed, which means, by comparison with the Escher's print example, what kind of curves should compose the grid in figure 2.

We finally report other hints suggested from Escher's lithograph. Although these consists in conceptual observations rather than mathematical ones, they reveal to make sense in hindsight. We notice that the center of 1 was left unpainted. We

also learn from [1] that the unwarped picture used by Escher was not complete, since the unpainted spot gives rise to an empty spiral. These observations can be translated to our perspective in the following metaphorical meaning. When warping a signal from a finite-dimensional domain to another finite-dimensional one (i.e. a domain having an upper limited resolution), some information is necessarily discarded. Maybe a perfect reconstruction could be achieved anyway, but it involves something more than merely inverting the steps employed for warping.

Contents

Introduction

During the last years the relevance of time–frequency transformations has widely grown in signal processing. These techniques are commonly addressed to give a new representation of a source signal. A time-frequency transformation could be adaptively defined in order to match the way the information is recorded in the source signal. Alternatively, it could be designed to obtain a sparse representation for compression or denoising applications. In some cases the two purposes could match, i.e. the sparse representation also conveys some of the source characteristics and implements a feature extraction. So, the ability of generating a flexible tiling of the time-frequency plane is a major issue. Many transformations have been introduced in order to accomplish this task, including the short time Fourier transform, the wavelet transform, filter banks and all their variations and mutual combination addressed to generalize their intrinsic characteristics [2, 3]. Nevertheless, such transformations have some restrictive properties which make them not suitable in some applications. In particular, some requirements, like fast computation and orthogonality, limit the degrees of freedom in choosing the proper time-frequency representation.

In order to approach the aim of an arbitrary time-frequency tiling, the application of a preliminary invertible transformation to reshape the frequency axis can be considered [4, 5]. This transformation is referred as frequency warping. The feature

defining how the frequency axis is reshaped is the frequency warping map.

The application of frequency warping as a way for generalizing existing time-frequency transforms has been introduced some years ago in [6–8]. However, from a mathematical point of view it has been previously modeled in many ways.

In [9, 10] frequency warping has been described as a nonstationary resampling in time of the input signal performed by sampling the outputs of an all-pass filter chain. The resulting transformation, close to the Laguerre transform, suffers of strong limitations in terms of allowed frequency maps. In fact, Laguerre maps are obtained by considering the composition between a sigmoidal function, actually the *arctangent* function, and its inverse multiplied by a scale parameter. This parameter represents the only degree of freedom and might not be sufficient as a design parameter in many applications. Later, frequency warping has been modeled as a projection on a set of frequency and amplitude modulated functions [11], but as far as applications are concerned, it was not taken advantage of this model and only Laguerre functions were applied.

From a computational point of view, frequency warping can be modeled as the composition of an inverse Fourier transform and a warped Fourier transform, which can be can be computed by a nonuniform Fourier transform [12–15]. This approach is more general since it allows to design the warping map in an arbitrary way, potentially perfectly suited to the target application. However, being based on discrete-frequency operations, it could suffer from inaccuracy.

Moreover, it would be desirable to define frequency warping as an orthogonal operator, so that, if a further orthogonal transformation is applied in cascade, the whole one would still be orthogonal. However, as an intrinsic feature, frequency warping always returns a redundant representation of the source signal. For this reason, the requirement of making it be orthogonal can not be fulfilled. Nevertheless, if proper defined, it can still be accurately inverted by applying the adjoint operator of the direct transform. This property makes frequency warping belong to the class of *frames* [16, 17].

In this work we deal with the problem of defining frequency warping transforms such that the frequency map can be designed in a flexible way, like by a piecewise approach, and the property of being inverted by the adjoint operator is satisfied up

to a predetermined accuracy. In particular, we focus on how the features of the frequency warping maps affect the reconstruction accuracy, so that designing rules can be inferred for getting an optimal design. Arbitrary maps could have singularities, hence, for the sake of generality, non-smooth functions are considered.

Our ultimate goal is to introduce a mathematical model and a fast and accurate computation algorithm for frequency warping transforms referred to non-smooth frequency map. This result is obtained by extending the modeling based on nonuniform Fourier transform by the introduction of an aliasing suppression technique [18–20].

The work is organized in three parts. Part I is dedicated to the introductions of target operators and transforms. In particular chapter 1 has a strict and rigid mathematical approach, while chapter 2 focuses on more practical issues. In this part there is no original contribution but the point of view and the mathematical setting, which is actually the base for successive further developments.

Part II represents the core of the core of the entire work. Basically, it concerns the computational model for a practical use of the operators which have been theoretically introduced in part I. More precisely, an original contribution for the computation of nonuniform Fourier transform is given in chapter 3 which is complementary to the factorization of the aliasing operator in chapter 4, both involved in the modeling of frequency warping. Moreover, a analytical characterization of frequency warping in terms of reconstruction accuracy is given in chapter 5. Most of the contents of this part represents an original and innovative contribution.

Part III presents refers to the field of ultrasonic waves propagation, where frequency warping has been efficiently applied as it perfectly matches the physical behavior of dispersive mode propagation. Chapter 6 explains how the mathematical model is transposed over the physical problem and gives some details about the experimental setup. Although the application of frequency warping on this topic is still in a preliminary stage, it reveals to be very promising and innovative.

The entire work, considered from a global perspective, concerns a wide range of problems and therefore employs a lot of mathematics. Although an effort has been done in order to uniform the notation and the conventions about the representation of signals and operators, the work is not completely

homogeneous. Moreover, it has been tried to limit the interdependencies among the different parts and chapters, nevertheless they maintain a certain degree of correlation. So it is strongly recommended to approach the reading in a linear fashion from the beginning to the end.

Part

I

Theoretical Issues on Warped Transforms

Chapter

1 Fourier and Warping Operators

This chapter will present the notation which will be used in the rest of the work. More in details, we will refer to either time-continuous and time-discrete signals and we will provide definitions for mathematical operators applied to both of them. In particular, we will mainly deal with time-frequency operators, so a major space will be dedicated to fixing the notation and the conventions about the Fourier transform. Finally we will introduce the frequency warping operator, which will be the starting point for the further developments of the rest of the work.

Both Fourier and warping operator will be presented in the continuous-time, discrete-time continuous-frequency and discrete-time discrete-frequency cases. A particular attention will be dedicated to invertibility and reconstruction accuracy. In this framework we will recall the sampling theorem and the duality between time and frequency domains. As a conclusion, we will introduce a additive decomposition of the time-discrete frequency warping operator in its frequency sampled approximation and an aliasing term. Both these operators will be deeply discussed in next chapters.

As a convention, signals will be represented in lowercase italic letters, while operators will be represented by boldface uppercase letters. We deliberately introduce an ambiguity between the representation of the operators and their kernels.

1.1 Fourier Operators

We start by reviewing the Fourier transform and its main properties, which are supposed to be well-known to the reader. So, the purpose of this section is to present an approach based on operators for the derivation and description of Fourier transforms. This may be useful to suggest a comparison to linear algebra, which will be deeply exploited in this work. Moreover, this short summary on Fourier transforms may serve as an exercise to get acquire familiarity with the operators approach.

From a practical point of view, we first introduce the continuous Fourier transform, then we derive the Fourier transform for discrete-time signals and finally the discrete transform in both time and frequency. The aim is to maintain a reference to the continuous operator in the definition of the discrete transforms, so that, when warping will be applied, the derivation to discrete case will be straightforward.

1.1.1 Continuous-Time Operators

In order to illustrate this representation, we start by considering the Fourier $\mathbf{F}$ transform applied on a continuous signal s:

$$\mathbf{F} : L^2(\mathbb{R}) \to L^2(\mathbb{R}),\ s(t) \mapsto \hat{s}(f) = \int_{\mathbb{R}} s(t) e^{-j2\pi tf} dt$$

so, the operator kernel is simply given by:

$$\mathbf{F}(f,t) = e^{-j2\pi tf}.$$

In compact operator notation the Fourier transform is represented by:

$$\hat{s} = \mathbf{F}s$$

The adjoint operator will be represented by the † subscript:

$$\mathbf{F}^\dagger : L^2(\mathbb{R}) \to L^2(\mathbb{R}),\ \hat{s}(f) \mapsto [\mathbf{F}^\dagger s](t) = \int_{\mathbb{R}} \hat{s}(f) e^{-j2\pi tf} df$$

and the operator kernel is obtained by complex conjugating F. The Fourier operator is unitary, i.e. its inverse operator is given by the adjoint one:

$$\mathbf{F^{-1}} = \mathbf{F}^\dagger$$

which is easily verified by considering:

$$[\mathbf{F}^\dagger \mathbf{F}](t,\tau) = \int_{\mathbb{R}} e^{-j2\pi tf} e^{j2\pi\tau f} = \int_{\mathbb{R}} e^{-j2\pi(t-\tau)f} = \delta(t-\tau)$$

that, in compact notation, is:

$$\mathbf{F}^\dagger \mathbf{F} = \mathbf{I}$$

where $\mathbf{I}$ is the identity operator.

1.1.2 Nyquist Theorem Revisited

Now we want to consider discrete-time signals. In order to do this, we first introduce the sampling operator $\mathbf{D}$ (where D stays for *Delta*):

$$\mathbf{D} : L^2(\mathbb{R}) \to \ell^2(\mathbb{Z}),\ s(t) \mapsto [\mathbf{D}s](n) = \int_{\mathbb{R}} s(t)\delta(t-n)dt$$

whose kernel is simply given by:

$$\mathbf{D}(n,t) = \delta(t-n).$$

In order to transform a discrete-time signal, the Fourier operator has to be sampled as well, so that we should consider:

$$[\mathbf{F}\mathbf{D}^\dagger](t,f) = \int_{\mathbb{R}} e^{-j2\pi tf}\delta(t-n)dt = e^{-j2\pi nf}.$$

Now we suppose that the considered signal is band-limited, with bandwidth equal to 1/2, then the sampling operation does not cause a loss in information. Sampling just cause a periodic repetition in the frequency domain. Let us show this well-known property by the operator notation. The sampling can be represented in the frequency domain as:

$$\mathbf{F}\mathbf{D}^\dagger \mathbf{D}s$$

where the operator $\mathbf{D}^\dagger\mathbf{D}$ can be explicitly computed:

$$[\mathbf{D}^\dagger\mathbf{D}](t,\tau) = \sum_{n\in\mathbb{Z}} \delta(t-n)\delta(\tau-n) = \delta(t-\tau)\sum_{n\in\mathbb{Z}}\delta(t-n)$$

which is actually a diagonal operator whose diagonal is given by a Dirac comb. We remind that the Dirac comb can be equivalently represented by its Fourier series:

$$\sum_{n\in\mathbb{Z}}\delta(t-n) = \sum_{n\in\mathbb{Z}} e^{j2\pi nt}$$

so we get:

$$\begin{aligned}[\mathbf{FD}^\dagger\mathbf{D}s](f) &= \int_{\mathbb{R}} e^{-j2\pi tf} \sum_{n\in\mathbb{Z}} e^{j2\pi nt} s(t)dt \\ &= \sum_{n\in\mathbb{Z}} \int_{\mathbb{R}} e^{-j2\pi t(f-n)} s(t)dt = \sum_{n\in\mathbb{Z}} \hat{s}(f-n).\end{aligned}$$

We can introduce the periodic repetition operator $\mathbf{R}$ such that:

$$\mathbf{R} : L^2(\mathbb{R}) \to L^\infty(\mathbb{R}),\ \hat{s}(\xi) \mapsto [\mathbf{R}s](f) = \int_{\mathbb{R}} \hat{s}(\xi) \sum_{\mathbb{Z}} \delta(\xi - f + n)$$

whose kernel is represented by:

$$\mathbf{R}(f,\xi) = \sum_{n\in\mathbb{Z}} \delta(\xi - f + n).$$

This equivalence can be finally set:

$$\mathbf{FD}^\dagger\mathbf{D} = \mathbf{RF}$$

which means that in order to invert the sampling operation we must be able to invert the periodic repetition. Normally periodic repetition is not an invertible operation, unless the considered signal is band-limited. In particular we are interested in baseband signals, so we just suppose that the input signal has non-zero amplitude only in the interval $[-½, ½]$. By this hypothesis, we can invert the periodic repetition by windowing the spectrum with a rectangular filter $\mathbf{H}$:

$$\mathbf{H}(f,\xi) = \delta(f-\xi)[H(\xi+1/2) - H(\xi-1/2)]$$

where H is the Heaviside function. So, in case of baseband band-limited signals, the operator:

$$\mathbf{F}^\dagger\mathbf{HFD}^\dagger\mathbf{D}$$

behaves like an identity operator. In order to specify this result, we first consider:

$$\begin{aligned}[\mathbf{F}^\dagger\mathbf{HF}](t,\tau) &= \int_{\mathbb{R}} e^{j2\pi ft}[H(f+1/2) - H(f-1/2)]e^{-j2\pi f\tau} df \\ &= \int_{-½}^{½} e^{j2\pi f(t-\tau)} df \\ &= \operatorname{sinc}(t-\tau)\end{aligned}$$

and then define the resulting operator as:

$$\mathbf{S}(t,\tau) = \mathrm{sinc}(t-\tau)$$

so that, the global operation performed on the input signal s can be represented as:

$$\mathbf{SD}^\dagger\mathbf{D}.$$

Now we notice that $\mathbf{SD}^\dagger$ can be written as an interpolator:

$$\mathbf{SD}^\dagger(t,n) = \int_{\mathbb{R}} \mathrm{sinc}(t-\tau)\delta(\tau-n)d\tau = \mathrm{sinc}(t-n).$$

It results that this inversion procedure gives as output the input signal samples interpolated by a sinc function, so it recovers the original signal if the signal could actually be expressed as a linear combination of shifted sinc functions. Finally we consider this equality:

$$\mathbf{SD}^\dagger\mathbf{DS} = \mathbf{F}^\dagger\mathbf{HRHF}.$$

Since $\mathbf{HRH}$ is equal to $\mathbf{H}$, we conclude that:

$$\mathbf{SD}^\dagger\mathbf{DS} = \mathbf{S}. \tag{1.1}$$

which means that, given a generic signal, the subspace identified by $\mathbf{S}$ can be recovered after sampling by applying $\mathbf{SD}^\dagger$.

1.1.3 Discrete-Time Fourier Operators

After having explained how to pass from continuous to discrete domain, we can deal with discrete-time signals. So, from this point forward, s will represent a sequence in $\ell^2(\mathbb{Z})$. The Fourier transform has to be redefined for the new input domain. In particular, it could be desirable to define such that the inverse operator is equal to the transpose one.

Let us apply a sampling on both sides of equation (1.1):

$$\mathbf{DSD}^\dagger\mathbf{DS} = \mathbf{DS}$$

which tells us that the subspace identified by $\mathbf{DS}$ is invariant respect to the application of $\mathbf{DSD}^\dagger$. Since we consider as input $\ell^2(\mathbb{Z})$, which is generated by $\mathbf{DS}$, the operator to evaluate is $\mathbf{DSD}^\dagger$:

$$\begin{aligned}
[\mathbf{DSD}^\dagger](m,n) &= \int_{\mathbb{R}} \delta(t-n) \int_{\mathbb{R}} \mathrm{sinc}(t-\tau)\delta(\tau-m)d\tau dt \\
&= \int_{\mathbb{R}} \delta(t-n)\mathrm{sinc}(t-m)dt \\
&= \mathrm{sinc}(n-m)
\end{aligned}$$

which means that $\mathbf{DSD}^\dagger$ is equal to the identity operator respect to $\ell^2(\mathbb{Z})$:

$$\mathbf{DSD}^\dagger = \mathbf{I}$$

therefore the Fourier operator and its adjoint can be put after $\mathbf{D}$:

$$\mathbf{DSF}^\dagger\mathbf{FD}^\dagger = \mathbf{I}.$$

The direct Fourier transform for discrete-time signals can be defined as follows:

$$\mathbf{FD}^\dagger : \ell^2(\mathbb{Z}) \to L^\infty(\mathbb{R}),\ s(n) \mapsto \hat{s}(f) = \sum_{n\in\mathbb{Z}} s(n)e^{-j2\pi nf} \quad (1.2)$$

whose kernel is merely given by:

$$[\mathbf{FD}^\dagger](f,n) = e^{-j2\pi nf}$$

The inverse operator can be defined by:

$$[\mathbf{FD}^\dagger]^{-1} = \mathbf{DSF}^\dagger = \mathbf{DF}^\dagger\mathbf{H}$$

such that:

$$[\mathbf{FD}^\dagger]^{-\mathbf{1}} : L^2(\mathbb{R}) \to \ell^2(\mathbb{Z}),\ \hat{s}(f) \mapsto s(n) = \int_0^1 \hat{s}(f)e^{j2\pi nf}dt$$

where the interval $[0,1]$ has been equivalently considered rather than $[-\frac{1}{2},\frac{1}{2}]$.

We point out that, in the inverse operator, the purpose of operator $\mathbf{DS}$ after operator $\mathbf{F}^\dagger$ is to reduce a Dirac comb of this kind:

$$\sum_{n\in\mathbb{Z}} s(n)\delta(t-n)$$

whose energy is infinite, to a finite energy sequence trough substituting the Dirac impulses by Kronecker symbols. So the Fourier transform of a sequence is intrinsically periodic, the windowing operation performed by operator $\mathbf{H}$ accomplishes only computational needs. For this reason, we prefer to represent the Fourier transform of a discrete-time signal and its inverse by the operator described above.

Nevertheless, it could be convenient as well to define the Fourier transform so that the inverse operator is given by its adjoint. In order to do this, we consider:

$$\mathbf{DF}^\dagger\mathbf{HFD}^\dagger = \mathbf{DF}^\dagger\mathbf{HHFD}^\dagger = [\mathbf{DF}^\dagger\mathbf{H}][\mathbf{HFD}^\dagger]$$

and since $\mathbf{H}^\dagger = \mathbf{H}$, we could set:

$$\mathbf{HFD}^\dagger : \ell^2(\mathbb{Z}) \to L^2([0,1)),\ s(n) \mapsto \hat{s}(f) = \sum_{n\in\mathbb{Z}} s(n)e^{-j2\pi nf}dt \tag{1.3}$$

as an alternative definition of Fourier transform. The kernel is obviously the same as in the previous definition, since operator $\mathbf{H}$ only affects the codomain. Independently on the adopted definition, the discrete-time operator will be referred as $\mathbf{F_D}$.

From a practical point of view, considering the entire frequency axis as output domain rather than a single period, does not imply substantial differences. Instead, from a theoretical point of view, it will have important implications when frequency warping will be applied. In fact, when an operator is applied on the frequency domain, even if the axis is restricted to a single period, the periodicity has to be taken into account for rightly modeling the effects of the considered operator and potentially for designing it according to some optimality criteria.

1.1.4 Discrete Fourier Operator

Now we want to introduce discrete operators in both time and frequency domains. The approach which will be followed is quite the same as the one used to introduce discrete-time operators.

In time domain we considered a sampling step equal to 1. Because of it, the frequency domain period is equal to 1 as well. So, it is quite evident that in the frequency domain we must consider a sampling step smaller than 1. Moreover, in order to maintain periodicity, the sampling step must be contained in the period an integer number of times. Therefore we will assume that the sampling step is equal to $1/N$, or rather the period is sampled in N different points. The sampling operator has to modified so that it performs this task and will be represented as $\mathbf{D}_N$:

$$\mathbf{D}_N : L^\infty(\mathbb{R}) \to \ell^\infty(\mathbb{R}),$$
$$\hat{s}(f) \mapsto [\mathbf{D}_N\hat{s}](k) = \int_{\mathbb{R}} \hat{s}(f)\delta(f - k/N)df$$

whose kernel is given by:

$$\mathbf{D}_N(k, f) = \delta(f - k/N).$$

Now, we apply this sampling operator on the left of the Fourier operator and on the right of the adjoint one:

$$\mathbf{DSF}^\dagger \mathbf{D}_N^\dagger \mathbf{D}_N \mathbf{F}\mathbf{D}^\dagger. \tag{1.4}$$

The operator $\mathbf{D}_N^\dagger \mathbf{D}_N$ roughly behaves like the operator $\mathbf{D}^\dagger \mathbf{D}$, that is:

$$\begin{aligned}[\mathbf{D}_N^\dagger \mathbf{D}_N](f,\xi) &= \sum_{k\in\mathbb{Z}} \delta(f-k/N)\delta(\xi-k/N) \\ &= \delta(f-\xi)\sum_{k\in\mathbb{Z}} \delta(f-k/N)\end{aligned}$$

again, the Dirac comb can be represented by:

$$\sum_{k\in\mathbb{Z}} \delta(f-k/N) = N\sum_{k\in\mathbb{Z}} e^{j2\pi fkN}$$

so that, from $\mathbf{F}^\dagger \mathbf{D}_N^\dagger \mathbf{D}_N \mathbf{F}$ we get:

$$\begin{aligned}[\mathbf{F}^\dagger \mathbf{D}_N^\dagger \mathbf{D}_N \mathbf{F}](t,\tau) &= \int_{\mathbb{R}} e^{j2\pi ft} N\sum_{k\in\mathbb{Z}} e^{j2\pi fkN} e^{-j2\pi f\tau} \\ &= N\sum_{k\in\mathbb{Z}} \int_{\mathbb{R}} e^{j2\pi f(t-\tau+kN)} = N\sum_{k\in\mathbb{Z}} \delta(t-\tau+kN).\end{aligned}$$

The resulting operator performs a repetition with step equal to N, In order to complete the chain (1.4), we still miss the $\mathbf{D}^\dagger$ operator on the right and the **DS** operator on the left. By applying $\mathbf{D}^\dagger$ we get:

$$\begin{aligned}[\mathbf{F}^\dagger \mathbf{D}_N^\dagger \mathbf{D}_N \mathbf{F}\mathbf{D}^\dagger](t,n) &= \int_{\mathbb{R}} N\sum_{k\in\mathbb{Z}} \delta(t-\tau+kN)\delta(\tau-n)d\tau \\ &= N\sum_{k\in\mathbb{Z}} \delta(t-n+kN)\end{aligned}$$

while by applying $[\mathbf{DS}](m,t) = \mathrm{sinc}(t-m)$ on the right we get:

$$\begin{aligned}&[\mathbf{DSF}^\dagger \mathbf{D}_N^\dagger \mathbf{D}_N \mathbf{F}\mathbf{D}^\dagger](m,n) = \\ &\int_{\mathbb{R}} \mathrm{sinc}(t-m) N\sum_{k\in\mathbb{Z}} \delta(t-n+kN)dt = N\sum_{k\in\mathbb{Z}} \mathrm{sinc}(n-m-kN)\end{aligned}$$

where the sinc functions, being sampled on integer values, behaves like Kronecker symbols. The obtained operator represents a discrete periodic repetition which will be referred as $\mathbf{R}_N$:

$$\mathbf{R}_N = N^{-1}\mathbf{DSF}^\dagger \mathbf{D}_N^\dagger \mathbf{D}_N \mathbf{F}\mathbf{D}^\dagger.$$

As expected, the sampling in the frequency domain causes a periodic repetition in discrete time domain. In order to avoid loss in information, the following operator should maintain the input signal unchanged:

$$\mathbf{H}_N\mathbf{R}_N$$

where $\mathbf{H}_N$ is suitable rectangular discrete-time window of length equal to N. So, the following statement is surely satisfied:

$$\mathbf{H}_N\mathbf{R}_N\mathbf{H}_N s = \mathbf{H}_N s$$

and we infer that the signal must be time-limited to an interval equal or smaller than N samples.

By considering as input domain the space generated by $\mathbf{H}_N$, we can now define the discrete Fourier transform as:

$$\mathbf{D}_N\mathbf{F}\mathbf{D}^\dagger : \mathbb{R}^N \to \ell^\infty(\mathbb{Z}),\ s(n) \mapsto \hat{s}(k) = \sum_{n\in\mathbb{Z}_N} s(n)e^{-j2\pi nk/N}$$

where $\mathbb{Z}_N$ is a set of N consecutive integers. The inverse transform is expressed by:

$$[\mathbf{D}_N\mathbf{F}\mathbf{D}^\dagger]^{-1} = N^{-1}\mathbf{D}\mathbf{S}\mathbf{F}^\dagger\mathbf{D}_N^\dagger = N^{-1}\mathbf{D}\mathbf{F}^\dagger\mathbf{H}\mathbf{D}_N^\dagger$$

and it acts on the discrete Fourier transformed signal $\hat{s}$ as follows:

$$[\mathbf{D}_N\mathbf{F}\mathbf{D}^\dagger]^{-1} : \ell^\infty(\mathbb{Z}) \to \mathbb{R}^N,$$
$$\hat{s}(k) \mapsto s(n) = N^{-1}\sum_{k\in\mathbb{Z}_N} \hat{s}(k)e^{j2\pi nk/N}.$$

Here, the set $\mathbb{Z}_N$ is not necessarily the same set used in the direct transform. A standard choice is to consider for both the sets:

$$\mathbb{Z}_N = \{0, 1, \ldots, N-1\}$$

but, as said before, other choices are allowed.

Again, we could redefine the direct Fourier operator such that the output domain is limited in frequency, i.e. $\mathbb{R}^N$:

$$\mathbf{D}_N\mathbf{H}\mathbf{F}\mathbf{D}^\dagger : \mathbb{R}^N \to \mathbb{R}^N,\ s(n) \mapsto \hat{s}(k) = \sum_{n\in\mathbb{Z}_N} s(n)e^{-j2\pi nk/N}$$

whose inverse is represented by its adjoint multiplied by the constant being the input dimension:

$$[\mathbf{D}_N\mathbf{H}\mathbf{F}\mathbf{D}^\dagger]^\dagger[\mathbf{D}_N\mathbf{H}\mathbf{F}\mathbf{D}^\dagger] = N\mathbf{I}_N$$

where $\mathbf{I}_N$ is the identity operator for a $\mathbb{R}^N$.

The discrete Fourier transform operator will be represented as $\mathbf{F}_{\mathbf{D}_N\mathbf{D}}$, either if the codomain is the entire frequency axis or a single period.

1.2 Frequency Warping Operators

In this section we introduce the warping operators. The presentation follows the flow which has been used for the Fourier operators. So, we start from the continuous case, then introduce the sampling of the time axis and finally derive the the sampling of both time and frequency axis. Preliminarily, the warping of a generic axis as an intrinsic transformation will be considered, then it will be transposed to the frequency axis. Even if the warping is performed in the frequency domain, the frequency warping operator is defined so that it acts in the time-domain. So, the introduced deformation is not directly observable and recognizable in the time-domain.

1.2.1 Unitary Operators

Roughly speaking, a unitary operator is an operator such that its inverse is given by the adjoint one. Unitariness is always a desirable property for an operator, since it carries out some advantages which can be very important in signal processing. More in details, an operator $\mathbf{U}$ is said to be unitary the following three condition are satisfied:

- Linearity.
  Given two constants $a, b \in \mathbb{R}$ and two functions or vectors s_1 and s_2, linearity is satisfied if:
  $$\mathbf{U}[as_1 + bs_2] = a\mathbf{U}s_1 + b\mathbf{U}s_2$$
- Suriectivity.
  This property, also said non-singularity, ensures that no input function is transformed in the 0 function:
  $$\mathbf{U}s = 0 \iff s = 0$$
- Isometry.
  This property consists in preserving distances:
  $$\|\mathbf{U}s\| = \|s\|$$

Linearity is normally satisfied for most of the operators which are used in time-frequency analysis. An example of operator which does not verify the surjectivity property is a filter, which by definition nullify all the information carried by specified functions or vectors. Examples of transformations which fulfill the isometry property are the time-shift, the frequency-shift or modulation and the scaling.

By considering the isometry property, for $\|\mathbf{U}s\|$ we get:

$$\|\mathbf{U}s\| = [\mathbf{U}s]^\dagger[\mathbf{U}s] = s^\dagger\mathbf{U}^\dagger\mathbf{U}s$$

so that, the isometry is satisfied if and only if:

$$\mathbf{U}^{-1} = \mathbf{U}^\dagger. \tag{1.5}$$

which is the property announced at the beginning. We remind that in the previous section, when we defined the Fourier operators, we always provided a definition satisfying the unitary property. As far as warping is concerned, we will attempt to the same as for Fourier operators.

Since the norm of s is given by the square root of the scalar product between s and itself, it follows that the scalar product between two functions or vectors s_1 and s_2 is invariant respect to the application of a unitary operator:

$$[\mathbf{U}s_1]^\dagger[\mathbf{U}s_2] = s_1^\dagger\mathbf{U}^\dagger\mathbf{U}s_2 = s_1^\dagger s_2.$$

This formulation suggests the way a unitary operator can be used. Let us suppose to have another unitary operator, for example the Fourier operator $\mathbf{F}$. The composed operator $\mathbf{FU}$ is still unitary, since:

$$[\mathbf{FU}]^\dagger[\mathbf{FU}] = \mathbf{U}^\dagger\mathbf{F}^\dagger\mathbf{FU} = \mathbf{U}^\dagger\mathbf{U} = \mathbf{I}.$$

So, the analysis performed by $\mathbf{F}$ can be modified through the application of $\mathbf{U}$, which could be applied either to the right $\mathbf{F}$ or to left of the input function or vector. The first option would involve a modification on the operator $\mathbf{F}$, so it may be not completely painless. Therefore, it should be much more convenient to apply it preliminarily on the input signal. We point out that, if the considered operator performs for example a shift towards left and we want to obtain such a modification on the bases vectors, the transformation to be applied on the signal is the inverse one, or rather the adjoint one, In fact, if we force $\mathbf{U}$ to act on $\mathbf{F}$ *rows* from the right, we get:

$$\mathbf{FU}s = [[\mathbf{FU}]^\dagger]^\dagger s = [\mathbf{U}^\dagger\mathbf{F}^\dagger]^\dagger s. \tag{1.6}$$

1.2.2 Continuous Warping Operator

Here we want to introduce the concept of deformation of a continuous function. Intuitively, to get a deformation of a function one has to introduce a deformation on its axis. This means that we must set a function w, such that it maps the old axis x to the new axis $w(x)$:

$$w : \mathbb{R} \to \mathbb{R}, \quad x \mapsto w(x).$$

In previous sections we often focused on invertibility. To get an invertible warping operator, the function w must be an invertible function, that is:

$$\dot{w} > 0 \quad a.e. \quad \Rightarrow \quad \exists w^{-1},\ w^{-1}(w(x)) = x \tag{1.7}$$

where $\dot{w}$ represents the first derivative of w while w^{-1} represents the functional inverse. Starting from w, we introduce the transformation which substitutes the axis x of an input function $s(w)$ by $w(x)$. This is actually the composition of s and w:

$$\mathbf{W}s = [s \circ w](x) = s(w(x)).$$

The kernel of this operator can be described as follows:

$$\mathbf{W}(x, y) = \delta(w(x) - y)$$

in fact:

$$[\mathbf{W}s](x) = \int_{\mathbb{R}} \delta(w(x) - y)s(y)dy = w(s(x)).$$

This operator is candidate to become the warping operator. To be elected, it must be linear, surjective and isometric. The first property is straightforward:

$$\mathbf{W}[as_1 + bs_2] = a\mathbf{W}s_1 + b\mathbf{W}s_2 \quad a, b \in \mathbb{R}.$$

Surjectivity is guaranteed by (1.7). In fact, being s equal to 0 only on certain intervals or points, it is transformed in the zero function only if the composition with w makes $s(w(x))$ return the only the zero values of $s(x)$. This is impossible, since $w(x)$, having positive derivative, maps x onto itself.

To verify the isometry property, we apply the adjoint operator in order to recover the identity:

$$[\mathbf{W}^\dagger\mathbf{W}](z, y) = \int_{\mathbb{R}} \delta(z - w(x))\delta(w(x) - y)dx$$

then we should set the following integration variable change:

$$w(x) = \xi \;\Rightarrow\; \dot{w}(x)dx = d\xi \;\Rightarrow\; dx = \frac{1}{\dot{w}(w^{-1}(\xi))}d\xi \qquad (1.8)$$

which gives:

$$\begin{aligned}[\mathbf{W}^\dagger\mathbf{W}](z,y) &= \int_{\mathbb{R}} \delta(z-\xi)\delta(\xi-y)\frac{1}{\dot{w}(w^{-1}(\xi))}d\xi \\ &= \frac{1}{\dot{w}(w^{-1}(z))}\delta(z-y).\end{aligned}$$

So, the isometry property is not verified, but this negative result suggest us how to modify the expression of $\mathbf{W}$. The integral should contain a factor equal to $\dot{w}(x)$, so that, by posing $w(x) = \xi$, $\dot{w}(x)dx$ would be simply substituted by $d\xi$. Therefore we set:

$$\mathbf{W} : L^2(\mathbb{R}) \to L^2(\mathbb{R}),\; s(y) \mapsto [\mathbf{W}s](x) = \sqrt{\dot{w}(x)}s(w(x))$$

whose kernel is:

$$\mathbf{W}(x,y) = \sqrt{\dot{w}(x)}\delta(w(x)-y).$$

Now the isometry property is easily verified:

$$\|\mathbf{W}s\|^2 = \int_{\mathbb{R}} \dot{w}(x)s^2(w(x))dx = \int_{\mathbb{R}} s^2(\xi)d\xi = \|s\|^2$$

where the above substitution (1.8) has been used.

Now we want to focus on the inverse operator $\mathbf{W}^{-1}$. As we verified, it can be expressed by the adjoint operator. Anyway, we did not take advantage of the functional inverse w^{-1}, which could serve as a mapping function as well. So we consider:

$$\tilde{\mathbf{W}}(z,x) = \sqrt{\dot{w^{-1}}(z)}\delta(w^{-1}(z)-y)$$

which, combined with $\mathbf{W}$, gives:

$$\begin{aligned}[\tilde{\mathbf{W}}\mathbf{W}](z,y) &= \int_{\mathbb{R}} \sqrt{\dot{w^{-1}}(z)\dot{w}(x)}\delta(w^{-1}(z)-x)\delta(w(x)-y)dx \\ &= \sqrt{\dot{w^{-1}}(z)\dot{w}(w^{-1}(z))}\delta(w(w^{-1}(z))-y) \\ &= \delta(z-y)\end{aligned}$$

where we exploited (1.8) for the expression of $\dot{w^{-1}}$. Finally we obtained the identity operator, which means that:

$$\tilde{\mathbf{W}} = \mathbf{W}^\dagger = \mathbf{W}^{-1}.$$

1.2.3 Continuous Frequency Warping Operator

Now we want to apply the continuous warping operator $\mathbf{W}$ in order to get a deformation of the frequency axis through an operator to be used in the time-domain. So, basically, the operator has to be applied between a Fourier transform and an inverse Fourier transform. This operator will be referred as $\mathbf{W_F}$, where the subscript points that the warping is executed in the transformed domain. We get:

$$\mathbf{W_F} = \mathbf{F}^\dagger \mathbf{W} \mathbf{F}.$$

Before going on computing its kernel, we introduce the intermediate operator $\mathbf{F_W}$:

$$\mathbf{F_W} = \mathbf{W}\mathbf{F}$$

whose kernel is given by:

$$\begin{aligned} \mathbf{F_W}(f,t) &= \int_{\mathbb{R}} \sqrt{\dot{w}(f)}\,\delta(w(f)-\xi)\,e^{-j2\pi\xi t}\,d\xi \\ &= \sqrt{\dot{w}(f)}\,e^{-j2\pi w(f)t}. \end{aligned}$$

$\mathbf{F_W}$ is still a unitary operator, being the composition of unitary operators. So, $\mathbf{W_F}$ is represented as:

$$\mathbf{W_F} = \mathbf{F}^\dagger \mathbf{F_W}.$$

having the following kernel:

$$\begin{aligned} \mathbf{W_F}(t,\tau) &= \int_{\mathbb{R}} \sqrt{\dot{w}(f)}\,e^{-j2\pi w(f)\tau}\,e^{j2\pi f t}\,df \\ &= \int_{\mathbb{R}} \sqrt{\dot{w}(f)}\,e^{j2\pi(ft-w(f)\tau)}\,df \end{aligned}$$

and the operator can be formally defined as:

$$\begin{aligned} &\mathbf{W_F} : L^2(\mathbb{R}) \to L^2(\mathbb{R}),\ s(\tau) \mapsto [\mathbf{W_F} s](t) = \\ &\qquad = \int_{\mathbb{R}} s(\tau) \int_{\mathbb{R}} \sqrt{\dot{w}(f)}\,e^{j2\pi(ft-w(f)\tau)}\,df\,d\tau. \end{aligned}$$

We point out that this operator, involving continuous operation, can not be analytically computed for a generic signal s, since, on the other hand, not even the continuous Fourier transform of a generic signal can be analytically performed.

We underline that $\mathbf{W_F}$ is still a unitary operator. Another thing to be taken into account is the shape to be given to the warping function w. Since we normally deal with real input signals, it may be required that the output is real as well. So, this requirement must be imposed on the shape of w. Intuitively, being the Fourier transformed of a real signal symmetric respect to the origin, we should impose that this symmetry is maintained after the application of frequency warping. In a simpler fashion, we can impose that the real part and the imaginary part of the operator $\mathbf{F_W}$ kernel are even and odd respectively:

$$\begin{aligned} \mathbf{F_W}(f,t) &= \mathbf{F_W}^*(-f,t) \\ \sqrt{\dot{w}(f)}e^{-j2\pi w(f)t} &= \sqrt{\dot{w}(-f)}e^{j2\pi w(-f)t} \end{aligned}$$

which is verified if:

$$w(f) = -w(-f). \tag{1.9}$$

that is, w must be an odd function in order to make $\mathbf{W_F}$ transform a real signal in a real signal. Since w is also an increasing function, it follows that the origin of the frequency axis is a fixed point of the w map, that is $w(0) = 0$.

1.2.4 Discrete-Time Frequency Warping

For discrete-time signals, the procedure to be used to obtain the corresponding frequency warping operator is the same as for the continuous time case. The warping operator has to be put between a Fourier transform and an inverse Fourier transform.

As far as the Fourier transform of a discrete-time signal is concerned, we can choose between definition (1.2) and (1.3). In order to maintain the entire frequency axis as codomain, we choose the first definition, so that:

$$\mathbf{W_{FD}} = \mathbf{DSF}^\dagger\mathbf{WFD}^\dagger = \mathbf{DSW_FD}^\dagger$$

is the target operator. The subscript $_{\mathbf{FD}}$ stays to represent that $\mathbf{W}$ is enclosed between a Fourier transform and a passage to a sampled domain.

Obviously, the warping map w has to be properly redefined in order to adapt to the periodicity of the Fourier transform of discrete-time signal. More precisely, we require the operator $\mathbf{DS}$ on the right not to cause loss of information, or rather, we

want $W_F D$ to give as output a sequence of Dirac impulses. To get this result, the warping map has to be defined as a function respecting conditions (1.7) and (1.9) and in addition, it must preserve periodicity. So, the effect of $\mathbf{WFD}^\dagger$ is:

$$[\mathbf{WFD}^\dagger s](f) = \sqrt{\dot{w}(f)} \sum_{n \in \mathbb{Z}_N} s(n) e^{-j2\pi n w(f)}$$

and we must impose:

$$[\mathbf{WFD}^\dagger s](f) = [\mathbf{WFD}^\dagger s](f + k) \quad k \in \mathbb{Z}$$

which can be rewritten as:

$$\sqrt{\dot{w}(f)} e^{-j2\pi n w(f)} = \sqrt{\dot{w}(f+k)} e^{-j2\pi n w(f+k)}.$$

We remind that a complex exponential is a periodic function whose period is equal to $j2\pi$, so we set:

$$w(f) = w(f + k) + n_k \quad k, n_k \in \mathbb{Z}$$

which also satisfies the equivalence of the square root factors. From the above equation, we derive:

$$w(k+1) - w(k) = n_{k+1} - n_k$$

with $n_0 = 0$ since $w(0) = 0$. Moreover, limited to the interval $[0, 1]$, w has to be an invertible map, so for sure we have $w(1) = 1$. Then it follows:

$$w(f + k) = k + w(f) \quad k \in \mathbb{Z}.$$

We also remind the property (1.9), which causes:

$$w(f) = -w(-f) = -w(-f + 1) + 1$$

where, by posing $f = 1/2$, we get:

$$w(1/2) = -w(-1/2 + 1) + 1 \quad \Rightarrow \quad w(1/2) = 1/2.$$

Finally, we conclude that in the discrete-time case, the warping map is designed such that it has an infinite number of fixed points in (k, k) with $k \in \mathbb{Z}$. In addition, if the resulting operator transforms real signals into real signals, than the map also has fixed points in $(k + 1/2, k + 1/2)$ with $k \in \mathbb{Z}$ and, if considered in

the interval $[k, k+1]$, it is antisymmetrical respect to the point $k+1/2$.

Now we can give the formal definition of $\mathbf{W}_{FD}$:

$$\mathbf{W_{FD}} : \ell^2(\mathbb{Z}) \to \ell^2(\mathbb{Z}),\ s(n) \mapsto [\mathbf{W_{FD}}s](m) = \\ = \sum_{n\in\mathbb{Z}} s(n) \int_0^1 \sqrt{\dot{w}(f)} e^{j2\pi(mf - nw(f))} df$$

where the kernel of $\mathbf{W_{FD}}$ can be actually considered as a matrix of infinite dimension:

$$\mathbf{W_{FD}}(m,n) = \int_0^1 \sqrt{\dot{w}(f)} e^{j2\pi(mf - nw(f))} df. \tag{1.10}$$

Again, we point out that the obtained operator is unitary, since it can be inverted by the adjoint operator. Although having discrete input and output, the operator $\mathbf{W_{FD}}$ can not be practically used. This is due to two facts:

- the computation of $\mathbf{W_{FD}}$ entries requires the calculation of an integral;
- input and output can not be infinite-dimensional.

The second issue can be solved by limiting the input and the output domain in a proper way, trying to preserve the unitary property. Instead, the first issue has to be solved by finding an algorithm to compute the matrix entries with discrete operations.

As a concluding remark, we show that the operator $\mathbf{W}_{FD}$ can be synthetically represented as a discrete-time warped Fourier transform $\mathbf{F_{WD}} = \mathbf{W}\mathbf{F_D}$ and an adjoint discrete-time Fourier transform (the inverse operator should be preferred to the adjoint one, since it is independent on the bivalence introduced for the definition of $\mathbf{F_D}$). So, it results:

$$\mathbf{W_{FD}} = \mathbf{F_D}^{\dagger}\mathbf{F_{WD}}.$$

The operator $\mathbf{F_{WD}}$, being the composition of the unitary operators $\mathbf{W}$ and $\mathbf{F}_D$, is still unitary:

$$\mathbf{F_{WD}}^{\dagger}\mathbf{F_{WD}} = \mathbf{I}.$$

1.2.5 Frequency Warping Transform

As a first step, the domain of the operator $\mathbf{W_{FD}}$ has to be limited. To do this, we exploit the operator $\mathbf{H}_N$, which has been previously introduced. The usage of this operator will be deliberately done with a subtle ambiguity. In some cases, $\mathbf{H}_N$ just turns to 0 the input samples which are indexed outside of a specified interval of consecutive integers, so it behaves like a singular transformation from $\ell^2(\mathbb{Z})$ to itself. In other cases, $\mathbf{H}_N$ has the role of limiting the domain to the interval of consecutive integers specified before, so it behaves like a transformation from $\ell^2(\mathbb{Z})$ to $\mathbb{R}^N$. So, the adopted behavior will be clear time to time by the context.

Now we introduce the following operator:

$$\mathbf{W_{FD}H}_N : \mathbb{R}^N \to \ell^2(\mathbb{Z}),\ s(n) \mapsto [\mathbf{W_{FD}H}_N s](m) = \\ = \sum_{n\in\mathbb{Z}_N} s(n) \int_0^1 \sqrt{\dot{w}(f)}\, e^{j2\pi(mf-nw(f))}\, df$$

where $\mathbb{Z}_N$ is a suitable set of N consecutive integers. This operator presents a significant difference in comparison to the operators introduced so far. In fact, previously, we always provided a definition for the operators such that the inverse transform is equal to the adjoint one. In this case, dealing with a *rectangular* matrix of dimension $\infty \times N$, the inverse matrix does not exist. Nevertheless, thanks to the unitary property of $\mathbf{W_{FD}}$, we have:

$$[\mathbf{W_{FD}H}_N]^\dagger[\mathbf{W_{FD}H}_N] = \mathbf{H}_N\mathbf{W}_{\mathbf{FD}}^\dagger\mathbf{W_{FD}H}_N = \mathbf{IH}_N = \mathbf{I}_N.$$

The above modification is painless, since it does not alter the property of perfectly recovering the input signal starting from the transformed one by the application of the adjoint operator. We point out that this relationship is not commutative, that is:

$$[\mathbf{W_{FD}H}_N][\mathbf{W_{FD}H}_N]^\dagger = \mathbf{W_{FD}H}_N\mathbf{W}_{\mathbf{FD}}^\dagger \neq \mathbf{I}$$

since, because of $\mathbf{H}_N$, the degrees of freedom are decreased from ∞ to N, that is $[\mathbf{W_{FD}H}_N]^\dagger$ is a singular not invertible operator.

So, for a finite computation, the input length must be limited. This is quite intuitive, since frequency warping is a time-variant transformation (time-variance is easily deduced by noting that in the frequency domain $\mathbf{W}_{FD}$ is equal to $\mathbf{W}$ and not to a diagonal operator).

We must introduce a further modification in order to cope with the infinite output length. As it has been done on the domain, we limit the codomain by applying an operator $\mathbf{H_M}$ on the left. The windowing matrix $\mathbf{H}_M$ is built like $\mathbf{H}_N$, but it may refer to a suitable set of consecutive integers whose length is equal to M. For the moment, there is no need to put any constraint on M. So, we set:

$$\mathbf{W}_{MN} = \mathbf{H}_M \mathbf{W}_{\mathbf{FD}} \mathbf{H}_N = \mathbf{H}_M \mathbf{D} \mathbf{S} \mathbf{F}^\dagger \mathbf{W} \mathbf{F} \mathbf{D}^\dagger \mathbf{H}_N$$

where the subscript $_{MN}$ means that $\mathbf{W}$ has been enclosed between a Fourier transform, a sampling and finally a truncation to a $M \times N$ matrix. Formally, the operator is represented by:

$$\begin{aligned} &\mathbf{W}_{MN} : \mathbb{R}^N \to \mathbb{R}^M,\ s(n) \mapsto [\mathbf{W}_{MN} s](m) = \\ &\quad = \sum_{n \in \mathbb{Z}_N} s(n) \int_0^1 \sqrt{\dot{w}(f)}\, e^{j2\pi(mf - nw(f))}\, df \quad m \in \mathbb{Z}_M. \end{aligned}$$

Unfortunately, independently on the chosen value of M, the operator $\mathbf{W}_{MN}$ loses the property of being inverted by its adjoint operator. In order to represent this loss, we define:

$$\mathbf{E}_{MN} = \mathbf{W}_{\mathbf{FD}} \mathbf{H}_N - \mathbf{W}_{MN}$$

which represents the complement matrix to $\mathbf{W}_{MN}$ respect to matrix $\mathbf{W}_{\mathbf{FD}} \mathbf{H}_N$. It has the meaning of error operator which occurs when matrix $\mathbf{W}_{\mathbf{FD}} \mathbf{H}_N$ is substituted by $\mathbf{W}_{MN}$. So, the composition of $\mathbf{W}_{MN}$ and its adjoint gives:

$$\mathbf{W}_{MN}^\dagger \mathbf{W}_{MN} = \mathbf{I}_N - \mathbf{E}_{MN}^\dagger \mathbf{E}_{MN}.$$

which, as said before, differs from the identity. Nevertheless, in the next chapters it will be shown how this operator can be used with a sufficient degree of precision. For the moment we do not deal with this problem and assume $\mathbf{W}_{MN}$ to be the target operator to be modeled.

1.2.6 Sampled Frequency Warping Transform

The entries of matrix $\mathbf{W}_{MN}$ are equal to the entries of matrix $\mathbf{W}_{\mathbf{FD}}$ limited to the *rectangle* given by the cartesian product $\mathbb{Z}_M \times \mathbb{Z}_N$. So, from a practical point of view, the new operator does not differ from the previous one in a significant manner. Instead,

from a conceptual point of view, the new operator allows some advantages. Being finite-dimensional, it may be possible to model the continuous integral by a discrete procedure.

Retracing the way Fourier operators were introduced, we first considered continuous operators, the we sampled the time axis and finally we sampled the frequency axis. So, now we introduce a sampling on the frequency axis of frequency warping operator as well. It is pretty obvious that this operation can not be painless. Since warping was originally defined on a continuous axis, sampling will probably alter the unitary property of warping. Nevertheless, as we said before about with regard to the application of operators $\mathbf{H}_M$, we will cope with reconstruction problem in the next chapters.

Let us consider the following:

$$\mathbf{DSF}^\dagger \mathbf{D}_M^\dagger \mathbf{D}_M \mathbf{WFD}^\dagger$$

which is operator $\mathbf{W_{FD}}$ on which a sampling in frequency has been applied. Intuitively, the sampling should produce a periodic repetition in time. To demonstrate this, we try to force the presence of operator $\mathbf{R}_M$. So, we evaluate the dual relationship of (1.1):

$$\mathbf{RHR} = \mathbf{R}$$

which means that a periodic space is invariant respect to the restriction to subspace $\mathbf{H}$ followed by periodic repetition. So $\mathbf{RH}$ behaves like an identity operator respect to a periodic input. It same can be rewritten in the following way:

$$\mathbf{RH} = \mathbf{FD}^\dagger \mathbf{DSF}^\dagger.$$

Since the operator $\mathbf{WFD}$ produces a periodic output, $\mathbf{RH}$ can be applied to it without any effects:

$$\begin{aligned}
\mathbf{DSF}^\dagger \mathbf{D}_M^\dagger \mathbf{D}_M \mathbf{WFD}^\dagger &= \mathbf{DSF}^\dagger \mathbf{D}_M^\dagger \mathbf{D}_M [\mathbf{RH}] \mathbf{WFD}^\dagger \\
&= \mathbf{DSF}^\dagger \mathbf{D}_M^\dagger \mathbf{D}_M [\mathbf{FD}^\dagger \mathbf{DSF}^\dagger] \mathbf{WFD}^\dagger \\
&= [\mathbf{DSF}^\dagger \mathbf{D}_M^\dagger \mathbf{D}_M \mathbf{FD}^\dagger][\mathbf{DSF}^\dagger \mathbf{WFD}^\dagger] \\
&= M \mathbf{R}_M \mathbf{W_{FD}}.
\end{aligned}$$

By applying of a limiter $\mathbf{H}_M$ and $\mathbf{H}_N$ on the left and on the right respectively, we can formally define the sampled frequency

warping transform:

$$\widetilde{\mathbf{W}}_{MN} : \mathbb{R}^N \to \mathbb{R}^M,\ s(n) \mapsto [\widetilde{\mathbf{W}}_{MN} s](m) =$$
$$\sum_{n\in\mathbb{Z}_N} s(n) M^{-1} \sum_{k=0}^{M-1} \sqrt{\dot{w}(k/M)}\, e^{j2\pi(mk/M - nw(k/M))} \qquad m \in \mathbb{Z}_M.$$

whose matrix has the following entries:

$$\widetilde{\mathbf{W}}_{MN}(m,n) = M^{-1} \sum_{k=0}^{M-1} \sqrt{\dot{w}(k/M)}\, e^{j2\pi(mk/M - nw(k/M))}.$$

As done for $\mathbf{W}_{FD}$, we introduce a synthetical representation by exploiting $\mathbf{F}^{\dagger}_{\mathbf{D}_M\mathbf{D}}$ and the discrete warped Fourier transform $\mathbf{F}_{\mathbf{D}_M\mathbf{W}\mathbf{D}} = \mathbf{D}_M\mathbf{W}\mathbf{F}\mathbf{D}^{\dagger}$:

$$\widetilde{\mathbf{W}}_{MN} = M^{-1}\mathbf{F}^{\dagger}_{\mathbf{D}_M\mathbf{D}}\mathbf{F}_{\mathbf{D}_M\mathbf{W}\mathbf{D}}.$$

Now we are interested in establishing a relationship between $\widetilde{\mathbf{W}}_{MN}$ and $\mathbf{W}_{MN}$. We consider:

$$\begin{aligned}\widetilde{\mathbf{W}}_{MN} &= \mathbf{H}_M\mathbf{R}_M\mathbf{W}_{\mathbf{FD}}\mathbf{H}_N \\ &= \mathbf{H}_M\mathbf{R}_M[\mathbf{W}_{MN} + \mathbf{E}_{MN}] \\ &= \mathbf{W}_{MN} + \mathbf{H}_M\mathbf{R}_M\mathbf{E}_{MN}\end{aligned}$$

which shows that the two operators differ for an aliasing contribution which will be referred as $\mathbf{A}$:

$$\mathbf{A}_{MN} = \mathbf{H}_M\mathbf{R}_M\mathbf{E}_{MN}. \tag{1.11}$$

Since the computation of $\widetilde{\mathbf{W}}_{MN}$ is done by discrete operations, if we have a mathematical model for $\mathbf{E}_{MN}$, than we can compute $\mathbf{A}_{MN}$,or rather $\mathbf{W}_{MN}$, by a discrete operations.

1.3 Conclusions

This chapter was dedicated to the introduction of basically mathematical concepts and models which will be developed in the rest of the work. More in details, we first reviewed the Fourier transform and its variants together with some well-known concepts like Nyquist theorem and time-frequency duality, then we introduced the warping operator.

Warping has been first presented as an intrinsic unitary transformation, then its application to the frequency axis has been considered. Finally, its truncated discrete-time variant has been detected and its relationship with approximated frequency sampled version has been identified.

Chapter

2 The Frequency Warping Matrix

Chapter 1 was dedicated to the introduction of the mathematical formalism and notation to describe the frequency warping operators. Starting from the Fourier transform, we followed a bottom–up approach, so that the global purpose of the introduction of new operators was probably lost. Anyway, giving a application–oriented description of frequency warping was not the main target of chapter 1.

Instead, here we want to deal with more practical issues related to frequency warping. First of all, we want to give an example about how to build a frequency warping map. Then we want to focus on the frequency warping kernel, in particular in the time–discrete case, so that we will actually deal with a matrix. For instance, important features of the warping matrix could be the existence of a sparsity pattern and the decay of its entries along rows or columns. Moreover we are interested in observing the relationships we set between the various frequency warping operators which were previously presented.

Finally, we will cope with the problem of choosing the dimensions of the warping matrix, or rather choosing the number of rows when the number of columns is given. As we previously considered, the truncation of the warping matrix to a finite dimensional matrix affects the property of being inverted by its adjoint one, which was the guideline for the derivation of all the operators. Therefore, truncation has to be performed carefully.

2.1 A Frequency Warping Map Example

We will deal here with discrete-time operators only. In order to make the reading easier, we recall the fundamental relationships which were obtained in chapter 1. In discrete-time spaces, the frequency warping operator was defined as a matrix of infinite dimensions whose entries are given by:

$$\mathbf{W_{FD}}(m,n) = \int_0^1 \sqrt{\dot{w}(f)}\, e^{j2\pi(mf-nw(f))}\, df \quad m,n \in \mathbb{Z}.$$

The frequency map has to be defined in the fundamental period $[0,1)$ and then extended to the rest of the frequency axis according to:

$$w(f+k) = k + w(f) \quad k \in \mathbb{Z}$$

which means that the frequency deviation $w(f)-f$ is a periodic function. Even if frequency warping is formally defined by a map, dealing with a differential representation, as the frequency deviation is, could be more intuitive.

An example of frequency warping map, represented on a single frequency period, is given by:

$$w(f) = \frac{1}{4}(2f^3 - 3f^2 + 5f) \quad f \in [0,1) \tag{2.1}$$

whose frequency deviation $\Delta(f) = w(f) - f$ has been depicted in Fig. 2.1. The warping map $w(f)$ is represented in the inset picture. As we said before, the frequency deviation can be perceived in a better way, while the warping map may result to be really close to the identity map $w(f) = f$. Although the deviation is really small, it affects the frequency warping matrix in a significant way, as it will be shown later, so the considered example can not be considered as a particular or pathological case.

Warping map (2.1) has not been designed according to application requirements, it just has a demonstrative purpose and will be used as a reference case in the rest of the work.

For the moment, we can do some observations. If considered only on $[0,1)$, the function (2.1) would be smooth. In chapter 1 we stressed on the fact that the frequency warping map ha to be considered on the entire frequency axis, and we forced the representation of the presented operators in order to always highlight the dependency by the deformation of the entire frequency axis. So, by extending (2.1) on the rest of the frequency

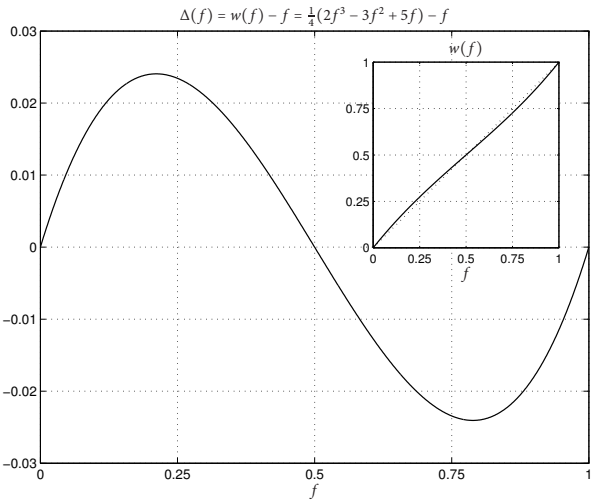

Figure 2.1: Frequency deviation $\Delta(f)$ of the warping map $w(f)$ (inset picture) in the fundamental period $[0,1)$. Considered on the entire axis, this map has an singularities on integer values of f.

axis by applying the proper periodic repetition, it turns out that its second derivative has an infinite number of discontinuities on $f = k$, $k \in \mathbb{Z}$, so it belongs to C^1. This property does not have any relevance for the present discussion, but it will turn out to be fundamental. If the periodicity of the frequency axis had been neglected in the modeling of the operators, this property could have passed unnoticed.

The map (2.1) has been described by a whole expression, but, when extended to the entire frequency axis, it has to be considered as a piecewise map. So, the design procedure is actually performed in a piecewise way. This suggests that we can obtain maps having similar properties, as far as smoothness is concerned, by employing any piecewise design procedure. For instance, the period can be split in intervals whose border points behaves as nodes, then on each interval the map is described as a polynomial. This procedure allows to easily approximate any target warping map. On the other hand, one could attempt to design smooth maps. Such a design would intuitively be more difficult, since global conditions have to be satisfied rather than local ones. Nevertheless, smooth maps have some other advantages which will be shown later.

2.2 Sparsity of a Warping Matrix

Now we try to heuristically understand the operation behind frequency warping. According to the way operator $\mathbf{W_{FD}}$ was decomposed, a time-limited discrete sequence is first transformed in the frequency domain, then its spectrum is reshaped according to a warping function w and multiplied to an orthogonalizing factor $\dot{w}^{1/2}$ and finally transformed back in the time-domain. The factor $\dot{w}^{1/2}$, representing an amplitude modulation, i.e. a convolution in the time-domain, necessarily causes a duration enlargement, so that the original time-limited input signal is potentially enlarged to the entire time-axis. This simple consideration explains the reason why it is not allowed to truncate the frequency warping matrix rows without compromising the unitary property.

Nevertheless, the amplitude modulation, acting in the same fashion on each column of $\mathbf{W_{FD}}$ independently on n, does not characterize the structure of the warping matrix in a significant way. Instead, the reshaping of frequency axis carries major effects. Since the spectrum is represented as a series of complex exponentials, the reshaping acts as a frequency modulation. Moreover, the modulating function is proportional to n, so this affects in a time-variant manner the warping matrix.

We remind that these considerations are intended to understand how to limit $\mathbf{W_{FD}}\mathbf{H}_N$ to its rows indexed in a set $\mathbb{Z}_M$ of M consecutive integers, according to the set $\mathbb{Z}_N$ by with the columns have been limited. For clarity, we set:

$$\mathbb{Z}_N = \{n_l, n_l + 1, \ldots, n_r\}$$

where n_l stays for *left* and n_r stays for *right*, and:

$$\mathbb{Z}_M = \{m_t, m_d + 1, \ldots, m_b\}$$

where m_t stays for *top* and m_b stays for *bottom*. The column axis, indexed by n, goes from left to right, while the row axis, indexed by m, goes from top to bottom. Given $\mathbb{Z}_N$, $\mathbb{Z}_M$ must be chosen so that only the significant entries of $\mathbf{W_{FD}}\mathbf{H}_N$ are discarded.

In order to evaluate an upper bound for m_t and a lower bound for m_b we have to consider the *line spectrum* of the kernel of $\mathbf{F_{WD}}$, i.e. the line spectrum of an amplitude and frequency modulated set of periodic functions. By substituting $w(f)$ in the complex exponential by its linear approximation in $f_0 \in [0, 1)$:

$$w(f) \simeq w(f_0) + \dot{w}(f_0) \cdot (f - f_0) = \dot{w}(f_0) f + \rho$$

where ρ_n is an arbitrary phase contribution, it results:

$$\mathbf{F_{WD}}(f_0, n) \simeq \sqrt{\dot{w}(f)}e^{-j2\pi n(\dot{w}(f_0)f+\rho)} \quad f \to f_0.$$

The effective carrier of the frequency modulation is represented by $n\dot{w}(f_0)$. By neglecting the effects of the phase contribution and of the amplitude modulation, which causes only a further $n-$constant duration enlargement, we get:

$$\begin{aligned}\mathbf{W_{FD}}(m, n, f_0) &\simeq \int_0^1 e^{j2\pi mf - n\dot{w}(f_0)f} df \\ &\simeq \int_0^1 e^{j2\pi(m-n\dot{w}(f_0))f} df \\ &\simeq \operatorname{sinc}(m - \lceil n\dot{w}(f_0)\rceil)\end{aligned}$$

where we deliberately made abuse of notation, since $\mathbf{W_{FD}}$ could not depend on f_0 and the sinc function stays for the Kronecker symbol. Anyway, the result tells us how to determine the bounds of the interval where energy should be concentrated. For minimizing and maximizing the position of the impulse $\lceil n\dot{w}(f_0)\rceil$, we must distinguish three different cases for n_l and n_r:

- $n_l < 0$ and $n_r < 0$:

$$m_t < -|n_l| \max \dot{w} \quad m_b > -|n_r| \min \dot{w}$$

- $n_l < 0$ and $n_r > 0$:

$$m_t < -|n_l| \max \dot{w} \quad m_b > |n_r| \max \dot{w}$$

- $n_l > 0$ and $n_r > 0$:

$$m_t < |n_l| \min \dot{w} \quad m_b > |n_r| \max \dot{w}.$$

More generally, we can state that significant entries of W_{FD} are enclosed between two lines whose slopes are $n \max \dot{w}$ and $n \min \dot{w}$. In Fig. 2.2, the *sparsity pattern* of the warping operator $\mathbf{W_{FD}}$ relative to the warping function (2.1) has been represented. Since $\max \dot{w}$ is equal to $5/4$, for $N = 128$, the minimum requirement for the output length is $M = 160$. The influence of the minimum of the derivative is also shown. This figure also represents a choice for $\mathbb{Z}_N$ which will be commonly adopted in

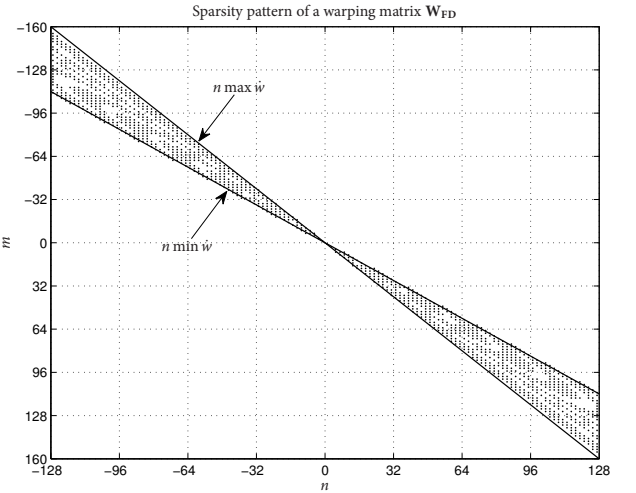

Figure 2.2: Entries of a warping matrix $\mathbf{W}_{\mathbf{FD}}$ having absolute value larger than 0.1 have been represented. The most significant entries are enclosed between two lines whose slopes are the maximum and the minimum of $\dot{w}$.

rest of the work. It consists in taking $\mathbb{Z}_N$ and consequently $\mathbb{Z}_M$ in a quasi-symmetrical fashion:

$$\mathbb{Z}_N = \{-N/2, \ldots, N/2-1\} \tag{2.2}$$
$$\mathbb{Z}_M = \{-M/2, \ldots, M/2-1\}. \tag{2.3}$$

According to the previous constraints, we must consider:

$$M > 2\left\lceil \frac{N}{2} \max \dot{w} \right\rceil \tag{2.4}$$

where M has been forced to be even.

According to the given constraints, the truncated warping operator $\mathbf{W}_{MN}$ should be close to be perfectly inverted by its adjoint:

$$\mathbf{W}_{MN}^{\dagger}\mathbf{W}_{MN} \simeq \mathbf{I}_N$$

since we assume that the error matrix does not give a significant contribution:

$$\mathbf{E}_{MN}^{\dagger}\mathbf{E}_{MN} \simeq \mathbf{O}_N.$$

where $\mathbf{O}_N$ represents the *null* matrix. A quantitative evaluation of the error will be treated in next chapters.

2.3 Time-Frequency Sampling

Now we want to describe frequency warping by its behavior in time and frequency. More in details, we want to analyze the way the time-frequency representation of a signal is changed by this transformation.

We remind that a time-frequency analysis is characterized by its basis vectors. The basis vectors of frequency warping, being represented by a matrix, are given by the matrix rows. So, we should study their time-frequency behavior in order to trace the curves representing their paths on the time-frequency plane.

We point now that for the sparsity characterization we focused on the matrix columns rather than on the matrix rows. To correctly perform this target change, we recall a generale property of the unitary operators and a particular property of the warping operator.

The first property, which is reported in (1.6) for a generic unitary operator, particularized for frequency warping becomes:

$$\mathbf{W_{FD}}s = \mathbf{F_D^\dagger W F_D}s = \mathbf{F_D^\dagger}[\mathbf{F_D^\dagger W}^\dagger]^\dagger s$$

which means that s, a apart from $\mathbf{F_D}^\dagger$ on the left, is analyzed by means of unwarped complex exponential. Equivalently we could have written:

$$\mathbf{W_{FD}}s = \mathbf{F_D^\dagger W F_D}s = [\mathbf{W}^\dagger \mathbf{F_D}]^\dagger[\mathbf{F_D}s].$$

which means that the spectrum of s is analyzed by means of unwarped complex exponential. In both representations, an unwarping takes place instead of a warping, since operator $\mathbf{W}$ is adjoint.

The second property consists in the possibility of representing the adjoint warping operator, or rather the inverse one, by exploiting the inverse map w^{-1}:

$$\mathbf{W}^{-1}(z,x) = \sqrt{\dot{w^{-1}}(z)}\delta(w^{-1}(z) - y).$$

Finally, it is clear that we must model the columns of $\mathbf{W_{FD}}$ as we did for its rows provided that w is substituted by w^{-1}:

$$\begin{aligned}
\mathbf{W_{FD}}^\dagger(n,m,f) &\simeq \int_0^1 e^{j2\pi n\xi - m\dot{w^{-1}}(f)\xi} d\xi \\
&\simeq \int_0^1 e^{j2\pi(n - m\dot{w^{-1}}(f))f} d\xi \\
&\simeq \mathrm{sinc}(n - m\dot{w^{-1}}(f))
\end{aligned}$$

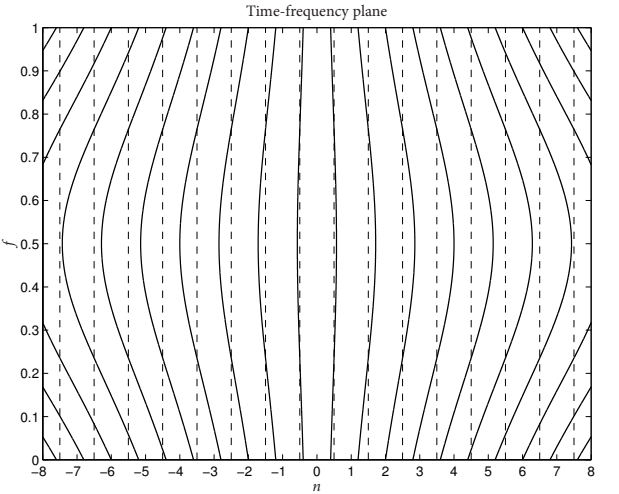

Figure 2.3: Sampling of the time-frequency plane referred to a discrete time signal due to frequency warping. The shaping of each tile is related to the derivative of the inverse of the warping map.

So, the curves representing the basis vectors are generated by the points (n, f) nullifying the argument of the sinc:

$$n = m\dot{w^{-1}}(f).$$

Of course n is considered as a continuous time variable. Rather than representing a basis vector by a curve, it is preferable to represent the correspondence area occupied by the basis vector on the time-frequency plane. By supposing that the curve is centered respect to the covered area, the $m-$tile is delimited by:

$$[(m - \tfrac{1}{2})\dot{w^{-1}}, (m + \tfrac{1}{2})\dot{w^{-1}}].$$

The sampling of the time-frequency plane induced by (2.1) is represented in Fig. 2.3. By standard sampling, the plane would be covered by rectangular tiles having area equal to 1 (dashed lines). The area of the reshaped tiles is still equal to 1, in fact:

$$\int_0^1 \dot{w^{-1}}(f)df = w^{-1}(f)\Big|_0^1 = w^{-1}(1) - w^{-1}(0) = 0$$

since w^{-1}, being a warping map, has the same property as w.

2.4 Smooth vs. non-Smooth Maps

Till now we just gave the schematic representation of a frequency warping matrix. The analysis which brought to Fig. 2.3 was done in a qualitative manner, so we just got a rough binary description in terms significant or not significant entry value. Here we want to focus on the matrix coefficients decay.

Besides, we are interested in comparing the frequency warping matrix $\mathbf{W_{FD}}$, or rather its truncation $\mathbf{W}_{MN}$, to its approximated version $\widetilde{\mathbf{W}}_{MN}$, which has been shown to be affected by time aliasing because of the sampling process performed in the frequency domain. This aliasing effect has been modeled by an aliasing operator $\mathbf{A}_{MN}$:

$$\widetilde{\mathbf{W}}_{MN} = \mathbf{W}_{MN} + \mathbf{A}_{MN}.$$

In Fig. 2.4 we represented the warping matrix $\mathbf{W}_{MN}$ and the aliasing matrix $\mathbf{A}_{MN}$ referred to the warping map (2.1) for $N = 2^8$ and $M = 2N$. Since $\max \dot{w}$ was shown to be $5/4$, M, according to previously obtained constraints, is properly selected and guarantees that most of the frequency warping matrix energy has been enclosed in $\mathbf{W}_{MN}$.

By observing the decay of $\mathbf{W}_{MN}$ coefficients over m, we infer that the non truncated matrix $\mathbf{W_{FD}}$ may have a slow decay. The relationship between the warping map properties and the decay will be investigated later. Nevertheless, we notice that the discarded coefficients of $\mathbf{E}_{MN}$ produce a very regular aliasing matrix. As a consequence, the aliasing operator $\mathbf{A}_{MN}$ should have a small rank, which means that it may be described by few basis vectors, or, equivalently, $\mathbf{A}_{MN}$ may be computed in a fast manner.

The reason why we are interested in efficiently computing $\mathbf{A}_{MN}$ in order to compensate the difference between $\mathbf{W}_{MN}$ and $\widetilde{\mathbf{W}}_{MN}$is that aliasing causes a decrease in accuracy when the inverse warping is performed by the adjoint operator:

$$\|s - \widetilde{\mathbf{W}}_{MN}^{\dagger}\widetilde{\mathbf{W}}_{MN}s\| \geq \|s - \mathbf{W}_{MN}^{\dagger}\mathbf{W}_{MN}s\|$$

that is:

$$\|\widetilde{\mathbf{W}}_{MN}^{\dagger}\widetilde{\mathbf{W}}_{MN} - \mathbf{I}_N\| \geq \|\mathbf{W}_{MN}^{\dagger}\mathbf{W}_{MN} - \mathbf{I}_N\|.$$

where $\|\cdot\|$ represents the euclidian and the spectral norm for a vector and a matrix respectively.

This relationship can be heuristically demonstrated as follows. For the left side we have:

$$\begin{aligned}\|\mathbf{W}_{MN}^{\dagger}\mathbf{W}_{MN} + \mathbf{W}_{MN}^{\dagger}\mathbf{A}_{MN} + \mathbf{A}_{MN}^{\dagger}\mathbf{W}_{MN} + \mathbf{A}_{MN}^{\dagger}\mathbf{A}_{MN} - \mathbf{I}_N\| \\ = \|\mathbf{E}_{MN}^{\dagger}\mathbf{E}_{MN} + \mathbf{W}_{MN}^{\dagger}\mathbf{A}_{MN} + \mathbf{A}_{MN}^{\dagger}\mathbf{W}_{MN} + \mathbf{A}_{MN}^{\dagger}\mathbf{A}_{MN}\|\end{aligned}$$

while for the right side we have:

$$\|\mathbf{E}_{MN}^{\dagger}\mathbf{E}_{MN}\|.$$

We should find a lower bound for the left side, so the norm of the sum of the operators can not be substituted by the sum of the norms. Nevertheless we suppose that this substitution is allowed and we focus on $\mathbf{W}_{MN}^{\dagger}\mathbf{A}_{MN}$ and discard the other operators. The inequality becomes:

$$\|\mathbf{W}_{MN}^{\dagger}\mathbf{H}_M\mathbf{R}_M\mathbf{E}_{MN}\| = \|[\mathbf{W}_{MN}^{\dagger}\mathbf{R}_M]\mathbf{E}_{MN}\| \geq \|\mathbf{E}_{MN}^{\dagger}\mathbf{E}_{MN}\|$$

The relationship intuitively beholds since the left side consists in the product of the periodic repetition of $\mathbf{W}_{MN}$ and the decaying operator $\mathbf{E}_{MN}$, while the right side is the product between two decaying operators. Despite of the heuristic demonstration, this result will be proven with experimental measurements in next chapters.

If the warping function w is *smooth*, matrix $\mathbf{E}_{MN}$ decays exponentially, so the aliasing effect is negligible and the reconstruction error is negligible as well. Furthermore, it follows that the error decreases quickly as M increases, so that a proper setting of M can make the reconstruction error comparable to machine error.

For non-smooth warping functions, the error is not negligible, so aliasing cancelation has to be considered in order to compensate the decrease in reconstruction accuracy. As we said before, non-smooth warping maps allow a piecewise design which can better match shaping specifications. In the following chapters we will illustrate how to fast compute both $\widetilde{\mathbf{W}}_{MN}$ and $\mathbf{A}_{MN}$ in case of non-smooth maps, so that the target operator $\mathbf{W}_{MN}$ is fast computed as well.

2.5 Conclusions

In this chapter we illustrated the features of the frequency warping matrix. We mainly focused on the role of the warping

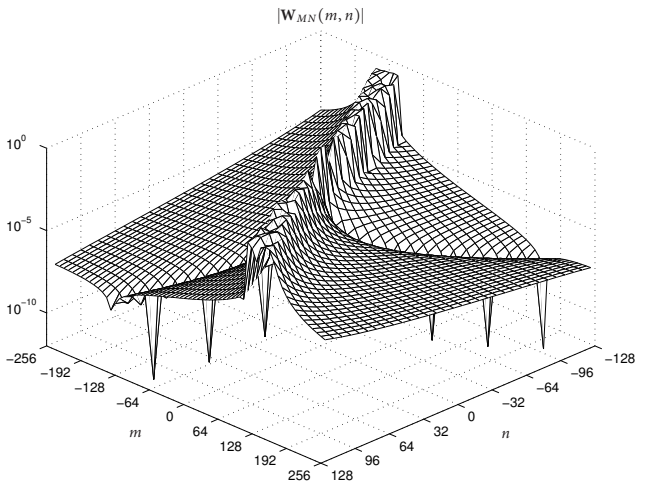

(a)

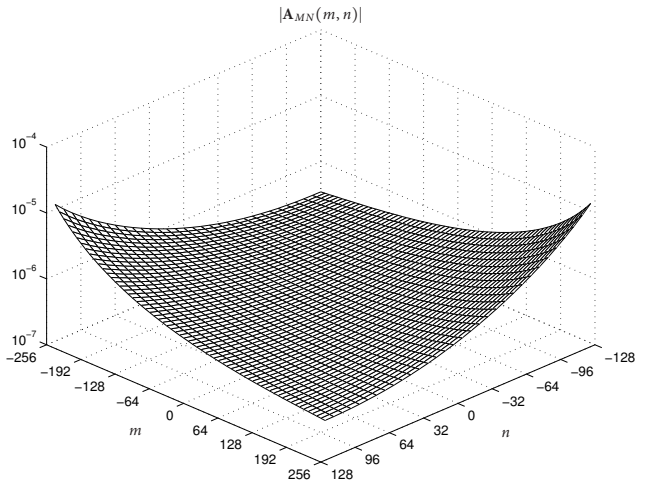

(b)

Figure 2.4: Absolute values of the warping matrix $\mathbf{W}_{MN}$ entries (a), where the sparsity pattern shown in Fig. 2.2 can be observed, and absolute values of the aliasing matrix $\mathbf{A}_{MN}$ entries (b).

map in determining the time-duration characteristics and the way the time-frequency plane is sampled. In this framework, we were able to detect the constraints for correctly truncating the warping matrix and to illustrate the connection between required time-frequency specifications and warping map design. Moreover, we showed how the map smoothness can affect the importance of aliasing in the computation of the frequency warping operator.

Part

II

Algorithms for Frequency Warping

Chapter

3 Nonuniform Fast Fourier Transform

The first part of this work was dedicated to present and settle the warping transforms we are dealing with. Starting from the continuous case, we redefined Fourier and warping operators in case of discrete-time axis. The discrete-time frequency warping was identified as the target operator to be modeled for the achievement of a feasible implementation. At this aim, two major problems were detected, consisting in the computation of a continuous integral and non-finite dimensions of the resulting operator. This last issue was solved by properly truncating the warping matrix, while the first one was overcome by decomposing the operator in two additive terms, one representing the frequency sampled discrete frequency warping operator and the other one representing time aliasing occurring because of the sampling in frequency. Moreover, the frequency sampled operator was described as the composition of a nonuniform and scaled discrete Fourier transform and an inverse ordinary discrete Fourier transform. Fast algorithms for the discrete Fourier transform are widely known, while algorithms for the nonuniform one deserve a deep insight.

Here we first recall some algorithms which have been presented in literature, then we introduce an original contribution [21] which will be shown to be optimum in case of dense sampling of the frequency axis (output length larger then input length), as it occurs for frequency warping.

3.1 Introduction to NUFFT

The Discrete Fourier Transform (DFT) is known to be a fundamental transformation in most fields of signal processing. It is very efficiently computed since algorithms which yields $O(N \log N)$ rather than $O(N^2)$ operations have been found. However, many applications are based on the computation of Fourier coefficients of nonuniformly sampled frequencies. This occurs when frequency warping techniques are introduced [18] or when directional analysis techniques are applied on two dimensional signals, like the polar Fourier Transform, the Radon Transform and the Contourlet Transform [22]. In such cases the transformation is referred as Nonuniform Fourier Transform and its fast implementation as Nonuniform Fast Fourier Transform (NUFFT).

In previous works [12, 14, 15] NUFFT is implemented by means of interpolation, i.e. each nonuniform Fourier coefficient is obtained by *interpolating* the Discrete Fourier coefficients in the neighborhood of the considered nonuniform frequency. In order to improve the performances, an oversampled DFT is employed, where the oversampling factor is generally taken equal to 2. Moreover, the input signal is previously scaled by a suitable scaling vector. In [14], the interpolator is obtained by a least square approximation with respect to the oversampled DFT basis. A significant improvement is obtained in [12], where first a bell-shaped interpolator is chosen and then the scaling vector is obtained by imposing a minimization on the approximation error. Finally in [15], scaling is considered as if it were applied to the oversampled DFT basis, although it is actually applied on the input signal. Then a least square interpolator is computed. The optimization of the scaling vector is an untractable problem and so it is chosen according to [12], resulting in a slight performance improvement.

Here we introduce a different approach. Each nonuniform Fourier exponential in the interval between two contiguous uniform Fourier frequencies is approximated by a small set of orthogonal vectors, obtained by a singular value decomposition (SVD). Only a single set of orthogonal vectors is needed. In facts, every nonuniform Fourier exponential can be obtained by modulating a nonuniform Fourier exponential of a single interval. So, first the input signal is scaled according to a small set of vectors. Second, the scaled versions of the input signal are

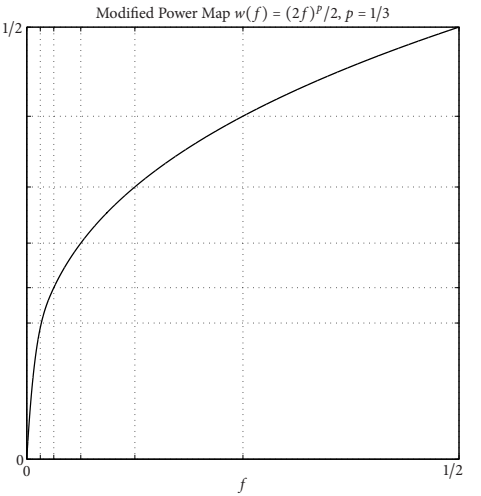

Figure 3.1: Warping map for frequency warping purposes: a constant-Q splitting by octaves (horizontal axis) is converted to a constant-Q splitting with higher frequency resolution (vertical axis). Frequency warping introduces a redundant representation of a signal, where the redundancy factor is given by the maximum slope of the warping map. The map has been modified around the origin in order to have a finite maximum slope, nevertheless the resulting density is very high.

Fourier transformed. Finally, the Fourier coefficients referred to the same frequency are linearly combined. This operation will be referred as *interpolation* in analogy with the interpolation techniques, although this term is inappropriate.

By doing so, interpolation coefficients result to be real, allowing a saving of an half of the total amount of multiplications. The resulting computational complexity is $O(N \log N)$. It will be shown that this approach is optimum when the number of output samples is higher enough than the number of input samples, i.e. when the nonuniform frequency set is sufficiently *dense*. In NUFFT applications this situation is common. For example in frequency warping the density is given by the maximum slope of the frequency map. Some useful frequency maps, as the one depicted in fig. 3.1, introduce a very high density.

As an exception, the notation employed in this chapter is completely uncorrelated from the rest of the work. Variables and operators will be defined when needed. Nevertheless, the description of the proposed algorithm will take advantage of the

previously introduced operator notation.

3.2 Problem Statement

Given a discrete signal x_n, $n = 0, \ldots, N-1$, we wish to compute the following transformation:

$$X(k) = \sum_{n=0}^{N-1} x_n e^{-j2\pi(n-\tau) f_k / N} \quad f_k \in [0, N). \tag{3.1}$$

for $k = 0 \ldots, K-1$, where K is the cardinality of the set of nonuniform frequencies f_k. τ is a shift parameter which changes the indexing of the Fourier exponentials. As particular cases f_k could include uniform frequencies $0, \ldots, N-1$. The number of output samples K to number of input samples N ratio will be referred as the *density* of the NUFFT:

$$\rho = \frac{K}{N} \tag{3.2}$$

which will be employed in order to make considerations on computational complexity. The density ρ can also be intended as the number of different NUFFTs which must be computed for the same input signal. The spectra of nonuniform Fourier exponentials of a particular nonuniform frequency map are depicted in fig. 3.2.

Without loss of generality, in this work we will consider the parameter shift τ equal to $N/2$:

$$X(k) = \sum_{n=0}^{N-1} x_n e^{-j2\pi(n-N/2) f_k / N} \quad f_k \in [0, N) \tag{3.3}$$

since solutions to problem (3.1) are obtained through element by element product between X_k and $e^{j2\pi(\tau - N/2) f_k}$. The assumption (3.3) is equivalent to consider the input signal indexed in $-N/2, \ldots, N/2-1$. In fact, signals originated by windowing operation and images have $-N/2, \ldots, N/2-1$ as natural indexing. Moreover, it will be show that this choice allows a computational cost reduction, since in (3.3) the exponentials are nearly symmetric respect to $n = N/2$.

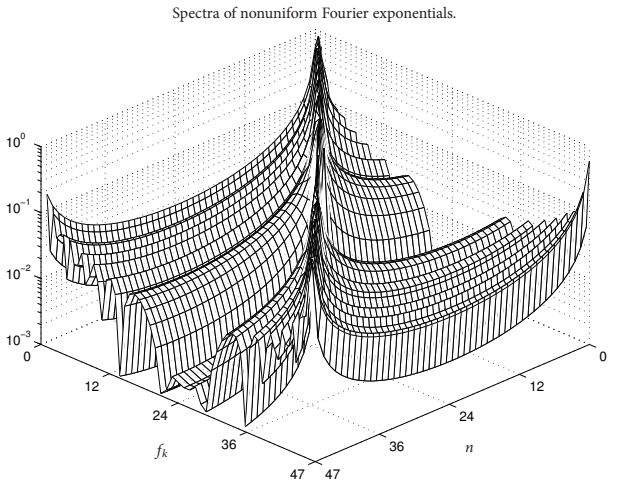

Figure 3.2: Spectra of nonuniform Fourier exponentials. Nonuniform frequencies f_k, $k = 0, \ldots, K-1$, are obtained by uniformly sampling a nonlinear function such that $f_0 = 0$ and $f_K = 1$. Spectra decay slowly since periodic repetition of a nonuniform Fourier exponential have discontinuities.

3.3 Interpolation Approach

The interpolation approach is based on the on the calculation of an oversampled FFT Y of the input signal scaled by a suitable vector c_n:

$$Y_i = \sum_{n=0}^{N-1} c_n x_n e^{-j2\pi ni/M} \qquad i = 0, \ldots, M-1 \tag{3.4}$$

where $M = mN$ and $m \in \mathbb{N}$ is the oversampling factor. Generally m is taken equal to 2, since taking $m > 2$ does not increase performances significantly. Then, the frequency axis is considered as a collection of M intervals $[i-1/M, i)$, $i = 0, \ldots, M-1$, and nonuniform Fourier exponentials of the i-th interval are approximated by linearly combining L FFT coefficients in the neighborhood of Y_i:

$$X(f_k) = \sum_{l=-L/2}^{L/2-1} Y_{i+l}\,\phi(f_k/m - (i+l)) \qquad f_k \in [i-1/m, i). \tag{3.5}$$

This formulation is valid for even values of L, but can be easily extended to odd values.

Clearly, (3.5) is an interpolation formula. So, the interpolating function ϕ must be chosen in some way. A possible approach [12] consists in choosing an appropriate interpolating continuous function and then finding c_n so that the approximation error is minimized. By doing so, ϕ is obtained from a finite-support bell-like function ψ by periodic repetition and phase modulation:

$$\phi(f) = \sum_{i=-\infty}^{\infty} e^{-j\pi(f-iM)(N-1)/M}\psi(f - iM) \tag{3.6}$$

and it follows:

$$c_n^{-1} = \int_{-L/2}^{L/2} \psi(f) e^{j2\pi f(n-(N-1)/2)/M} df \tag{3.7}$$

Eventually, the scaling vector can be chosen in order to make the error result null on the oversampled Fourier frequencies $0, \ldots, M-1$. It follows:

$$c_n^{-1} = \sum_{l=-L/2}^{L/2} \psi(l) e^{j2\pi l(n-(N-1)/2)/M}. \tag{3.8}$$

Finally ψ must be chosen according to time-frequency considerations. It has been shown that the Kaiser-Bessel window is a good choice for the function ψ.

From an algebraic point of view, the interpolator could be obtained as follows [15]. The scaling vector in (3.4) is associated with the complex exponentials rather than with the input signal. So, the set of the amplitude modulated Fourier exponentials $c_n e^{-j2\pi n(i+l)/mN}$, $l = -L/2, \ldots, L/2 - 1$, acts as a basis for the approximation space of nonuniform Fourier exponentials in $[i - 1/m, i)$. Then the interpolator is obtained by a least square approach with respect to this space. The scaling vector should be chosen in order to minimize the approximation error. Unfortunately, an optimization over the scaling coefficients c_n is an untractable problem, so c_n are obtained by (3.7) or (3.8) according to a specified window ϕ. For Kaiser-Bessel window, this algebraic approach leads to slightly different coefficients and slightly better performances. In fig. 3.3 some scaled exponentials corresponding to an optimized Kaiser-Bessel interpolator are represented.

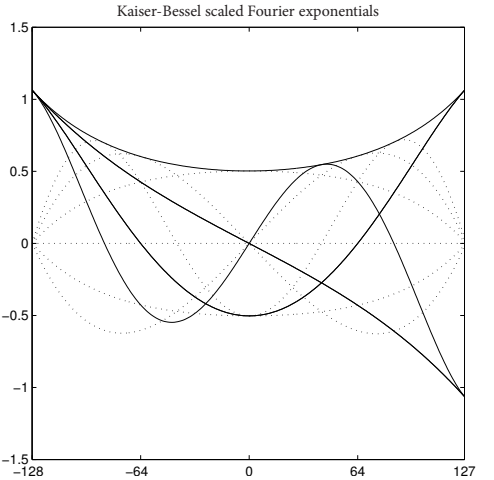

Figure 3.3: Kaiser-Bessel scaled Fourier exponentials for $N = 2^8$, real part (solid line) and imaginary part (dotted line). In interpolation approaches, they act as basis vectors for the approximation space of nonuniform Fourier exponentials with $f_k \in [0, 1/2)$.

3.4 SVD-based Proposed Algorithm

According to the algebraic approach described in the previous section, further improvements can be achieved only by focusing on the choice of basis vectors. In fact, thanks to scaling vector and to oversampled FFT, basis vectors of fig. 3.3 become less regular by gaining discontinuities on the interval edges and have slowly decaying spectra. As a consequence, the space generated by this basis achieves a better approximation of nonuniform Fourier exponentials, which precisely have slowly decaying spectra, as depicted in fig. 3.2. So, in order to obtain an optimum approximation, we want to find an optimum basis.

In the present section we will use a matrix notation. Taken a generic operator $\mathbf{A}$, the adjoint and the transpose operators will be represented by $\mathbf{A}^\dagger$ and $\mathbf{A}'$ respectively. The meaning of subscripts and superscripts will be specified at any time they are used. A vector of generic size N will be indexed in $0, \ldots N-1$. Indexes which are not included in $0, \ldots, N-1$ are to be intended as mod_N. The symbols $\delta_0, \delta_1\, \delta_2, \ldots$, will denote shifted impulsive column vectors of suitable size.

First, we define the following unitary operators:

$$\mathbf{T} = \begin{bmatrix} \delta_1 & \delta_2 & \cdots & \delta_{N-1} & \delta_0 \end{bmatrix} \tag{3.9}$$

$$\mathbf{R} = \begin{bmatrix} \delta_{N-1} & \delta_{N-2} & \cdots & \delta_1 & \delta_0 \end{bmatrix} \tag{3.10}$$

which represent circular shift and time-reversing respectively. Now we consider the $[N \times K]$ matrix $\mathbf{E}$ whose columns are nonuniform Fourier exponentials. The elements $\mathbf{E}(n,k)$ of this matrix are given by:

$$\mathbf{E}(n,k) = e^{j2\pi(n-N/2)f_k/N}. \tag{3.11}$$

Thanks to the considered time indexing, the real part of the columns of $\mathbf{E}$ is symmetric and the imaginary part is antisymmetric with respect to $n = N/2$, apart for $n = 0$:

$$\mathbf{E} = \mathbf{Z}\mathbf{E}^* + j2\delta_0\delta_0'\,\Im[\mathbf{E}]$$

where $\delta_0\delta_0'$ is a two-dimensional impulsive $[N \times N]$ matrix and $\mathbf{Z}$ is defined as follows:

$$\mathbf{Z} = \mathbf{T}\,\mathbf{R} = \begin{bmatrix} \delta_0 & \delta_{N-1} & \cdots & \delta_2 & \delta_1 \end{bmatrix}. \tag{3.12}$$

The operator $\mathbf{Z}$ acts as a complex conjugation only if it is applied to the Fourier transform of a real vector, so $\mathbf{F}^\dagger\mathbf{E}$ is real if $\Im[\mathbf{E}(0,\cdot)] = 0$, where $\mathbf{F}$ represents the Fourier transform. In order to deal with a real matrix rather than with a complex one, we introduce the following operator:

$$\tilde{\mathbf{E}} = \mathbf{E} - j\delta_0\delta_0'\,\Im[\mathbf{E}]. \tag{3.13}$$

By defining the row vector $\mathbf{D} = j\Im[\mathbf{E}(0,\cdot)]$ of size K, the column vector X of size K representing the NUFFT (3.3) of the input signal x results:

$$X = \mathbf{E}^\dagger x = \tilde{\mathbf{E}}^\dagger x + \mathbf{D}^\dagger x_0. \tag{3.14}$$

Now, the nonuniform frequency set is partitioned in $2N$ subsets corresponding to contiguous frequency intervals:

$$f_k^{(l)} \in [l/2, l/2 + 1/2) \quad l = 0, \ldots, 2N-1 \tag{3.15}$$

whose cardinalities are K_l. Then, the set of nonuniform Fourier exponentials corresponding to each interval is considered:

$$\mathbf{E}_l(n,k) = e^{j2\pi(n-N/2)f_k^{(l)}/N} \tag{3.16}$$

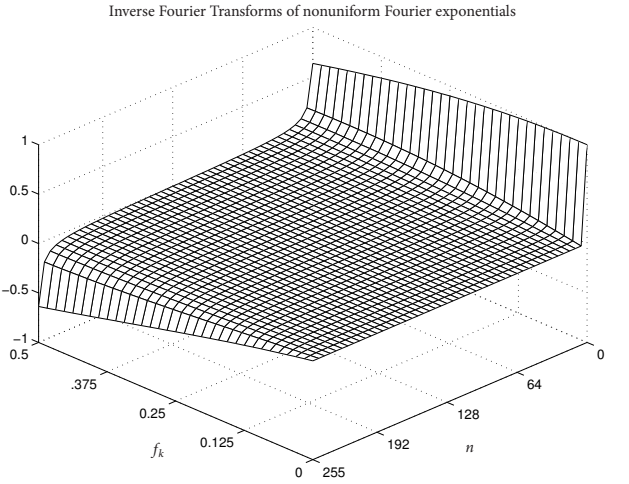

Figure 3.4: Entries of the matrix $\mathbf{F}^{\dagger}\tilde{\mathbf{E}}_0$. When nonuniform frequency f_k tends to 0, the matrix column tends to be an impulse. The columns are very correlated, so the rank of the matrix is small.

It is worth to note that $\mathbf{E}_l$, for even l, could be obtained by modulating the column vectors of a nonuniform Fourier matrix referred to a suitable set of frequencies $f_k \in [0, 1/2)$, which will be represented as $\mathbf{E}_{l,0}$. For odd l, $\mathbf{E}_l$ could be obtained in the same way from a nonuniform Fourier matrix whose frequencies refer to $f_k \in [-1/2, 0)$, which could be also obtained by conjugating a suitable matrix $\mathbf{E}_{l,0}$. Modulation can be converted in circular shift by passing in the Fourier domain, so, by some some calculations, it follows:

$$\tilde{\mathbf{E}}_l = (-1)^i \mathbf{F}\mathbf{T}^{-i}\mathbf{F}^{\dagger}\tilde{\mathbf{E}}_{l,0} \qquad l = 2i \tag{3.17}$$

$$\tilde{\mathbf{E}}_l = (-1)^i \mathbf{F}\mathbf{T}^{-i}\mathbf{F}^{\dagger}\tilde{\mathbf{E}}^{*}_{l,0}\mathbf{R} \quad l = 2i - 1. \tag{3.18}$$

where the formulation (3.14) has been exploited in order to deal with the real matrixes $\mathbf{F}^{\dagger}\tilde{\mathbf{E}}_{l,0}$. In general, each matrix $\tilde{\mathbf{E}}_{l,0}$ refers to randomly distributed frequencies in $[0, 1/2)$. In order to find a single basis for the column vectors of all matrixes $\tilde{\mathbf{E}}_{l,0}$, we can equally consider a generic matrix $\mathbf{E}_0$ which ideally has as column vectors every possible nonuniform Fourier exponentials in $[0, 1/2)$. In practice, it suffices to consider a finite set of nonuniform frequencies which densely cover the whole $[0, 1/2)$ interval. This matrix has very correlated column vectors, as

depicted in fig. 3.4, so its rank results to be small for a certain precision. As a consequence, a singular value decomposition can be introduced, i.e. $\mathbf{F}^\dagger \tilde{\mathbf{E}}_0 = \mathbf{U}\mathbf{S}\mathbf{V}'$. The singular values decay exponentially, so we could consider a reduced number L of singular values and neglect the others:

$$\mathbf{F}^\dagger \tilde{\mathbf{E}}_0 \simeq \mathbf{U}_L \mathbf{S}_L \mathbf{V}'_L \tag{3.19}$$

where $\mathbf{U}_L$ and $\mathbf{V}_L$ are constituted by the first L columns of $\mathbf{U}$ and $\mathbf{V}$ respectively and $\mathbf{S}_L$ is a square matrix constituted by the first L rows and columns of $\mathbf{S}$. The column vectors of $\mathbf{U}_L$ represent an optimum basis for all the matrixes $\tilde{\mathbf{E}}_{0,l}$. Then, the decomposition is extended to $\tilde{\mathbf{E}}_l$ in the following way:

$$\tilde{\mathbf{E}}_l \simeq \mathbf{F}\mathbf{T}^{-i}\mathbf{U}_L\mathbf{P}'_l \qquad l = 2i \tag{3.20}$$

$$\tilde{\mathbf{E}}_l \simeq \mathbf{F}\mathbf{T}^{-i}\mathbf{Z}\mathbf{U}_L\mathbf{P}'_l \qquad l = 2i-1 \tag{3.21}$$

where each $\mathbf{P}_l$ is a real $[K_l \times L]$ matrix which linearly combine the column vectors of $\mathbf{U}_L$ in order to obtain the best approximation of $\tilde{\mathbf{E}}_{l,0}$. Since $\mathbf{U}_L$ has orthogonal columns, $\mathbf{P}_l$ are simply obtained by computing:

$$\mathbf{P}_l = (\mathbf{T}^i\mathbf{F}^\dagger\tilde{\mathbf{E}}_l)'\mathbf{U}_L \qquad l = 2i \tag{3.22}$$

$$\mathbf{P}_l = (\mathbf{Z}\mathbf{T}^i\mathbf{F}^\dagger\tilde{\mathbf{E}}_l)'\mathbf{U}_L \qquad l = 2i-1. \tag{3.23}$$

The column vectors of each $\tilde{\mathbf{E}}_l$ are approximated by linearly combining the columns of $\mathbf{F}\mathbf{T}^{-i}\mathbf{U}_L$ or $\mathbf{F}\mathbf{T}^{-i}\mathbf{Z}\mathbf{U}_L$ through the rows of the matrix $\mathbf{P}_l$. In order to compute (3.14), we must calculate the scalar products between x and the columns of $\mathbf{F}\mathbf{T}^{-i}\mathbf{U}_L$ and $\mathbf{F}\mathbf{T}^{-i}\mathbf{Z}\mathbf{U}_L$ in an efficient way. With some algebra, it has been found that first, x must be scaled by the Fourier antitrasformed vectors of $\mathbf{U}_L$, $\mathbf{W} = \mathbf{F}^\dagger\mathbf{U}_L$:

$$\mathbf{X} = \mathrm{diag}(x)\mathbf{W} \tag{3.24}$$

where $\mathrm{diag}(x)$ is a matrix having x as main diagonal. The columns of $\mathbf{W}$ corresponding to the first 6 singular values are depicted in fig. 3.5. Then, the Fourier transforms of the column vectors of $\mathbf{X}$ produce the needed $N \times L$ scalar products:

$$\mathbf{Q} = \mathbf{F}\mathbf{X} \tag{3.25}$$

Each row of $\mathbf{Q}$ will be pointed by $\mathbf{Q}_i$. Finally we obtain that $\tilde{X}^{(l)} = \tilde{\mathbf{E}}_l^\dagger x$ is given by the product between a $[K_l \times L]$ matrix

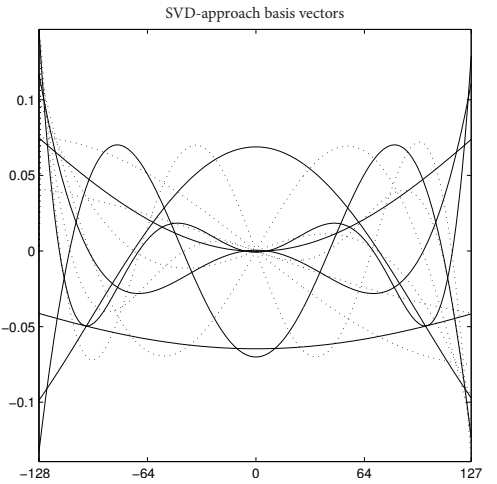

Figure 3.5: Fourier Transforms of the first 6 orthogonal vectors $\mathbf{U}_L$, real part (solid line) and imaginary part (dotted line). These vectors have the same role which vectors depicted in fig. 3.3 play in the conventional approach.

and a column vector of size L:

$$\tilde{X}^{(l)} \simeq \mathbf{P}_l \mathbf{Q}_i^{\dagger} \qquad l = 2i \tag{3.26}$$

$$\tilde{X}^{(l)} \simeq \mathbf{P}_l \mathbf{Q}'_{-i} \qquad l = 2i - 1 \tag{3.27}$$

Summarizing, the algorithm consists in precomputing *interpolation* coefficients (3.22)-(3.23), computing L scaling (3.24), calculating $N \times L$ scalar products (3.25) and *interpolating* them (3.26)-(3.27). It is worth to note that the term *interpolation* is only used in analogy with the conventional technique.

3.5 Performances

The computational cost of both interpolation and SVD-based approaches is given by three terms, cost of scaling, cost of Fourier transforms and cost of interpolation. In terms of real multiplication, for the presented algorithm it results:

$$\kappa_{\text{svd}} = 2LN + 4LN \log_2 N + 2LN\rho \tag{3.28}$$

where ρ represents the NUFFT density (3.2). The first additive term derives from (3.24), where L element-by-element products

between a real and a complex vector of size N are computed, i.e. $2LN$ real multiplications. The second term derives from (3.25), where L Fourier transforms of vectors of size N are computed. Each Fourier transform needs $4N \log_2 N$ real multiplications. Finally, the third term derives from (3.26)-(3.27) where $K = \rho N$ scalar products between a real and a complex vector of size L are computed, or, equally, L complex scaling of a real vector of size ρN. The cost of $\mathbf{D}^\dagger x_0$ (3.14) can be neglected. Through analogous considerations, for interpolation techniques it results:

$$\kappa_{\text{int}} = N + 8N \log_2 N + 4LN\rho\lambda. \tag{3.29}$$

The factor $\lambda > 1$ is an effective parameter which takes into account that, for the same value of L, SVD-based approach has better performances, as depicted in fig. 3.6. For useful values of L, λ is nearly equal to $1,4$. As far as memory requirements are concerned, in terms of real numbers for the SVD-approach it results:

$$\mu_{\text{svd}} = LN + LN\rho + N\rho \tag{3.30}$$

where terms correspond to the complex vectors $\mathbf{W}$ to the real interpolation coefficients $\mathbf{P}_l$ and to the vector $\mathbf{D}$ respectively. Only LN real coefficients are necessary for the vectors $\mathbf{W}$, since they are the Fourier transforms of the real vectors $\mathbf{U}_L$. Similarly, for interpolation approach it results:

$$\mu_{\text{int}} = N + 2LN\rho\lambda. \tag{3.31}$$

A fair comparison between the two approaches is quite hard. Sufficient conditions for SVD-approach to be less expensive than interpolation approach are:

$$\rho > \log_2 N \quad \Rightarrow \quad \kappa_{\text{svd}} < \kappa_{\text{int}} \tag{3.32}$$

$$\rho > 1 \quad \Rightarrow \quad \mu_{\text{svd}} < \mu_{\text{int}} \tag{3.33}$$

In worst cases, when $\rho \approx 1$, the proposed method would consist in more multiplications because of the computation of L Fourier transforms. Nevertheless, the algorithm has a serial structure, since each basis vector requires the computation of a scaling, a fast Fourier transform and its contribution to the interpolation, which is actually another scaling. Moreover, it does not involve complex multiplications in the scaling and interpolation computation. Furthermore, since the algorithm is based on orthogonal

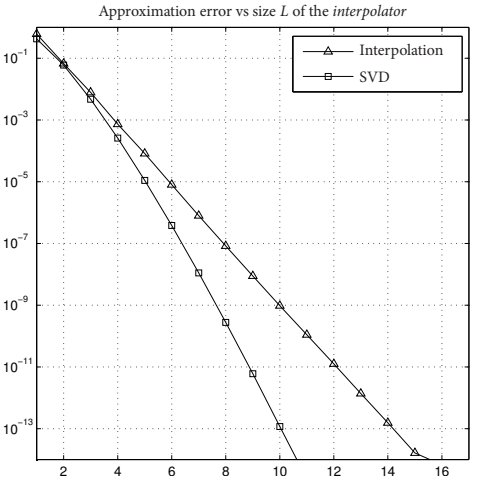

Figure 3.6: Comparison between the approximation errors given by the proposed SVD-based and the interpolation algorithm versus the size of the *interpolator*. The maximum of the euclidian norm of the error have been measured.

projections, the size of the interpolator L can be increased by simply adding basis vectors. Finally, the fast Fourier transform, being a very common operation, is generally optimized and efficiently managed. For these reasons, the comparison have been focused only on the approximation error respect to the size L of the interpolator employed to approximate each nonuniform Fourier exponential, represented in fig. 3.6. In fig. 3.7 we have compared the approximation errors for a generic matrix $\mathbf{E}_0$, i.e. a matrix with nonuniform frequencies in $[0, 1/2)$ for interpolator size L equal to 8. The error given by SVD-based approach is 3 orders of magnitude lower than error given by interpolation approach, in coherence with values represented in fig. 3.6.

3.6 Conclusions

In this chapter we presented a novel approach for the computation of the Nonuniform Fourier Transform based on Singular Value Decomposition. The proposed algorithm has quasi-linear complexity. In comparison with the conventional interpolation approach, our proposed approach has been shown to have a

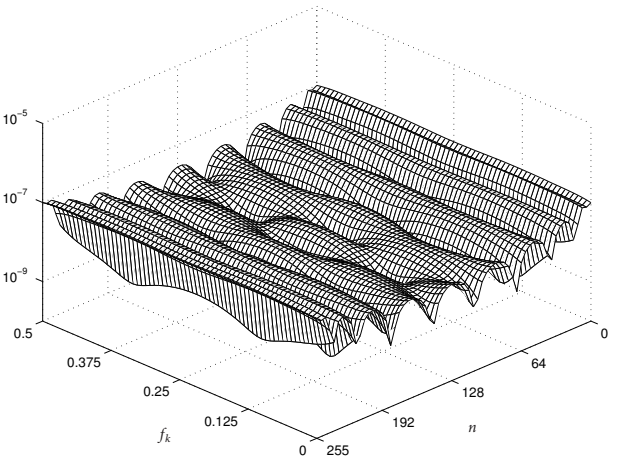

(a) Approximation error of $\tilde{\mathbf{E}}_0$ by interpolation approach, $L = 8$

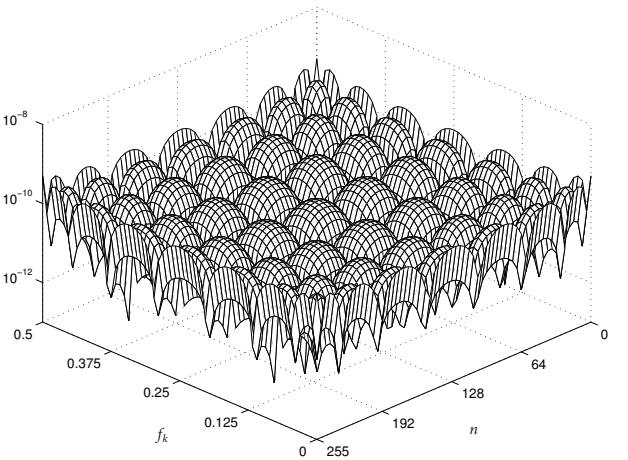

(b) Approximation error of $\tilde{\mathbf{E}}_0$ by SVD-based approach, $L = 8$

Figure 3.7: Comparison between the approximation errors of the matrix $\tilde{\mathbf{E}}_0$ given by the interpolation approach (a) and the proposed SVD-based approach (b), for size L of the *interpolator* equal to 8.

higher computational cost for the calculation of the projection components, but a lower cost for interpolating them. Moreover, this algorithm provides advantages in terms of computational structure, being based on Fast Fourier Transforms and real multiplications.

Chapter

4 Factorization of the Aliasing Matrix

The present chapter is the core of the entire work. In fact, the issues which are going to be treated occupy a major relevance in terms of importance originality and innovation of the obtained results. Basically, the content of this chapter completes the analytical characterization of the frequency warping matrix in order to make a fast computation achievable. Although it configures as a completion, it involves a lot of mathematical modeling effort and carries many implications on the nature of the operator under consideration which goes beyond simple computational issues. From the following analysis, as well as a factorization for the aliasing matrix which is necessary to correctly describe the frequency warping operator by compensating the effects of having sampled the frequency axis, useful hints for the warping map design strategy are also obtained. Moreover, the present model acts a starting point for further investigations, like the quantitative characterization of reconstruction accuracy, which is treated in the next chapter.

The results which are illustrated here are a detailed explanation of some previously obtained preliminaries results [19, 20]. The notation is consistent with the one described in chapter 1, although some letters will be reassigned to other operators for fulfill representation necessities.

4.1 Problem Statement and Methodology

The purpose of this chapter is to model the operator $\mathbf{A}_{MN}$ involved, together with $\widetilde{\mathbf{W}}_{MN}$, in the computation of operator $\mathbf{W}_{MN}$, as they were introduced in chapter 1. The investigation is limited to the case of non-smooth maps only, since it has been previously shown that the usefulness of aliasing compensation is not significant in case of smooth maps. The interest in non-smooth maps is based on the ease in designing suitable warping maps.

The aim of this investigation is to achieve the ability of compute the aliasing operator by means of the warping map features only, without explicitly calculate the difference between $\widetilde{\mathbf{W}}_{MN}$ and $\mathbf{W}_{MN}$. Moreover, it would be desirable to obtain a fast algorithm for computing the output of $\mathbf{A}_{MN}$ with a linear complexity.

The methodology can be briefly described as follows. We exploit the fact that aliasing is equivalently obtained as the periodic repetition along columns of operator $\mathbf{E}_{MN}$. When M is properly set, $\mathbf{E}_{MN}$ has a regular behavior since it mainly depends on the singularities of the warping map only. In fact, singularities consisting in steps in the frequency domain, i.e. fast variations, can be equivalently described in the time domain by considering large time indexes, like in matrix $\mathbf{E}_{MN}$, which will be also referred as tails matrix, since it contains the discarded tails of $\mathbf{W}_{FD}$. So, after having determined a model for $\mathbf{E}_{MN}$, a model for $\mathbf{A}_{MN}$ can be easily obtained as well.

As far as the fast computation is concerned, since the model for $\mathbf{A}_{MN}$ turns out to be a factorization like a singular value decomposition with a fast decaying internal kernel, a linear complexity is easily obtained by properly truncating the kernel. Moreover, the kernel is the only factor sensibly depending on the characteristics of the warping map, so the obtained algorithm is very efficient and allows a simple computational architecture.

Before going through the mathematical modeling, which is full of complex demonstrations, we propose a heuristic approach to the problem. This constitutes an attempt to trace out the path which inspired the further deep mathematical insight, in order to present it just as formalization of some simple intuitions.

To get some further simplifications in notation, here we neglect the subscript $_{MN}$ on operators $\mathbf{W}_{MN}$, $\mathbf{E}_{MN}$ and $\mathbf{A}_{MN}$. This would generate an ambiguity between $\mathbf{W}$, representing

the native axis warping, and $\mathbf{W}_{MN}$, representing the frequency warping. Antway the first one is not needed here. Letters **S**, **D** and **U**, introduced in chapter 1, are reassigned to new operators.

4.2 Heuristic Model of the Tails Matrix

Before describing the mathematical modeling of the aliasing matrix, let us make some heuristic considerations about the warping matrix decay.

As a case study, we still consider the non–smooth warping map w in (2.1). As we observed before, $w \in \mathcal{C}^1$, $\max \dot{w} = 5/4$ and there is only one singularity placed in $f = 0$ within the fundamental interval $[0, 1)$. In Fig. 4.1 we plotted some columns of the warping matrix in a wide temporal range in both semilog (Fig. 4.1(a)) and loglog axis (Fig. 4.1(b)). Independently on n, each column converges to the same asymptote. In loglog axis, for $w \in \mathcal{C}^1$, the asymptote is given by a line whose slope is -2 (see Section 4.3.1).

Now we suppose to be able to determine the intercept of the asymptote in Fig. 4.1(b). We can imagine to subtract the asymptote and define a residual matrix $\mathbf{G}_2$. Some of its columns have been depicted in Fig. 4.2(a). The decay is shown to be proportional to lines having slope equal to -3 but having different intercepts. Again, we can subtract the asymptotes and obtain a new matrix which will be referred as $\mathbf{G}_3$ and shown in Fig. 4.2(b) for some columns. In general, we define:

$$\mathbf{G}_l(m,n) = \mathbf{W}_{\mathbf{FD}}(m,n) - \sum_{i=1}^{l} \zeta_{i,n} \frac{m^{-i}}{(M/2)^{-i}}$$

where the generic subscript l means that asymptotes from m^{-1} till m^{-l} have been subtracted and the normalization to $M/2$ has been introduced in order to obtain well-scaled values for coefficients $\zeta_{i,n}$. This process could be iterated for $l \to \infty$. However, as it will be demonstrated in Section 4.4.2, after some iterations, matrix $\mathbf{G}_l$ converges to 0 in $(\mathbb{Z} \setminus \mathbb{Z}_M) \times \mathbb{Z}_N$, where $\mathbb{Z}_N$ and $\mathbb{Z}_M$ are settled according to the quasi-symmetrical choice (2.2)-(2.3). This means that the columns of $\mathbf{E}(m,n)$ can be represented as a linear combination of m^{-i} when the coefficients $\zeta_{i,n}$ are known. Then, when periodic repetition can be analytically computed, aliasing can be represented as a linear combination of analytically known vectors.

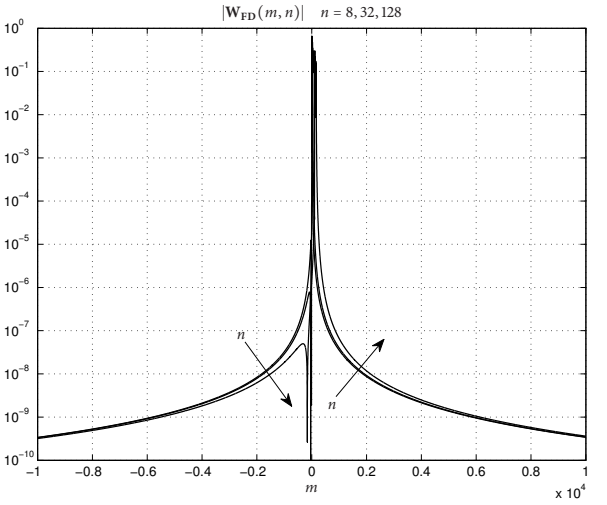

(a)

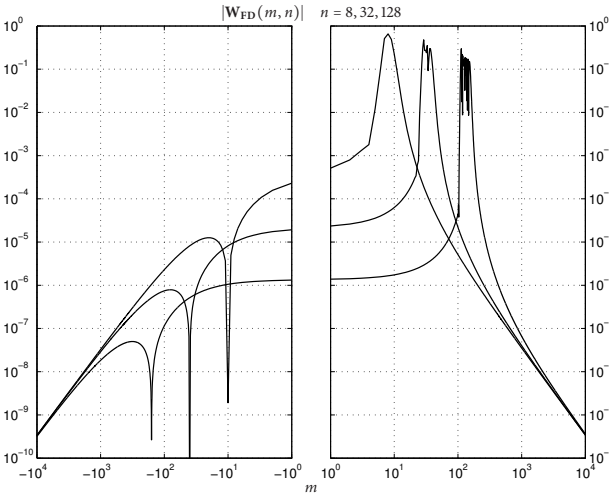

(b)

Figure 4.1: Absolute value of warping matrix columns for $n = 8, 32, 128$. The decay for $m \to \infty$ is proportional to m^{-2} and the asymptote is the same for every n.

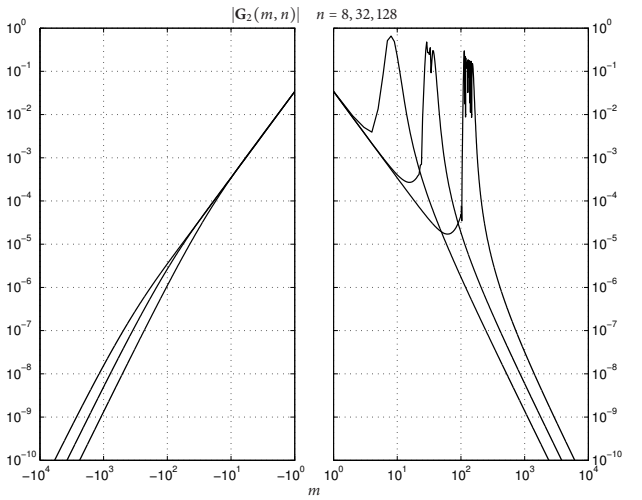

(a)

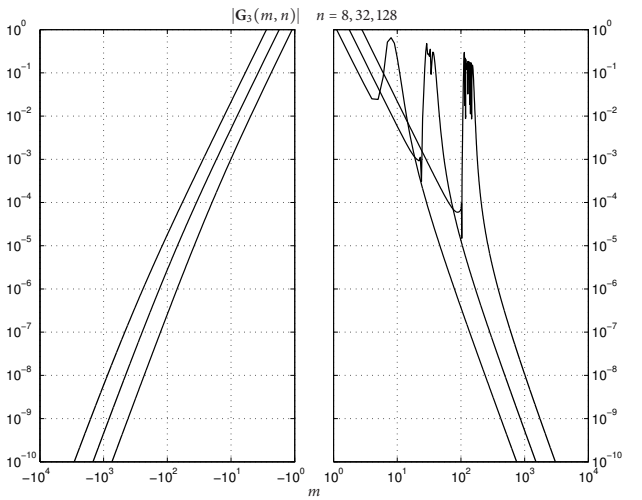

(b)

Figure 4.2: Absolute value of the sequences resulting by iteratively subtracting the asymptote from matrix $\mathbf{W_{FD}}$. Asymptotes $\propto m^{-2}$ and $\propto m^{-3}$ are eliminated in (a) and (b) respectively.

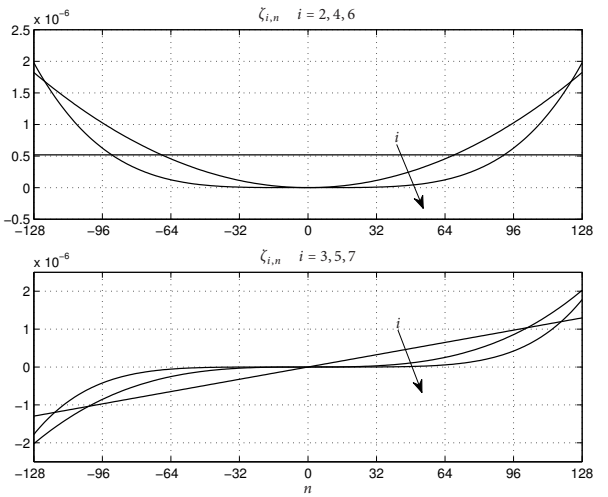

(a)

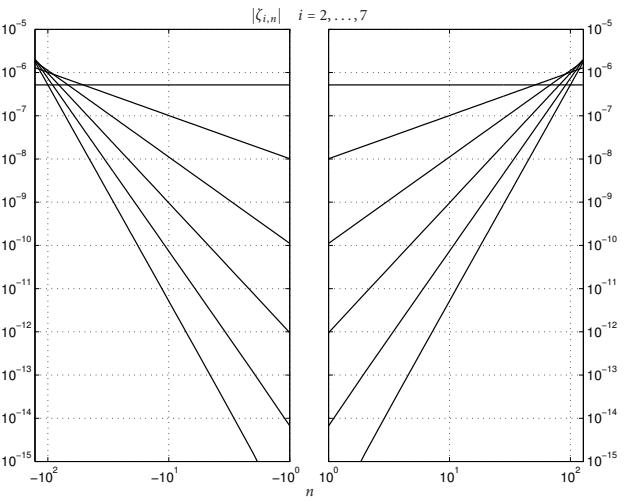

(b)

Figure 4.3: Entries $\mathbf{E}(m, n)$ are obtained as a series of negative powers m^{-i} whose coefficients $\zeta_{i,n}$, represented in linear (a) and semilog axis (b), are roughly given by positive powers of n.

In order to complete the description of the warping matrix tails for $m \to \infty$, its behavior respect to n has to be characterized. In Fig. 4.3 we depicted the coefficients $\zeta_{i,n}$ for $N = 2^8$ and $M = 2N$ in linear axis and loglog axis. The coefficients are clearly proportional to n^i. In the next Section we will show how they are represented as a series of n^k, $k = 0, \ldots, i$.

So, the basic idea which will be developed in the following sections is to make the dependency of $\mathbf{E}_{MN}(m, n)$ on negative powers of m and positive powers of n arise, in order to verify that the observations which have been done on the considered example are systematic and therefore characterize the aliasing matrix in an intrinsic manner. Moreover, the identification of the coefficients of these series is a major issue and will require most of the efforts.

4.3 Modeling of the Aliasing Matrix

In chapter 2, it was pointed out that the maximum of the warping map derivative is the parameter mainly affecting the duration in time of the warping matrix columns, i.e. influencing the truncation of the warping matrix. Nevertheless, it is not an exhaustive parameter to characterize the aliasing matrix. In fact, it was previously shown that the differentiability order of the warping map affects the behavior of the warping matrix for $m \to \infty$, hence it affects the aliasing matrix as well.

Let us suppose that $w \in \mathcal{C}^\sigma$ with a single singularity in $\xi \in [0,1)$. An infinite number of singularities are obviously located in $\xi + k$, $k \in \mathbb{Z}$. In this Section, we neglect the fact that an additional singularity should be placed in $1 - \xi$ to maintain the odd symmetry of the warping map respect to $1/2$. Multiple singularities will be treated in Section 4.4.3. We assume that $\mathbb{Z}_N$ and $\mathbb{Z}_M$ are chosen according to (2.2) and (2.3) respectively and M is settled by (2.4).

According to equation (1.11), in order to evaluate $\mathbf{A}$ we first have to evaluate $\mathbf{E}$ which is actually equal to $\mathbf{W_{FD}}$ for $m \notin \mathbb{Z}_M$ and $n \notin \mathbb{Z}_N$. We refer to equation (1.10), which represents the inverse Fourier transform of the set of periodic functions $\mathbf{F_{WD}}(f, n)$ whose differentiability class can be easily demonstrated to be $\mathcal{C}^{\sigma-1}$ because of the factor $\sqrt{\dot{w}(f)}$:

$$w \in \mathcal{C}^\sigma \quad \Rightarrow \quad \mathbf{F_{WD}} \in \mathcal{C}^{\sigma-1}. \tag{4.1}$$

If M respects the constraint (2.4), $\mathbf{E}$ depends only on fast variations of $\mathbf{F_{WD}}$. Being a set of piecewise-smooth functions, fast variations are entirely concentrated in the singularity point located in ξ.

In the following paragraphs, we will first investigate the dependency of $\mathbf{E}(m,n)$ on m, then we will focus on the dependency on n, and finally we will show how to compute $\mathbf{A}$ by periodically repeating $\mathbf{E}$ along columns.

4.3.1 Dependency of Tails on the Row Index

Without loss of generality, we consider $[\xi - 1/2, \xi + 1/2)$ as the fundamental interval and, for convenience, we set:

$$\phi_n(f) = \mathbf{F_{WD}}(f,n).$$

By doing so, the function ϕ_n is smooth in both $[\xi - 1/2, \xi)$ and $(\xi, \xi + 1/2)$. In these two intervals, we express ϕ_n by its Taylor series centered in ξ^- and ξ^+ respectively, so it holds:

$$\phi_n(f) = \begin{cases} \sum_{i=0}^{\infty} \frac{(f-\xi)^i}{i!} D^i\phi_n(\xi^-) & f \in [\xi - 1/2, \xi) \\ \sum_{i=0}^{\infty} \frac{(f-\xi)^i}{i!} D^i\phi_n(\xi^+) & f \in (\xi, \xi + 1/2) \end{cases}.$$

According to (4.1), for $i = 0, \ldots, \sigma - 1$ $\phi_n(\xi^-) = \phi_n(\xi^+) = \phi_n(\xi)$. For $i \geq \sigma$, in order to unify the representation, we can take advantage of the step Heaviside function H:

$$\phi_n(f) = \sum_{i=0}^{\sigma-1} \frac{(f-\xi)^i}{i!} D^i\phi_n(\xi) + \sum_{i=\sigma}^{\infty} \frac{(f-\xi)^i}{i!} D^i\phi_n(\xi^-) + H(f-\xi) \sum_{i=\sigma}^{\infty} \frac{(f-\xi)^i}{i!} \left[D^i\phi_n(\xi^+) - D^i\phi_n(\xi^-) \right] \quad (4.2)$$

where $D^i\phi_n$ is the Euler's notation for the higher order derivatives of ϕ_n. Since we are interested in evaluating $\mathbf{E}(m,n)$, the behavior of the inverse Fourier transform $[\mathbf{F_D}^\dagger \phi_n](m)$ for large values of m has to be modeled only. For computational purposes, we introduce a more suitable function $\varphi_n(f)$ such that its inverse Fourier transform is asymptotically the same as for ϕ_n:

$$[\mathbf{F_D}^\dagger \varphi_n](m) = [\mathbf{F_D}^\dagger \phi_n](m) \quad m \notin \mathbb{Z}_M.$$

Table 4.1: Analytic expression of functions $\psi_i(f)$ for $i = 0, \dots, 3$ in the fundamental period $[0,1)$.

$\psi_0(f)$	$H(f) - f - \frac{1}{2}$
$\psi_1(f)$	$H(f)f - \frac{1}{2}f^2 - \frac{1}{2}f - \frac{1}{2}$
$\psi_2(f)$	$H(f)\frac{1}{2}f^2 - \frac{1}{6}f^3 - \frac{1}{4}f^2 - \frac{1}{12}f$
$\psi_3(f)$	$H(f)\frac{1}{6}f^3 - \frac{1}{24}f^4 - \frac{1}{12}f^3 - \frac{1}{24}f^2 + \frac{1}{720}$

Each function ϕ_n contributes to fast variations only through the step function, so the first two summations in (4.2) can be neglected and only the behavior of the last term is reproduced in $\varphi_n(f)$. Let us define:

$$\varphi_n(f) = \sum_{i=\sigma}^{\infty} \chi_{i,n}(\xi)\psi_i(f-\xi)$$

where $\chi_{i,n}(\xi)$ represents the step in $D^i\phi_n$:

$$\chi_{i,n}(\xi) = D^i\phi_n(\xi^+) - D^i\phi_n(\xi^-) \tag{4.3}$$

and $\psi_i(f)$ are defined for $f \in [0,1)$ so that their periodization results to belong to $\mathcal{C}^{i-1}$:

$$\psi_i(f) = H(f)\frac{f^i}{i!} - \sum_{k=0}^{i+1} \rho_{i+1,k} f^k \quad f \in [0,1). \tag{4.4}$$

The first term in (4.4) represents a function whose i-th derivative is the Heaviside function $H(f)$, so that the whole set $\{\psi_i\}_{i\in\mathbb{N}}$ can represent functions having discontinuities on each derivatives. In the second term, coefficients $\rho_{i,k}$ are calculated by imposing $\psi_i(0) = \psi_i(1)$ to make the functions periodic and zero-mean, and it can easily proved that they are recursively related by:

$$D^i\psi_i = \psi_{i-1}$$

and, by doing so, one gets:

$$D^{i+1}\psi_i(f) = \delta(f) - 1. \tag{4.5}$$

Table 4.1 reports the expressions of the functions plotted in Fig. 4.4, where we depicted the periodization of functions ψ_i for $i = 0, \dots, 3$ in the interval $[-1,1]$. As i increases, the presence

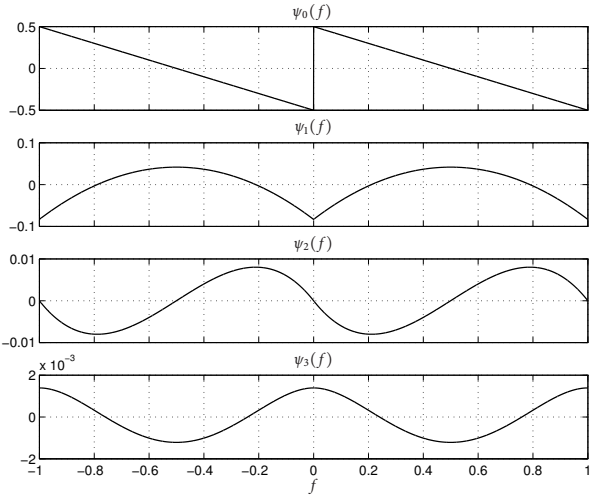

Figure 4.4: Periodization of functions ψ_i, $i = 0, \ldots, 3$ used for representing the singularities contained in functions ϕ_n. The interval $[-1, 1]$ is considered as domain in order to highlight the behavior around the singularity in $f = 0$.

of the singularity becomes less evident and the function tends to resemble a sine or a cosine. . A detailed explanation about how to find the coefficients $\rho_{i,k}$ is given in Appendix 4.A.1.

The function φ_n has been built so that $D^p\varphi_n$ has the same steps as $D^p\phi_n$. In fact, for $D^p\varphi_n$ we get:

$$D^p\varphi_n(f) = \sum_{i=\sigma}^{\infty} \chi_{i,n}(\xi)\psi_{i-p}(f-\xi)$$

then, by evaluating $D^p\varphi_n(\xi^+) - D^p\varphi_n(\xi^-)$, we get:

$$D^p\varphi_n(\xi^+) - D^p\varphi_n(\xi^-) = \sum_{i=\sigma}^{\infty} \chi_{i,n}(\xi)[\psi_{i-p}(0^+) - \psi_{i-p}(1^-)]$$

where $\psi_{i-p}(0^+) - \psi_{i-p}(1^-) = \delta(i-p)$ (see (4.5)), so:

$$D^i\varphi_n(\xi^+) - D^i\varphi_n(\xi^-) = \chi_{i,n}(\xi).$$

The behavior of $\mathbf{E}(m, n)$ can be inferred by studying $\mathbf{F_D}^\dagger\varphi_n$,

hence, thanks to linearity, by studying $\mathbf{F_D}^\dagger \psi_n$:

$$\begin{aligned}
[\mathbf{F_D}^\dagger \psi_i(\cdot - \xi)](m) &= e^{j2\pi m\xi}[\mathbf{F_D}^\dagger \psi_i](m) \\
&= e^{j2\pi m\xi}(-j2\pi m)^{-(i+1)}[\mathbf{F_D}^\dagger D^{i+1}\psi_i](m) \\
&= e^{j2\pi m\xi}(-j2\pi m)^{-(i+1)}[\mathbf{F_D}^\dagger(\delta - 1)](m) \\
&= e^{j2\pi m\xi}(-j2\pi m)^{-(i+1)}(1 - \delta(m))
\end{aligned}$$

where we exploited the translation in frequency theorem, the differentiation in frequency theorem (guaranteed by the periodicity of ψ_i) and (4.5). The impulse $\delta(m)$ implies $[\mathbf{F_D}^\dagger \psi_i](0)$ to be 0. Finally:

$$\mathbf{E}(m,n) \simeq e^{j2\pi m\xi} \sum_{i=\sigma}^{\infty} \chi_{i,n}(\xi)(-j2\pi m)^{-(i+1)} \quad m \notin \mathbb{Z}_M. \quad (4.6)$$

As we predicted in Section 4.2, $\mathbf{E}(m,n)$ entries have been expressed as linear combinations of negative powers of m.

4.3.2 Dependency of Tails on the Column Index

To obtain the coefficients $\chi_{i,n}$ in (4.6), the derivatives $D^i\phi_n$ in (4.3) have to be computed. It can be proven by induction (see Appendix 4.A.2) that the i-th derivative is:

$$D^i\phi_n(f) = e^{-j2\pi n w(f)} \sum_{k=0}^{i} \alpha_{i,i-k}(f)(-j2\pi n \dot{w}(f))^k \quad (4.7)$$

where $\alpha_{i,k}$ is factorized as follows:

$$\alpha_{i,k}(f) = \sum_{l=1}^{|\Omega_k|} \beta_{k,l}(f)\gamma_{k,l}(i). \quad (4.8)$$

$\beta_{k,l}$ is given by:

$$\beta_{k,l} = (Dw)^{\frac{1}{2}} \prod_{m=1}^{k+1} (D^m w)^{p_{k,l,m}} \quad p_{k,l,m} \begin{cases} \in \mathbb{Z}_- & m = 1 \\ \in \mathbb{Z}_+ & m > 1 \end{cases}$$

and $|\Omega_k|$ represents the cardinality of the set of all possible sequences $[p_{k,l,1} \quad p_{k,l,1} \quad \dots \quad p_{k,l,k+1}]$ such that:

$$\sum_{m=1}^{k+1} p_{k,l,m} \cdot m = k. \quad (4.9)$$

A formal demonstration of these statements is reported in Appendix 4.A.3. In Table 4.2 we gave closed expressions of $\beta_{k,l}$ and $\gamma_{k,l}$ for $k = 0, \ldots, 3$. As a convention, $\beta_{k,1}$ is defined as the only function among $\beta_{k,l}$ containing the $k+1$ degree derivative:

$$\beta_{k,1} = (Dw)^{-\frac{1}{2}} D^{k+1} w. \tag{4.10}$$

With the above positions, according to (4.7), we have:

- for $\sigma = 0$ coefficients $\chi_{i,n}$ are given by $D^i\phi_n(\xi^+) - D^i\phi_n(\xi^-)$. In the resulting summation, factors $e^{-j2\pi n w(\xi)}$ and $(-j2\pi n)$ can be extracted.

$$\chi_{i,n}(\xi) = e^{-j2\pi n w(\xi)} \sum_{k=0}^{i} (-j2\pi n)^k \\ (\alpha_{i,i-k}(\xi^+)(\dot{w}(\xi^+))^k - \alpha_{i,i-k}(\xi^-)(\dot{w}(\xi^-))^k). \tag{4.11}$$

- for $\sigma > 0$ we can exploit the factorization (4.8):

$$\chi_{i,n}(\xi) = e^{-j2\pi n w(\xi)} \sum_{k=0}^{i-\sigma} (-j2\pi n \dot{w}(\xi))^k \\ \sum_{l=1}^{|\Omega_k|} (\beta_{i-k,l}(\xi^+) - \beta_{i-k,l}(\xi^-)) \gamma_{i-k,l}(i). \tag{4.12}$$

In (4.12) the summation over k has been considered from 0 to $i - \sigma$ rather than from 0 to i since the function containing the maximum derivative degree $\beta_{i-k,1} = (Dw)^{-\frac{1}{2}} D^{i-k+1} w$ is continue for $k > i - \sigma$.

It is worth to note that, according to (4.6) and (4.12), when $\sigma > 0$ all the information about the warping map, apart from $w(\xi)$ and $\dot{w}(\xi)$ is enclosed in $\beta_{k,l}$. This means that most of the algorithm structure does not depend on the particular shape of the warping maps.

4.3.3 Periodic Repetition of Tails

Now equation (1.11) can be applied to obtain an expression for $\mathbf{A}$. Since coefficients $\chi_{i,n}$ do not depend on m, the summation in (1.11) is applied directly on $m^{-(i+1)} e^{j2\pi m\xi}$:

$$\sum_{k \neq 0} \frac{e^{j2\pi(m-kM)\xi}}{(m-kM)^{i+1}} = e^{j2\pi m\xi} \sum_{k \neq 0} \frac{e^{-j2\pi kM\xi}}{(m-kM)^{i+1}}$$

Table 4.2: Expressions of $\beta_{k,l}$ and $\gamma_{k,l}$ for $k = 0, \dots 3$.

k,l	$\beta_{k,l}$	$\gamma_{k,l}(i)$
0,1	$(Dw)^{1/2}$	1
1,1	$(Dw)^{-1/2} D^2 w$	$1/2\, i^2$
2,1	$(Dw)^{-1/2} D^3 w$	$1/12\,(2i^3 - 3i^2 + i)$
2,2	$(Dw)^{-3/2} (D^2 w)^2$	$1/8\,(i^4 - 4i^3 + 4i^2 - i)$
3,1	$(Dw)^{-1/2} D^4 w$	$1/24\,(i^4 - 4i^3 + 5i^2 - 2i)$
3,2	$(Dw)^{-3/2} D^2 w D^3 w$	$1/24\,(2i^5 - 15i^4 + 37i^3 - 36i^2 + 12i)$
3,3	$(Dw)^{-5/2} (D^2 w)^3$	$1/48\,(i^6 - 12i^5 + 52i^4 - 99i^3 + 82i^2 - 24i)$

and if the following condition is satisfied:

$$M\xi \in \mathbb{N} \tag{4.13}$$

then $e^{-j2\pi k M \xi} = 1$, $k \in \mathbb{Z}$ and the term $e^{j2\pi(m-kM)\xi}$ can be factored out. Equation (4.13) simply means that the singularity must be placed on one of the M points on which the frequency axis is sampled for the computation of $\mathcal{W}_{M,N}$. It is not a restrictive hypothesis, but it has to be taken into account when the warping map is designed. Moreover, since:

$$\frac{1}{(z-k)^{-(i+1)}} = \frac{(-1)^i}{i!} D_z^i \frac{1}{z-k}$$

$$\zeta(z) = \pi \cot(\pi z) - \frac{1}{z} = \sum_{k \neq 0} \frac{1}{z-k} \qquad |z| \leq \frac{1}{2}$$

therefore:

$$\sum_{k \neq 0} \frac{1}{(m-kM)^{i+1}} = \frac{(-1)^i}{M^{i+1} i!} D^i \zeta(m/M).$$

Finally $\mathbf{A}$ can be represented by:

$$\mathbf{A}(m,n) \simeq e^{j2\pi m \xi} \sum_{i=\sigma}^{\infty} \chi_{i,n}(\xi) \frac{(-1)^i}{i!} \frac{(-j2\pi)^{i+1}}{M^{i+1}} D^i \zeta(m/M). \tag{4.14}$$

which completely describes the analytical modeling of aliasing.

4.4 Fast Warping Transforms

In the present Section we deal with the problem of compactly calculating the analytical description which has been previously introduced. Moreover, we cope with the problem of performing the multiplication to the matrix **A** in a fast way, since, according to equation (4.14), a summation of infinite terms is still needed. Furthermore, in case $\xi \in (0, 1/2)$, we will take into account the symmetrical singularity placed in $-\xi$ which is needed for the odd symmetry of the warping map.

4.4.1 Matrix Representation of Aliasing

The results summarized in equations (4.6), (4.14) and (4.11), (4.12) can be arranged in a compact and efficient matrix representation. The coefficients $\chi_{i,n}$, apart from the complex exponential and other factors involving $\dot{w}$, can be seen as difference between the products of a row vector having $\alpha_{i,i-k}$ as entries and a column vector having the powers of n as entries. At this aim, we first introduce a matrix **K** whose generic entry is:

$$\mathbf{K}(i,k) = \begin{cases} \alpha_{i,i-k} & k \le i \\ 0 & \text{otherwise} \end{cases} \qquad i,k = 0,1,\ldots$$

Then, three different contributions are considered: **V**, **N**, **D**. The first matrix contains all the powers of n normalized to $N/2$ so that its entries turn out to be nearly independent on the dimension of the problem:

$$\mathbf{V}(k,n) = \frac{n^k}{(N/2)^k} \qquad n \in \mathbb{Z}_N, k = 0,1,\ldots$$

The other (diagonal) matrixes are introduced to compensate this normalization and account for the powers of $-j2\pi\dot{w}$:

$$\mathbf{N} = \mathrm{diag}\left[(-j\pi N)^k\right] \qquad k = 0,1,\ldots$$
$$\mathbf{D} = \mathrm{diag}\left[\dot{w}^k\right] \qquad k = 0,1,\ldots$$

and have to be multiplied on the left of **V**. By doing so, the dependance of coefficients χ on ξ, apart from the complex exponential factor, is entirely enclosed in matrixes **K** and **D**, which, when evaluated in ξ^+ and ξ^-, will be referred as $\mathbf{K}_{\xi^+}$ and $\mathbf{D}_{\xi^+}$, $\mathbf{K}_{\xi^-}$ and $\mathbf{D}_{\xi^-}$ respectively. As for (4.11) and (4.12), the case

$\sigma > 0$ is only a particular case of the case $\sigma = 0$ where can refer to a single matrix $\mathbf{D}_\xi$ since $\dot{w}(\xi^-) = \dot{w}(\xi^+)$. So, we have:

- for $\sigma = 0$:
$$\mathbf{X} = \mathbf{K}_{\xi^+}\mathbf{D}_{\xi^+} - \mathbf{K}_{\xi^-}\mathbf{D}_{\xi^-}$$
- for $\sigma > 0$:
$$\mathbf{X} = [\mathbf{K}_{\xi^+} - \mathbf{K}_{\xi^-}]\mathbf{D}_\xi.$$

We point out that the first σ lower diagonals of $\mathbf{X}$ starting from the main diagonal are null. Finally we define:

$$\mathbf{Q} = \mathrm{diag}[e^{-j2\pi n w(\xi)}] \qquad n \in \mathbb{Z}_N$$

so that $\chi_{i,n}$ can be calculated as **XNVQ**. It is worth to point out that the input is indexed in $\mathbb{Z}_N$ according to the choice we previously made on the input signal (2.2).

Once $\chi_{i,n}$ is computed, equation (4.6) has to be considered for the computation of $\mathbf{E}$ and equation (4.14) for the computation of $\mathbf{A}$. As far as $\mathbf{E}$ is concerned, we define:

$$\mathbf{Y}(m,i) = \begin{cases} \dfrac{m^{-(i+1)}}{(M/2)^{-(i+1)}} & m \notin \mathbb{Z}_M \\ 0 & \text{otherwise} \end{cases} \qquad i = 0, 1, \ldots$$

together with the following diagonal matrixes to be multiplied on the right and on the left of $\mathbf{Y}$ respectively:

$$\mathbf{M} = \mathrm{diag}[(-j\pi M)^{-(i+1)}] \qquad i = 0, 1, \ldots$$
$$\mathbf{P} = \mathrm{diag}[e^{j2\pi m\xi}] \qquad m \in \mathbb{Z}$$

so that for $\mathbf{E}$ we get the compact expression:

$$\mathbf{E} = \mathbf{PYMXNVQ}.$$

In a similar way, for the operator $\mathbf{A}$ we define:

$$\mathbf{U}(m,i) = \frac{(-1)^i}{2^{i+1}i!} D^i \zeta(m/M) \quad m \in \mathbb{Z}_M,\ i = 0, 1, \ldots$$

so that it results:

$$\mathbf{A} = \mathbf{PUMXNVQ} \tag{4.15}$$

where $\mathbf{P}$ has to be restricted to $\mathbb{Z}_M$ and the output is clearly indexed in $\mathbb{Z}_M$ as well. In Fig. 4.5 some columns of matrix $\mathbf{U}$ for $M = 2^9$ have been depicted.

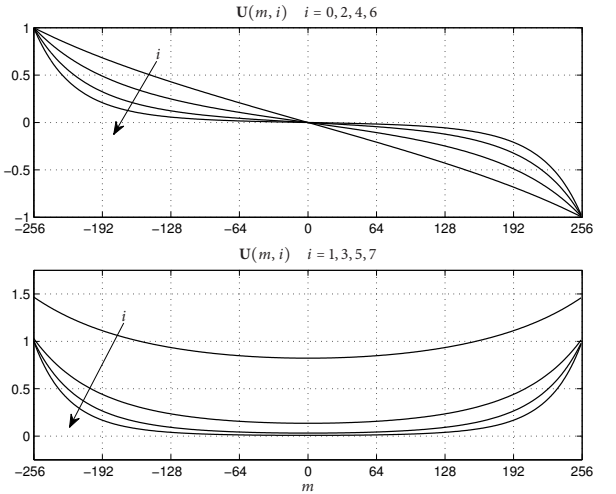

Figure 4.5: Basis vectors $\mathbf{U}(m,i)$, $i = 0,\dots,7$ used to represent the columns of the aliasing matrix $\mathbf{A}$ for $M = 2^9$.

It is worth to note that $\mathbf{P}$ and $\mathbf{Q}$ are diagonal matrixes which perform a scaling action on both input and output signals, while matrixes $\mathbf{M}$ and $\mathbf{N}$ act only as a scaling on matrix $\mathbf{X}$. Moreover, matrices $\mathbf{Y}$, $\mathbf{U}$ and $\mathbf{V}$ do not depend on the warping map and can be precomputed.

4.4.2 Fast Computation

The computation of $\mathbf{A}$ by the decomposition (4.15) still requires an infinite number of operations, since the matrix $\mathbf{X}$ has infinite dimensions. However, if the absolute values of $\mathbf{MXN}$ entries decrease rapidly as the indexes i and k increase, then a finite computation is possible for any prescribed accuracy. In order to verify this condition, let us consider the following product:

$$\mathbf{MKDN} = \mathbf{K} \cdot \mathrm{diag}[\mathbf{M}]\mathrm{diag}[\mathbf{DN}]' = \mathbf{K} \cdot \mathbf{J}$$

where $\cdot$ is the element by element product, the diag operator returns a column vector containing the main diagonal when applied on a matrix, and $\mathbf{J}$ is:

$$\mathbf{J}(i,k) = [\mathrm{diag}[\mathbf{M}]\mathrm{diag}[\mathbf{DN}]'](i,k) = \frac{(-j\pi N\dot{w})^k}{(-j\pi M)^{i+1}}$$

As before, when $\sigma = 0$, $\mathbf{J}_{\xi^+}$ and $\mathbf{J}_{\xi_-}$ represent $\mathbf{J}$ evaluated in ξ^+ and ξ^- respectively. When $\sigma > 0$ we will refer to $\mathbf{J}_\xi$ instead. According to (2.4), $M > N \max \dot{w}$, so that:

$$|\mathbf{J}(i,k)| < 1 \quad i \geq k$$

and the ratio

$$J(f) = \frac{M}{N\dot{w}(f)} > 1 \tag{4.16}$$

represents a sort of redundancy normalized to slope of the map in f. Now we introduce the matrix

$$\mathbf{S} = \mathbf{K}_{\xi^+} \cdot \mathbf{J}_{\xi^+} - \mathbf{K}_{\xi^-} \cdot \mathbf{J}_{\xi^-}$$

whose entries are either real or imaginary:

$$\mathbf{S}(i,k) = \begin{cases} \Re[\mathbf{S}(i,k)] & i-k = 2l+1 \\ \Im[\mathbf{S}(i,k)] & i-k = 2l \end{cases} \qquad l \in \mathbb{Z}. \tag{4.17}$$

Since $\mathbf{K}$ is a lower triangular matrix, it can be shown that $\mathbf{S}(i,k)$ decreases rapidly as i and k increase. When $\sigma = 0$, the main diagonal decays exponentially, while, when $\sigma > 0$, since there are σ null diagonals starting from the main one, the behavior of $\mathbf{S}(i+\sigma, i)$ is evaluated instead. Moreover, among the functions $\beta_{\sigma,l}$, the only one containing the $\sigma+1$-th derivative is $\beta_{\sigma,1}$ (see equation (4.10)). So, we get:

- for $\sigma = 0$:

$$\mathbf{S}(i,i) \propto \frac{\alpha_{i,0}(\xi^+)}{MJ^i(\xi^+)} - \frac{\alpha_{i,0}(\xi^-)}{MJ^i(\xi^-)} \propto \frac{1}{M[J(\xi^+)J(\xi^-)]^i}$$

- for $\sigma > 0$

$$\mathbf{S}(i+\sigma, i) \propto \frac{\alpha_{i+\sigma,\sigma}(\xi^+) - \alpha_{i+\sigma,\sigma}(\xi^+)}{M^{\sigma+1}J^i(\xi)} \propto$$
$$\propto \frac{\gamma_{\sigma,1}(i+\sigma)}{M^{\sigma+1}J^i(\xi)} \propto \frac{i^{\sigma+1}}{M^{\sigma+1}J^i(\xi)}$$

where $\gamma_{\sigma,1}(i+\sigma)$ can be expressed in a closed form:

$$\gamma_{k,1}(i+k) = \frac{2i+k+1}{2(k+1)!} \prod_{l=1}^{k} (i+l) \tag{4.18}$$

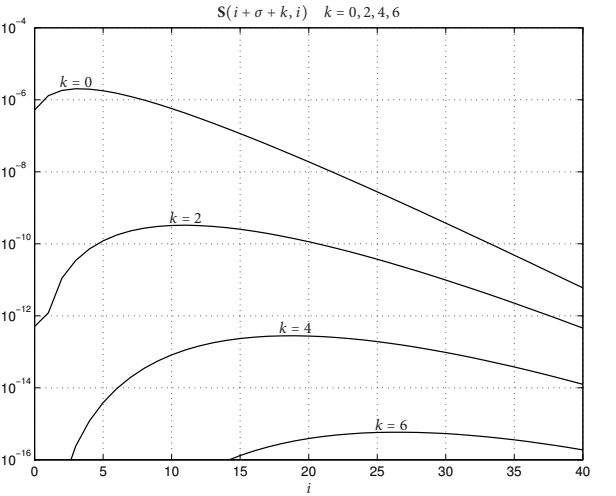

Figure 4.6: Odd diagonals of matrix **S** referred to the warping map of Fig. 2.1 with $N = 2^8$ and $M = 2N$. The decay is exponential as both i and k increases.

as described in Appendix 4.A.4. The first non-zero diagonal has an exponential decay, since it is expressed as the product between a polynomial and a negative exponential. Moreover, the greater is the distance from the main diagonal, the greater the matrix is scaled by an increasing power of M. Non-zero diagonals of **S** referred to the warping map (2.1) are represented in Fig. 4.6.

Thanks to these considerations, matrix **S** can be properly truncated to a $K \times K$ matrix with D non-zero diagonals:

$$\mathbf{S}_{K,D}(i,k) = \begin{cases} \mathbf{S}(i+\sigma,k) & k \le i < k+D \quad i,k < K \\ 0 & \text{otherwise.} \end{cases}$$

and the approximated aliasing matrix $\mathbf{A}_{K,D}$ can be defined as:

$$\mathbf{A}_{K,D} = \mathbf{P}\mathbf{U}_K\mathbf{S}_{K,D}\mathbf{V}_K\mathbf{Q}$$

where the subscript K on **V** represents the truncation to the first K rows:

$$\mathbf{V}_K(k,n) = \begin{cases} \mathbf{V}(k,n) & k < K \\ 0 & \text{otherwise.} \end{cases}$$

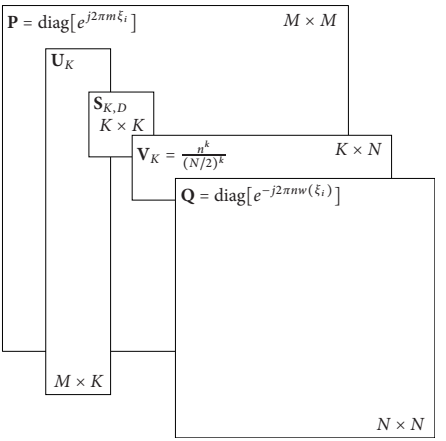

Figure 4.7: Schematic structure of matrix $\mathbf{A}_{K,D}$ factorization. The total amount of multiplications is $\propto K(M + N + D)$, with $K \ll N$, so the resulting algorithm is fast.

while the subscript K on $\mathbf{U}$ represents the truncation to the columns indexed between σ and $\sigma + K - 1$:

$$\mathbf{U}_K(m, i) = \begin{cases} \mathbf{U}(m, i + \sigma) & i < K \\ 0 & \text{otherwise.} \end{cases}$$

A schematization of the factorization of $\mathbf{A}_{K,D}$ has been depicted in Fig. 4.7. Finally, we define the approximated truncated warping matrix:

$$\mathbf{W}_{K,D} = \tilde{\mathbf{W}} - \mathbf{A}_{K,D}.$$

4.4.3 Multiple singularities

In Section 4.3 we analyzed the case of $w \in \mathcal{C}^\sigma$ with only one singularity. This restrictive hypothesis was intended to simplify the mathematical modeling process. If the warping map is designed in a piecewise way, there could be more than one singularity and the resulting map may have different differentiability orders in the neighborhood of each singularity. Nevertheless, the aliasing operator depends on the singularity in a linear way, so the effects of multiple singularities superimpose linearly.

We remind that the warping map $w(f)$ has to be an odd function in order to guarantee that a real signal is transformed into a real signal. If we suppose to have L singularities ξ_l, $l = 1, \ldots, L$, $\xi_l \in (0, 1/2)$ generating the aliasing matrixes $\mathbf{A}^{(\xi_l)}$, then each singularity must have a corresponding dual singularity in $1 - \xi_l$ or equivalently in $-\xi_l$ generating $\mathbf{A}^{(-\xi_l)}$, which can be shown to be equal to $\mathbf{A}^{(\xi_l)*}$. So, the effect of each singularity in $\xi_l \in (0, 1/2)$ is given by:

$$\mathbf{A}^{(\xi_l)} + \mathbf{A}^{(-\xi_l)} = 2\Re[\mathbf{A}^{(\xi_l)}].$$

If present, the singularities in 0 and 1/2 do not have any dual singularities and generate the aliasing matrixes $\mathbf{A}^{(0)}$ and $\mathbf{A}^{(1/2)}$ respectively. So, by superimposing the effects of all potential singularities, it results:

$$\mathbf{A} = \mathbf{A}^{(0)} + \mathbf{A}^{(1/2)} + \sum_{l=1}^{L} 2\Re[\mathbf{A}^{(\xi_l)}]$$

For $\mathbf{A}^{(0)}$ and $\mathbf{A}^{(1/2)}$ some simplifications occur. If $\xi = 0$, both $\mathbf{P}$ and $\mathbf{Q}$ are equal to the identity matrix since $w(0) = 0$, and therefore can be neglected. If $\xi = 1/2$, since $w(1/2) = 1/2$, matrixes $\mathbf{P}$ and $\mathbf{Q}$ just cause a sign inversion on odd indexed input and output entries. In both cases, for the output to be real, $\mathbf{S}$ must have real entries as well. Moreover, the differentiability orders σ_0 and $\sigma_{1/2}$ must be odd, since $D^{\sigma+1}w$ must be an odd function to have a step on $\xi = 0$ or $\xi = 1/2$. Therefore, from equation (4.17), it follows that even diagonals of $\mathbf{S}$ are null.

4.5 Performances

In order to evaluate the accuracy of the proposed algorithm we must introduce a measure of the reconstruction error. As done before, the measure is assumed to be the spectral norm of the reconstruction error matrix, i.e. the maximum its eigenvalue. Therefore, we first consider the error in the ideal case, which is given by operator $\mathbf{W}$ itself:

$$\varepsilon_{\mathbf{W}} = \|\mathbf{W}^{\dagger}\mathbf{W} - \mathbf{I}_N\| = \|\mathbf{E}^{\dagger}\mathbf{E}\|.$$

As the worst case, we consider the error given by operator $\tilde{\mathbf{W}}$, which means no aliasing compensation:

$$\varepsilon_{\tilde{\mathbf{W}}} = \|\tilde{\mathbf{W}}^{\dagger}\tilde{\mathbf{W}} - \mathbf{I}_N\|.$$

Then, we consider the error in approximating the ideal operator $\mathbf{W}^\dagger\mathbf{W}$:

$$\epsilon_{\mathbf{W}_{K,D}} = \|\mathbf{W}^\dagger_{K,D}\mathbf{W}_{K,D} - \mathbf{W}^\dagger\mathbf{W}\|$$

which is intended to check the convergence of the representation introduced for $\mathbf{A}$. This parameter is lower limited by 0 and upper limited by $\epsilon_{\tilde{\mathbf{W}}} = \|\tilde{\mathbf{W}}^\dagger\tilde{\mathbf{W}} - \mathbf{W}^\dagger\mathbf{W}\| \simeq \varepsilon_{\tilde{\mathbf{W}}}$:

$$0 \leq \epsilon_{\mathbf{W}_{K,D}} \leq \epsilon_{\tilde{\mathbf{W}}}.$$

Here we will show that it is not required to make $\epsilon_{\mathbf{W}_{K,D}}$ reach its lower limit. In fact, in order to evaluate performances, we introduce the error $\varepsilon_{\mathbf{W}_{K,D}}$:

$$\varepsilon_{\mathbf{W}_{K,D}} = \|\mathbf{W}^\dagger_{K,D}\mathbf{W}_{K,D} - \mathbf{I}_N\|.$$

such that

$$\varepsilon_{\mathbf{W}} \leq \varepsilon_{\mathbf{W}_{K,D}} \leq \varepsilon_{\tilde{\mathbf{W}}}.$$

For both $\epsilon_{\mathbf{W}_{K,D}}$ and $\varepsilon_{\mathbf{W}_{K,D}}$, the upper limit $\epsilon_{\tilde{\mathbf{W}}} \simeq \varepsilon_{\tilde{\mathbf{W}}}$ is obtained for $K = 0$ and/or $D = 0$ (no aliasing compensation), while the lower limit is theoretically reached for $K, D \to \infty$. Nevertheless, since $\mathbf{S}$ entries decrease exponentially, we expect that $\epsilon_{\mathbf{W}_{K,D}}$ and $\varepsilon_{\mathbf{W}_{K,D}}$ decrease exponentially as well. In particular, $\varepsilon_{\mathbf{W}_{K,D}}$ reaches the target value $\varepsilon_{\mathbf{W}}$ for values of K and D much smaller than N:

$$\begin{aligned}
\varepsilon_{\mathbf{W}_{K,D}} &= \|\mathbf{W}^\dagger_{K,D}\mathbf{W}_{K,D} - \mathbf{W}^\dagger\mathbf{W} + \mathbf{W}^\dagger\mathbf{W} - \mathbf{I}_N\| \\
&\leq \|\mathbf{W}^\dagger_{K,D}\mathbf{W}_{K,D} - \mathbf{W}^\dagger\mathbf{W}\| + \|\mathbf{W}^\dagger\mathbf{W} - \mathbf{I}_N\| \\
&\leq \epsilon_{\mathbf{W}_{K,D}} + \varepsilon_{\mathbf{W}} \qquad (4.19) \\
&\simeq \max[\, \epsilon_{\mathbf{W}_{K,D}}, \varepsilon_{\mathbf{W}} \,]. \qquad (4.20)
\end{aligned}$$

Thus, the truncation of $\mathbf{S}$ turns the complexity from $O(N^2)$ to $O(N)$, like in a truncated Singular Value Decomposition. In fact, the matrix-vector multiplication involving $\mathbf{V}_K$, $\mathbf{S}_{K,D}$ and $\mathbf{U}_K$ requires $K \cdot N$, $K \cdot D$ and $K \cdot M$ multiplications respectively, while the scaling by $\mathbf{P}$ and $\mathbf{Q}$ is computed by $M + N$ multiplications, hence about $K \cdot (N + M + D)$ multiplications are needed.

In order to evaluate the accuracy of the proposed algorithm, we numerically computed the spectral norms $\epsilon_{\mathbf{W}_{K,D}}$ and $\varepsilon_{\mathbf{W}_{K,D}}$ for the frequency warping map (2.1) which belong to $\mathcal{C}^1$, with $\max \dot{w} = 5/4$ for $N = 2^8$ and $M = 2N$.

In Fig. 4.9 we plotted $\epsilon_{\mathbf{W}_{K,D}}$ respect to K and for increasing values of of D. As expected, it decreases exponentially as K

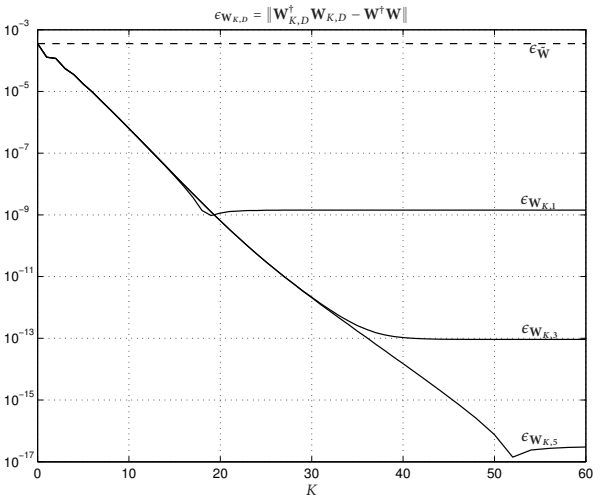

Figure 4.8: Approximation error in representing $\mathbf{W}^{\dagger}\mathbf{W}$ by $\mathbf{W}_{K,D}$. The decrease along D direction is fast, so that small value is required, while a large value of K could be required.

increases till the lower bound corresponding to each value of D is reached. By evaluating the behavior of $\mathbf{S}$, it turns out that, in order to obtain a prescribed accuracy, the value of K depends essentially on the normalized redundancy J (4.16) while the value of D mainly depends on M. In order to represent the operator $\mathbf{W}^{\dagger}\mathbf{W}$ with a double precision accuracy, a considerable value of K would be needed. Nevertheless, since D has a negligible effect on computational cost and K is not affected on N, the complexity is still linear even for large value of K.

From a computational point of view, the target of the proposed model is to compensate aliasing so that the lower bound $\varepsilon_{\mathbf{W}}$ is reached. In Fig. 4.9 we plotted $\varepsilon_{\mathbf{W}_{K,D}}$, the upper bound $\varepsilon_{\mathcal{W}}$, the lower bound $\varepsilon_{\mathbf{W}}$ and the newly introduced upper bound (4.19). So, the error estimation (4.20) is verified to be accurate. In order to reach $\varepsilon_{\mathbf{W}}$, first D has to be set by imposing $\epsilon_{\mathbf{W}_{K,D}} < \varepsilon_{\mathbf{W}}$ for $K \to \infty$, then K is chosen by imposing the same condition by fixing D to the previously set value. An analytical estimation of minimum required K and D would be useful, but this is out of the scope of this paper. In this example by taking $K = 14$ and $D = 1$ the requirement is satisfied. Since only the main diagonal is needed, $\mathbf{S}_{K,1}$ is easily obtained by $\beta_{k,1}$ (4.10) and $\gamma_{k,1}$ (4.18).

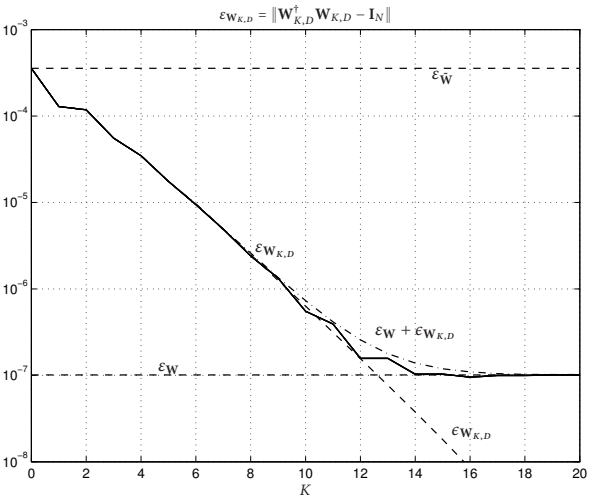

Figure 4.9: Error $\varepsilon_{\mathbf{W}_{K,D}}$ relative to warping map of Fig. 2.1, with $N = 2^8$ and $M = 2N$. By considering a small value of K respect to N and $D = 1$ the lower limit $\varepsilon_{\mathbf{W}}$ is reached. Curves obtained for different D overlaps.

The gain in reconstruction accuracy obtained by aliasing cancelation, the ratio $\varepsilon_{\tilde{\mathbf{W}}}/\varepsilon_{\mathbf{W}}$, can be considerably large. In the considered case the reconstruction error can be decreased by more than 3 degree of magnitudes. Although, the gain in accuracy is strongly dependent on N, M and σ and a detailed study for the estimation of these bounds can be found in the following chapter.

4.6 Conclusions

In this chapter the definition of a mathematical model for the accurate and fast calculation of the aliasing matrix involved in the computation of frequency warping has been treated.

A computational model of the aliasing operator in case of arbitrary shaped non–smooth warping maps has been introduced starting from some experimental observations and a heuristic model. This approach has been shown to be effective since, by applying some proper truncations, it carries a linear complexity without compromising reconstruction accuracy.

Appendix 4.A Mathematical Proofs

4.A.1 Expressions of functions ψ_i

In order to derive the expression of ψ_i, we start by deriving equation (4.4):

$$\begin{aligned} D\psi_i(f) &= H(f)\frac{f^{(i-1)}}{(i-1)!} - \sum_{k=1}^{i+1}\rho_{i+1,k}kf^{k-1} \\ &= H(f)\frac{f^{(i-1)}}{(i-1)!} - \sum_{k=0}^{i}\rho_{i+1,k+1}(k+1)f^{k} \end{aligned}$$

which still matches the definition of ψ_{i-1} by considering:

$$\rho_{i,k} = (k+1)\rho_{i+1,k+1} \quad k = 0, \ldots, i$$

By iteratively applying k times this equation to (4.4) we get:

$$\psi_i(f) = H(f)\frac{1}{i!}f^i - \sum_{k=0}^{i+1}\frac{1}{k!}f^k\rho_{i+1-k} \tag{4.21}$$

where the second subscript has been omitted being equal to 0. Now we impose the functions ψ_i to be periodic, i.e. $\psi_i(0) = \psi_i(1)$:

$$\frac{1}{i!} - \sum_{k=1}^{i+1}\frac{\rho_{i+1-k}}{k!} = 0$$

so that for ρ_i we have:

$$\rho_i = \frac{1}{i!} - \sum_{k=1}^{i}\frac{\rho_{i-k}}{(k+1)!}$$

which, starting from $\rho_0 = 1$, generates the following sequence:

$$1, 1/2, 1/12, 0, -1/720, 0, 1/30240, 0, -1/1209600, \ldots$$

to be used in (4.21) to generate ψ_i functions.

4.A.2 Factorization of $D_f^i\phi_n$

The factorization (4.7) will be demonstrated to be true by induction. To simplify the notation, we set $\mu = -j2\pi nw$. First we verify it is true for $i = 0$:

$$\phi_n = \alpha_{0,0}e^{n\mu} \quad \Rightarrow \quad \alpha_{0,0} = (Dw)^{\frac{1}{2}}.$$

Then, we suppose it is true for $i-1$:

$$D^{i-1}\phi_n = e^{\mu}\sum_{k=0}^{i-1}\alpha_{i-1,i-1-k}(D\mu)^k$$

and try to verify it implies that the factorization is true for i. By deriving the factorization of $D^{i-1}\phi_n$ we get:

$$D\mu e^{\mu}\sum_{k=0}^{i-1}\alpha_{i-1,i-1-k}(D\mu)^k + e^{\mu}D\sum_{k=0}^{i-1}\alpha_{i-1,i-1-k}(D\mu)^k$$

and we try to express it as a polynomial in $D\mu$. For the first term we have:

$$e^{n\mu}\sum_{k=1}^{i}\alpha_{i-1,i-k}(nD\mu)^k$$

while for the second term:

$$e^{\mu}\sum_{k=0}^{i-1}\left[D\alpha_{i-1,i-1-k}(D\mu)^k + \alpha_{i-1,i-1-k}k(D\mu)^{k-1}D^2\mu\right] =$$
$$e^{\mu}\sum_{k=0}^{i-1}\left[D\alpha_{i-1,i-1-k} + \alpha_{i-1,i-1-k}kD^2w(Dw)^{-1}\right](D\mu)^k$$

so that $D^i\phi_n$ has been expressed as a polynomial in $D\mu$ with power from 0 to i, as it was required. Then we impose the expression of coefficients $\alpha_{i,i-k}$. The coefficient of $(D\mu)^i$ is:

$$\alpha_{i,0} = \alpha_{i-1,0} \quad \Rightarrow \quad \alpha_{i,0} = \alpha_{0,0} = (Dw)^{1/2}$$

while the coefficient of $(D\mu)^i$:

$$\alpha_{i,i} = D\alpha_{i-1,i-1}. \tag{4.22}$$

The rest of the coefficients are given in differential form:

$$\alpha_{i,k} - \alpha_{i-1,k} =$$
$$D\alpha_{i-1,k-1} + \alpha_{i-1,k-1}(i-k)D^2w(Dw)^{-1}. \tag{4.23}$$

4.A.3 Expressions of coefficients $\alpha_{i,k}$

We will first demonstrate by induction that α can be factorize as in (4.8). For $k=0$ the factorization is true since $\alpha_{i,0} = (Dw)^{1/2}$.

Then we suppose it is true for $k-1$ and try to verify that it is true for k by exploiting equation (4.23):

$$\alpha_{i,k} - \alpha_{i-1,k} = \sum_{l \in |\Omega_{k-1}|} D\beta_{k-1,l}\gamma_{k-1,l}(i-1) + \sum_{l \in |\Omega_{k-1}|} D^2 w (Dw)^{-1} \beta_{k-1,l}(i-k)\gamma_{k-1,l}(i-1).$$

$D^2 w(Dw)^{-1}\beta_{k-1,l}$ is demonstrated to be a subset of $D\beta_{k-1,l}$:

$$D\beta_{k,l} = \left(\frac{1}{2} - p_{k,l,1}\right) D^2 w (Dw)^{-1}\beta_{k,l} + (Dw)^{\frac{1}{2}-p_{k,l,1}} D \prod_{m=2}^{k+1} (D^m w)^{p_{k,l,m}}$$

then we can collect the two summations in one and represents $\alpha_{i,k} - \alpha_{i-1,k}$ as:

$$\alpha_{i,k} - \alpha_{i-1,k} = \sum_{l \in |\Omega_k|} \beta_{k,l}(f)[\gamma_{k,l}(i) - \gamma_{k,l}(i-1)]$$

which makes the representation (4.8) feasible.

The constraint (4.9) is obtained as follows. Starting from a generic sequence $p_{k-1,\cdot,m} \in \Omega_{k-1}$, a sequence $p_{k,\cdot} \in \Omega_k$ can be generated by the following rule. If the derivative is applied to $D^m w$, then the following sequence is added to $p_{k-1,\cdot,m}$:

$$-\delta(m) + \delta(m+1)$$

so that equation (4.9) becomes:

$$\sum_{m=1}^{k+1} (p_{k,l,m} - \delta(m) + \delta(m+1)) \cdot m = k+1.$$

In order to obtain the actual expressions of β and γ, one has to proceed iteratively. The set of $\beta_{k,l}$ is obtained by deriving $\beta k-1, l$, eliminating multiplicative coefficients and collecting multiple terms, while γ is given in a differential form, so finite difference equations have to be solved.

As an example, we solve the case $k = 1$. We have:

$$\beta_{1,1} = D^2 w (Dw)^{-1/2}$$

and $\gamma_{1,1}$ which is given in differential form:

$$\gamma_{1,1}(i) - \gamma_{1,1}(i-1) = \frac{1}{2}(2i-1).$$

From this equation and from the initial condition (4.22) we get $\gamma_1(0) = 0$, so:

$$\gamma_{1,1}(i) = \frac{1}{2}\sum_{n=1}^{i}(2n-1) = \frac{1}{2}i^2.$$

Successive cases can be solved with the same approach.

4.A.4 Closed expression of polynomial $\gamma_{k,1}$

The iterative equation to be solved in order to find $\gamma_{k,1}$ is simpler than in the general case since it does not involve the term $(i - k) \cdot \gamma_{k-1,1}(i-1)$. So we have:

$$\gamma_{k,1}(i) - \gamma_{k,1}(i-1) = \gamma_{k-1,1}(i-1) \quad k > 1 \tag{4.24}$$

while the condition (4.22) gives:

$$\gamma_{i,1}(i) = \gamma_{i-1,1}(i-1) = \gamma_{1,1}(1) = \frac{1}{2} \tag{4.25}$$

which, substituted in (4.24) evaluated for $k = i$, gives:

$$\gamma_{i,1}(i-1) = 0$$

that implies:

$$\gamma_{k,1}(k-i) = 0 \qquad i = 1, \ldots, k-1$$

which can be demonstrated by induction. In fact, it is true for $i = 1$, then, rewriting equation (4.24), if it is true for i:

$$\gamma_{k,1}(k-i) - \gamma_{k,1}(k-(i+1)) = \gamma_{k-1,1}((k-1)-i) \tag{4.26}$$

the first and the last term are null, so even the second is null.

Equation (4.24) implies that $\gamma_{k,1}(i)$ is a polynomial of degree $k+1$. In facts, $\gamma_1(i)$ is a polynomial of degree 2 and (4.24) represents a finite difference on function $\gamma_{k,1}$. $\gamma_{k,1}$ is an approximation of the integral of $\gamma_{k-1,1}$, hence $\gamma_{k,1}$ is a polynomial of degree equal to degree of $\gamma_{k-1,1}$ plus 1. In order to determine a polynomial of

degree $k+1$ we need at least $k+2$ points. k points are given by the zeros in $i = 0, \ldots, k-1$, and another point is given by (4.25), so we need an additional points. A second condition can be found by considering equation (4.26) for $i = k$:

$$\gamma_{k,1}(-1) = (-1)^{k+1}\frac{1}{2}.$$

So, a general expression for $\gamma_{i,1}$ is obtained by considering a polynomial having zeros in $0, 1, \ldots, k-1$, multiplied for a first degree polynomial having a zero in x and having X as a normalizing constant:

$$\gamma_{k,1}(i) = \frac{2i - x}{2X}\prod_{l=0}^{k-1}(i - l)$$

then, by imposing the two additional conditions, we obtain:

$$\begin{cases} (2k - x)k! = X \\ (2 + x)k! = X \end{cases} \Rightarrow \begin{cases} x = k - 1 \\ X = (k+1)! \end{cases}$$

and finally we get:

$$\gamma_{k,1}(i) = \frac{2i - k + 1}{2(k+1)!}\prod_{l=0}^{k-1}(i - l)$$

from which follows (4.18).

Chapter

5 Frame Bounds Estimation

Warping has been introduced in this work in the framework of unitary operators. This point of view has led the derivation of a time-discrete frequency warping operator as an infinite-dimensional matrix, which, despite of being unitary, could not be used in a practical sense. For these reason, we introduced some finite-dimensional variants which, in order to maintain the capability of recovering the original signal from the transformed one by the application of their adjoints, must produce a redundant output, i.e. a transformed output signal longer than the input one.

Unitary property is a characteristic of *square* operators, since neither the direct transformation nor the adjoint one can be singular. So, the *rectangular* operators which have been described in this work can not be categorized as unitary. Instead, they must be considered in the framework of *frames* [16, 17]. In this theory, the property of being unitary is replaced by the property of being a *tight frame*. The *frame* refers to the fact that, if we consider the adjoint operator composed with the direct one, its maximum and minimum eigenvalues are positive, so that all the eigenvalues are enclosed in the frame determined by the minimum and the maximum one, called frame bounds. The *tight* property takes place when the frame bounds collapse on the same value, so that all the eigenvalues have the same value. Therefore, frame bounds are related to reconstruction accuracy.

Since we deal with operators which are not perfectly inverted by their adjoints, we are now interested in estimating the reconstruction error, or rather, according to the concepts above, the frame bounds.

5.1 Discrete Frames

A complete treatment of frames is out of the scope of this work. Here, we will limit our analysis to discrete frames and to basic concepts which are useful for the evaluation of performances of the considered operators.

We start by considering the eigenvectors and corresponding eigenvalues of the operator $\mathbf{W}_{MN}^{\dagger}\mathbf{W}_{MN}$. Eigenvalues, ordered from the larger to the smaller, will be denoted by:

$$\lambda_0, \lambda_1, \ldots, \lambda_{N-1}$$

while eigenvectors will be denoted by:

$$v_0, v_1, \ldots, v_{N-1}$$

such that:

$$\mathbf{W}_{MN}^{\dagger}\mathbf{W}_{MN}v_i = \lambda_i v_i$$

or equivalently:

$$\det[\mathbf{W}_{MN}^{\dagger}\mathbf{W}_{MN} - \lambda_i \mathbf{I}_N] = 0.$$

The considered operator is square, so, in order to be invertible, its eigenvalues must be strictly positive and limited. When this condition is satisfied by the maximum and the minimum eigenvalues, it is necessarily satisfied by all the eigenvalues, so we just refer to λ_{N-1} and λ_0, which are called frame bounds and conventionally represented by A and B respectively:

$$A = \min \lambda_i = \lambda_{N-1}$$
$$B = \max \lambda_i = \lambda_0$$

and $\mathbf{W}_{MN}$ is a frame when both A and B are positive and limited:

$$0 < A < \infty$$
$$0 < B < \infty.$$

The frame is said to be tight when the ratio B/A is equal to 1, so that $\mathbf{W}_{MN}^{\dagger}\mathbf{W}_{MN}$ is equal to $A\mathbf{I}_N$ or equivalently $B\mathbf{I}_N$.

Now we want to show the effect of having $B/A \neq 1$ on the reconstruction error. Let us suppose to have a generic normalized eigenvector v_i as input vector. By transforming through $\mathbf{W}_{MN}$ and reconstructing by $\mathbf{W}_{MN}^{\dagger}$ we get:

$$\|v_i - \lambda_i v_i\| = \|(1-\lambda_i)v_i\| = |1-\lambda_i|\|v_i\| = |1-\lambda_i|.$$

Obviously the relative error is constant, so the error could be removed by a scaling. Let us consider a generic input obtained as linear combination of the eigenvectors, so that its norm is equal to 1. We suppose that the output is scaled by a value in the interval $[B^{-1}, A^{-1}]$, in particular we choose as value the bounds B^{-1} and A^{-1}. For B^{-1} we have:

$$\sum_{i=0}^{N-1} a_i v_i \mapsto B^{-1} \sum_{i=0}^{N-1} a_i \lambda_i v_i$$

so that, by exploiting eigenvectors orthogonality, the quadratic error is:

$$\sum_{i=0}^{N-1} a_i^2 |1 - B^{-1}\lambda_i|^2. \tag{5.1}$$

The error in the direction of the eigenvector v_0, being $\lambda_0 = B$, is null, while in the direction of λ_{N-1} the error is maximum. Then the worst case arises when $a_i = \delta_{N-1}$ and the maximum error is:

$$\max_{a_i} \left[\sum_{i=0}^{N-1} a_i^2 |1 - B^{-1}\lambda_i|^2 \right]^{1/2} = |1 - A/B|.$$

If the scaling factor is A^{-1}, the worst case gives:

$$\max_{a_i} \left[\sum_{i=0}^{N-1} a_i^2 |1 - A^{-1}\lambda_i|^2 \right]^{1/2} = |1 - B/A|.$$

It can be easily verified that:

$$B/A - 1 \geq 1 - A/B$$

so the error $B/A - 1$ is assumed as worst reconstruction error given by a generic frame when the scaling factor is chosen in $[B^{-1}, A^{-1}]$. This means that the reconstruction error is upper limited when an estimation of frame bounds can be performed.

5.2 Frame Bounds in Frequency Warping

In the case of frequency warping, there is no need of scaling the output, since for $M \to \infty$ the eigenvalues tends to 1, and we surely have:

$$A < 1 \quad B > 1$$

so the maximum error is given by:

$$\max\{1 - A, B - 1\}$$

so, we are not interested in estimating both the frame bounds, but the single one which largely differs from 1.

In chapter 2 we heuristically demonstrated that, in case of non-smooth warping maps, the reconstruction accuracy given by operator $\mathbf{W}_{MN}$ and its frequency sampled variant $\widetilde{\mathbf{W}}_{MN}$ may differ in a significant manner. This preliminary result was confirmed by the example we provided in order to evaluate the performances of the aliasing factorization algorithm. Nevertheless, that example was referred to a single warping map and was considered for a single value of N and M. It would be desirable to be able to foresee the error given by $\mathbf{W}_{MN}$ and $\widetilde{\mathbf{W}}_{MN}$ starting from the input parameters N and M and the warping map only. Then we would be able to compare the two performances in a parameterized form and evaluate the intrinsic advantage of aliasing compensation.

For instance, in figure 5.1 we depicted a set of warping maps corresponding to the same specifications. The slope of the frequency deviation $w(f) - f$ in the first half of the band has to be equal to 6/5, the second half is settled so that the global smoothness results to be equal to a preassigned value σ. In figure 5.2 we plotted matrix $\mathbf{W}_{MN}$ (a) and matrix $\widetilde{\mathbf{W}}_{MN}$ (b) corresponding to the map 5.1 with $\sigma = 1$ for $N = 2^8$ and $M = 2N$.

Hence, here we try to estimate:

$$\varepsilon_{\mathbf{W}}(M, N) = \|\mathbf{W}_{MN}^{\dagger}\mathbf{W}_{MN} - \mathbf{I}_N\| \tag{5.2}$$

$$\varepsilon_{\tilde{\mathbf{W}}}(M, N) = \|\widetilde{\mathbf{W}}_{MN}^{\dagger}\widetilde{\mathbf{W}}_{MN} - \mathbf{I}_N\| \tag{5.3}$$

where, respect to the same error variables defined in chapter 4, we pointed out a dependency on M and N.

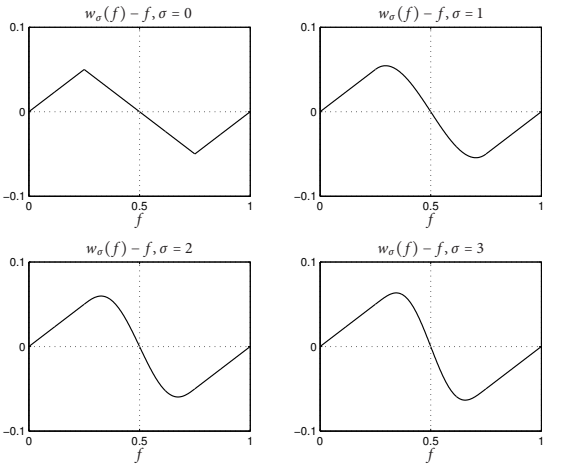

Figure 5.1: Frequency deviation, i.e. $w(f)-f$, of the warping maps used in the for evaluating the performances of the frame bounds estimation. The warping maps are obtained in a piecewise way: in the interval $[0,1/4]$ they are equal to a line of slope 6/5, in the interval $[1/4,1/2]$ they are polynomials of odd powers giving σ continuous derivatives on the singularity point 1/4.

5.3 Error Estimation

The estimation procedure take advantage of the tails matrix and aliasing model which was developed in chapter 4.

As far as (5.2) is concerned, we recall that $\varepsilon_{\mathbf{W}}$ is equal to $\|\mathbf{E}_{MN}^{\dagger}\mathbf{E}_{MN}\|$ and that $\mathbf{E}_{MN}$ can be factorized by (4.15). With proper hypothesis when multiple singularities are considered, we reduce to the following:

$$\varepsilon_{\mathbf{W}} = \|\mathbf{V}^{\dagger}\mathbf{S}^{\dagger}\mathbf{Y}^{\dagger}\mathbf{Y}\mathbf{S}\mathbf{V}\|$$

then $\mathbf{S}$ is substituted by the σ-th lower diagonal, $\mathbf{Y}^{\dagger}\mathbf{Y}$, which is analytically computable and proportional to M, is substituted by the σ-th entry of the main diagonal and the effect of $\mathbf{V}$ is represented by a factor N. Finally we get:

$$\varepsilon_{\mathbf{W}} \simeq \frac{\rho(M/N)}{\pi^{2\sigma+2}(2\sigma+1)} \cdot \frac{N}{M^{2\sigma+1}} \cdot \Delta^2 \tag{5.4}$$

where Δ is the differential value between ξ^+ and ξ^- of $\beta_{\sigma,1}$ (4.10):

$$\Delta = \beta_{\sigma,1}(\xi^+) - \beta_{\sigma,1}(\xi^-)$$

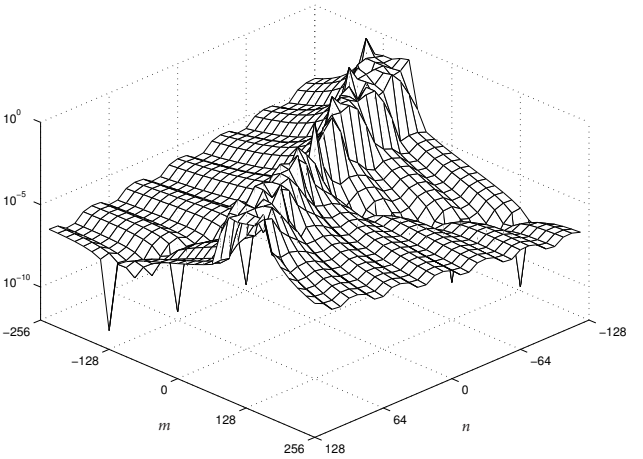

(a) Absolute value of the entries of a truncated warping matrix

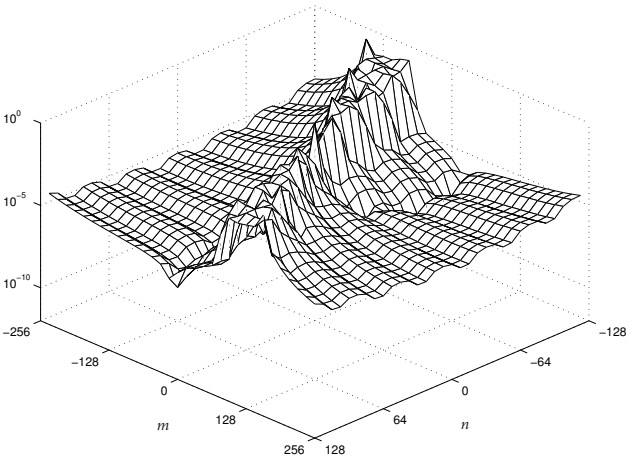

(b) Absolute value of the entries of an aliasing-affected warping matrix

Figure 5.2: Addressed warping operators are depicted, aliasing free (a) and aliasing affected (b). Although the two operators are almost equal, the presence of aliasing in (b) can cause a considerable difference in frame bounds

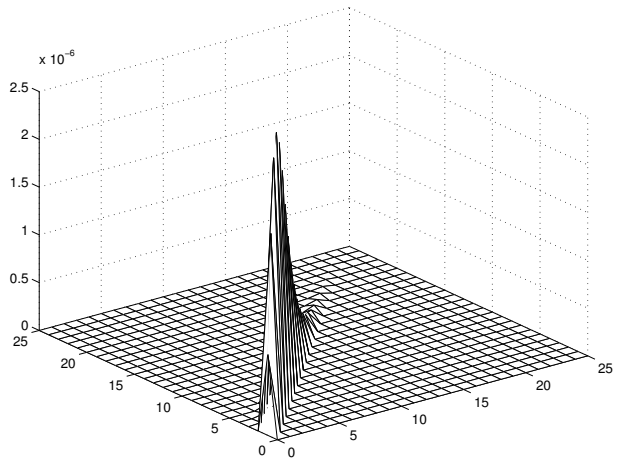

Figure 5.3: Absolute value of matrix **S** entries for $\sigma = 1$, $N = 2^8$ and $M = 2N$. Most of the energy is concentrated along the σ-th lower diagonal.

while ρ is the maximum of the polynomial $\gamma_{\sigma,1}$ (4.18) corresponding to $\beta_{\sigma,1}$ multiplied for a negative exponential having J (4.16) as base:

$$\rho = \max_x \left[J(\xi)^{-x+\sigma} \gamma_{\sigma,1}(x) \right]^2 \tag{5.5}$$

which corresponds to the square maximum of the σ-th lower diagonal of **S** (see fig. 5.3). The expression (5.4) has to be slightly modified in the case $\sigma = 0$. A quasi-exact analytical solution will be provided for ρ, by assuming that the variable x is continuous, although, being a vector index, would be discrete. So we compute the maximum by calculating the value nullifying the first derivative:

$$D\gamma_{\sigma,1}(x) = \gamma_{\sigma,1}(x) \log J$$

The polynomial $\gamma_{\sigma,1}$ has degree equal to $\sigma+1$ and gets an even or odd symmetry if shifted back by $(\sigma-1)/2$. It follows that $\gamma_{\sigma,1}(x+(\sigma-1)/2)$ has either even or odd powers and its derivative can be approximated by:

$$D\gamma_{k,1}\left(x + \frac{\sigma-1}{2}\right) \simeq D\left(x + \frac{\sigma-1}{2}\right)^{\sigma+1} = (\sigma+1)\left(x + \frac{\sigma-1}{2}\right)^{\sigma}$$

and finally we get the following approximated solution:

$$x \simeq \frac{\sigma+1}{\log J} - \frac{\sigma-1}{2}.$$

We point out that, representing a positive index, one has to prevent this solution to become smaller than 0.

In order to estimate $\varepsilon_{\tilde{\mathbf{W}}}$ we take advantage of equation (1.11):

$$\varepsilon_{\tilde{\mathbf{W}}} \simeq 2\|\mathbf{W}_{MN}^{\dagger}\mathbf{A}_{MN}\| = 2\|\mathbf{A}_{MN}^{\dagger}\mathbf{W}_{MN}\mathbf{W}_{MN}^{\dagger}\mathbf{A}_{MN}\|^{1/2}.$$

For $\sigma > 0$ the product $\mathbf{W}_{MN}\mathbf{W}_{MN}^{\dagger}$ can be safely substituted by its main diagonal, whose shape can be analytically derived starting from the warping map. Then the model (4.15) is substituted and it turns out:

$$\varepsilon_{\tilde{\mathbf{W}}} \simeq 2\|\mathbf{V}^{\dagger}\mathbf{S}^{\dagger}\mathbf{U}^{\dagger}\mathbf{C}\mathbf{U}\mathbf{S}\mathbf{V}\|^{1/2} \tag{5.6}$$

where $\mathrm{diag}(\mathbf{C}) = \mathrm{diag}(\mathbf{W}_{MN}\mathbf{W}_{MN}^{\dagger})$. Then only an estimation for $\mathrm{diag}(\mathbf{U}^{\dagger}\mathbf{C}\mathbf{U})$ is needed to trace the estimation of $\varepsilon_{\tilde{\mathbf{W}}}$ back to the form (5.4). Matrix $\mathbf{C}$ has only $N \max Dw$ significant values, so that it actually selects the central values of $\mathbf{U}$ columns, that is $\mathbf{U}(m,k)$ with $m \in \mathbb{Z}_{\lceil N \max Dw \rceil}$. The σ-th entry of $\mathrm{diag}(\mathbf{U}^{\dagger}\mathbf{C}\mathbf{U})$ results to be the energy of $\mathbf{U}(m,\sigma)$ with $m \in \mathbb{Z}_{\lceil N \max Dw \rceil}$, which behaves like a constant in case σ is odd and like m in case σ is even. So energies are proportional to $M^{2\mathrm{mod}_2(\sigma+1)}$:

$$\varepsilon_{\tilde{\mathbf{W}}} \simeq \frac{1}{2}\left(\frac{\rho(M/N)}{\pi^{2\sigma+2}} \cdot \frac{\kappa N}{M^{2(\sigma+1+\mathrm{mod}_2(\sigma+1))}} \cdot \Delta^2\right)^{1/2}. \tag{5.7}$$

In case σ is odd κ is exactly proportional to N according to values of $D^k\zeta(0)$. In case σ is even κ is roughly proportional to N^3 but has to be numerically computed.

The estimations (5.4) and (5.7) have been obtained by imposing the convergence to the exact values for M tending to ∞. So, apart from a possible lack in accuracy for M close to $N \max Dw$, these estimations describe the analytical dependency of the frame bounds on the design variables N, M and σ. Moreover, they allow to evaluate the advantage obtained by using the aliasing free frequency warping operator rather than the frequency sampled one. Finally, the solution of (5.5) allows to estimate the required K to make the computation of the aliasing matrix $\mathbf{A}_{MN}$ converge.

5.4 Experimental Results

To evaluate performances, we consider frequency maps whose frequency deviations are depicted in fig. 5.1. They have a single singularities in $\xi = 1/4$ (a singularity in $\xi = -1/4$ is also present) with different degrees of smoothness:

$$w_\sigma(f) = \begin{cases} \frac{6}{5}f & f \in [0, 1/4] \\ \frac{1}{2} + \sum_{i=0}^{\sigma} a_i (f - \frac{1}{2})^{2i+1} & f \in [1/4, 1/2] \end{cases}.$$

Coefficients a_i are obtained by imposing the first σ derivatives to be null on ξ. N has been fixed to 2^8 and the redundancy M/N varies from its lower allowed value $\max Dw = 6/5$, which is the same for all the considered maps, to the very large value 2^5, to be able to check the asymptotic behavior.

Estimation results are shown in fig. 5.4 for $\widetilde{\mathbf{W}}_{MN}$ and $\mathbf{W}_{MN}$ respectively. The second case is shown to be very accurate while the first case is a bit inaccurate for small M but still converges for large M. As we predicted when the approximation (5.6) has been done, the model completely fails for $\widetilde{\mathbf{W}}_{MN}$ when $\sigma = 0$. The considered maps represent a bad case in the sense that the slope of w on the singularity is equal to the maximum slope. Having a smaller slope on the singularity improves the estimation accuracy.

As a concluding remark, we can state that gain obtained by aliasing compensation is proved by the fact the following approximated relationship holds:

$$\varepsilon_{\widetilde{\mathbf{W}}} \sim \varepsilon_{\mathbf{W}}{}^{1/2}$$

which was also heuristically foreseen in chapter 2.

5.5 Conclusions

We dealt with the problem of frame bounds estimation for frequency warping operators of non-smooth warping maps. We gave estimations formulas for both the aliasing affected and the aliasing free form of the frequency warping operator. The estimations are proven to be effective and can be used for designing warping operators satisfying specific requirements in reconstruction accuracy.

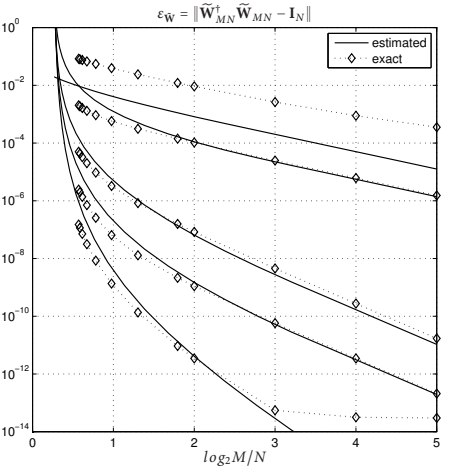

(a)

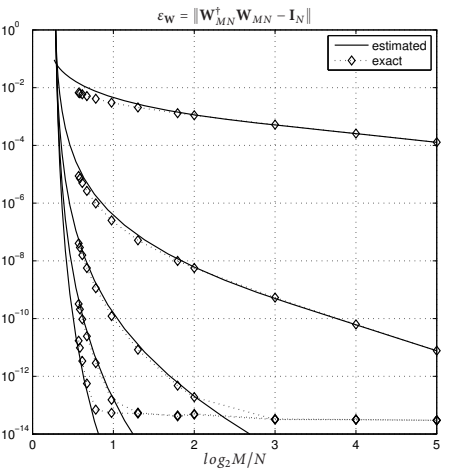

(b)

Figure 5.4: Error norm estimations (solid line) and computed error norms (diamonds) of the frequency sampled warping operator (a) and of the truncated warping operators (b) for $\sigma = 0, \ldots, 4$. Computed norms obviously saturates to a lower computational limit.

Part

III

Applications on Ultrasound Signals

Chapter

6 Ultrasonic Guided Waves Characterization

Guided Waves (GWs) have characteristic dispersive time-frequency representations (TFRs). Unfortunately, any TFR is subjected to the time-frequency uncertainty principle. This, in general, limits the capability of TFRs to characterize multiple, closely spaced guided modes from a time transient measurement, over a wide frequency range. To overcome this limitation, we present here a new warped frequency transform (WFT) that in force of a more flexible tiling of the time frequency domain presents enhanced modes extraction capabilities. Such tiling is chosen to match the dispersive spectro-temporal structure of the waveguide by selecting an appropriate map of the time frequency plane. The proposed transformation is fast, invertible, and covariant to group delay shifts. In particular, in this chapter we describe design and calculation strategies for maps tailored to Lamb waves propagating in an aluminium plate. Time-transient guided wave propagation events obtained both artificially and experimentally are considered. The results show that the proposed WFT limits interference patterns which appears with others TFRs and produces a sparse representation of the Lamb waves pattern that can be suitable for identification and characterization purposes.

6.1 Introduction to Guided Waves

Guided Waves (GWs) are mechanical-stress waves that can propagate along solids of finite dimension (waveguides). In a certain waveguide (a plate, a rod, a rail) one or more stress GWs can propagate at a given excitation frequency. Each of these waves has a characteristic dispersive behavior based on which its speed of propagation depends on the frequency. The representation of the wave's speed versus frequency is generally referred as *dispersion curves*. From a practical point of view, dispersion generates nonstationary signals as a function of time (time-waveforms) if the waveguide is excited by a force with multiple frequency content. These signals, in fact, change their shape while propagating since the several excited waves components have different speed. Characterization of the dispersion curves from time-transient measurements is vital to all the GWs based applications that are becoming nowadays a common practice in the industry for nondestructive evaluation, material characterization, acoustic focusing and advanced material design.

As proposed in [23] dispersion curves can be obtained by processing multiple time-waveforms, acquired at equally spaced positions along the waveguide, by using the two-dimensional Fourier transform (2D-FT). However, this technique needs multiple signals from closely-spaced locations. This drawback limits the practicality of the 2D-FT procedure for industrial applications.

GWs dispersion curves can be also extracted from a single recorded time-waveform. This step is in general attempted by means of time-frequency representations (TFRs) [24].

Unfortunately, any TFR is subjected to the time-frequency (TF) uncertainty principle [25] that limits the capability of distinguishing multiple, closely spaced guided modes. In fact each TFR decomposes the TF plane in atoms whose resolution is bounded by $\Delta_T \Delta_F \geq 1$, where Δ_T is time duration and Δ_F spectral or frequency bandwidth.

The various TF plane decomposition strategies (*tilings*) characterize the different transforms. For example in Fig. 6.1(a) and 6.1(b) are depicted the tilings of the Short-Time Frequency Transform (STFT), with constant shape atoms in the TF plane, and those of the Wavelet transform (WT), characterized by a multiscale resolution. Processing a time waveform via a TFR produces a complex coefficient for each atom of the TF plane.

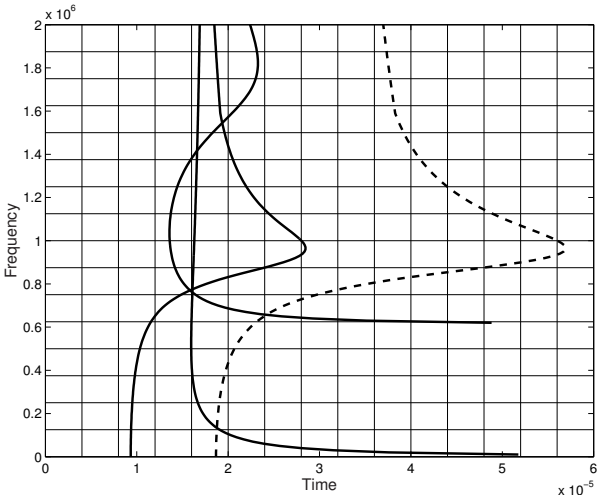

(a)

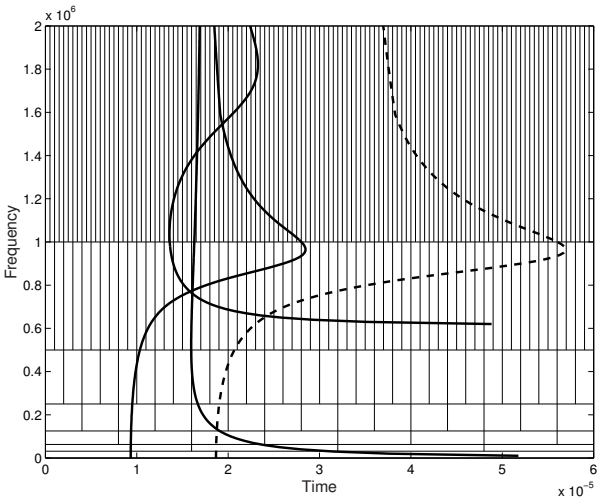

(b)

Figure 6.1: Tiling of the TF plane for the STFT (a), and for the WT (b). The superimposed thicker continuous lines represent sample dispersion curves for the waveguide studied in Section 6.3 projected in the TF plane considering a distance source-receiver of 50 mm. The dashed line corresponds to only one of the modes projected in TF plane considering a path length of 100 mm from the source to the receiver.

The squared values of these coefficients are generally represented in contour maps. These maps for the STFT and the WT are known as *spectrogram* and *scalogram*, respectively. In Fig. 6.1(a) and 6.1(b) the predicted multimodal and dispersive behaviour of the guided waves studied in Section are superimposed as a thicker lines. As it can be seen from Fig. 6.1(a) and 6.1(b) neither the fixed STFT resolution nor the Wavelet multiscale resolution are suited to finely estimate the dispersion curves because of their atoms are poorly correlated to the complex behavior of guided waves. In particular, they generate interference patterns in the TF plane when more than one mode exists in a TF atom.

As suggested by different authors [26] [27] the readability of spectrograms and scalograms can be enhanced by means of the *reassignment* method that improves the TFR resolution by concentrating the atom's energy at its center of gravity. However this technique is particularly sensitive to the presence of noise and multi-component interferences.

More flexible TFRs can be obtained with either Wavelet Packet [28] or Chirplet [29] [30] transforms which are able to adapt the spectro-temporal resolution to the characteristics of the acquired time-waveform. Yet, these procedures still have two major shortcomings: (i) they cannot track fast non-linear frequency modulations; (ii) they are not group delay shift covariant. This latter drawback in particular, requires, to set a proper time-frequency tiling, knowledge of the distance traveled by the guided waves. In other words, if this distance is unknown or if unexpected reflections atoms' are present whitin the signal, the resolution may be inadequate (see Fig. 6.2).

Other strategies to extract the dispersion curves contemplate the TF energy distributions, such as the Wigner Ville distribution [31]. These transforms are superior to correlation-based methods (such as the STFT), but their applications are limited by the existence of cross-term interference. In addition, their computational cost is onerous.

With the intention to overcome some of the highlighted problems of TFRs, we implemented a new Warped Frequency Transform (WFT) with enhanced capabilities. The proposed WFT is fast, invertible and covariant to group velocity shifts. The key point of the proposed WFT is its tiling, composed by non-linearly frequency modulated atoms, designed to match the spectro-temporal structure of the different guided waves. Such tiling is obtained by selecting an appropriate warping map to

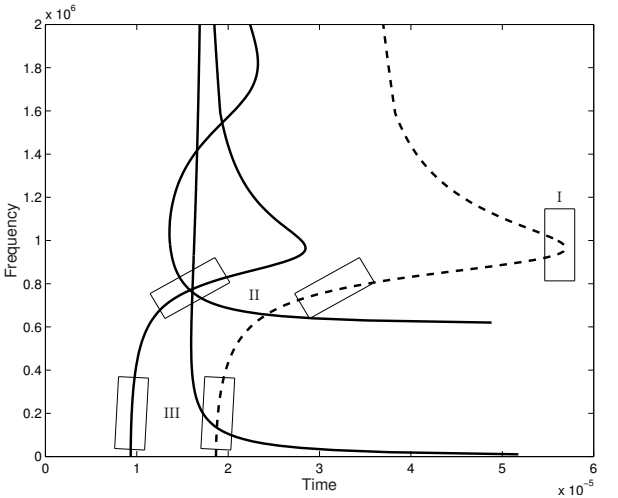

Figure 6.2: The slope of Chirplet atoms axes can be set either manually or with automated procedures (*matching pursuits* algorithms [30]). This degree of freedom can be effectively exploited for guided waves analysis. However, some problems arise: i) Case I represents the poor correlation we may have between a chirplet atom and the mode time-frequency behavior; ii) Case II shows that the correct slope for a dispersive mode at a given distance is ever more inadequate when the distance traveled increases; iii) adaptive automated procedures could overcome this problem but are unable to handle situations like Case III in which different slopes must be selected to discriminate the modes.

reshape the frequency axis. The map can be designed once the dispersion curves for the considered waveguide can be predicted for the frequency range of interest. The capabilities of the WFT in comparison with other TFRs are shown here considering an application on guided waves propagating in an isotropic aluminum plate.

6.2 Dispersion-matched Warpograms

6.2.1 Group Delay Shifts Covariance

The group delay is defined as the derivative of signal's phase response and it is a measure of time delay introduced in each sinusoidal component. TFRs are classified as Group Delay Shifts Covariant (GDSC) when the TFR of a signal s which undergoes

a change $\tau(f)$ in the group delay ($s \rightarrow s_{disp}$) corresponds to the TFR of the original signal shifted by $\tau(f)$:

$$\mathbf{F}s_{disp} = S_{disp}(f) = e^{-j2\pi \int \tau(f)df} \cdot S(f) \tag{6.1}$$

$$TFR[s_{disp}](t,f) = TFR[s](t - \tau(f), f) \tag{6.2}$$

It was shown in [32] that a GDSC representation can be obtained by warping a signal and then analyzing it by a TFR of the Cohen class, such as the Short-Time Frequency Transform (STFT), if:

$$K\frac{dw^{-1}(f)}{df} = \tau(f) \tag{6.3}$$

where K is an arbitrary constant. Therefore, it is possible to design a GDSC TFR, appropriate for a given dispersive system, by setting the derivative of the inverse warping map $w^{-1}(f)$.

6.2.2 Application to Stress Guided Waves

If $c_g(f)$ is the dispersive group velocity relation for the mode we want to analyze, the group delay we must consider is $\tau(f) = D/c_g(f)$, where D is the distance traveled by the acoustic wave from the actuator. Therefore, in our approach, the warping map is designed according to the dispersive relation:

$$K\frac{dw^{-1}(f)}{df} = \frac{1}{c_g(f)} \tag{6.4}$$

and the constant K is assumed so that $w(0.5) = 0.5$. Next, a GDSC time frequency representation (TFR_W), that we call *warpogram*, is obtained with the following transformation:

$$TFR_W[s_{disp}](t,f) = STFT[\mathcal{W}s_{disp}\,](tKc_g(f), w^{-1}(f)) \tag{6.5}$$

Generally speaking, first the signal is warped in frequency, then a Short-Time Fourier Transform is performed (alternative TFRs can be considered at this point), and finally the warped axes are reparametrized to provide the correct time-frequency alignment. It is worth to notice that the compensation of the dispersive effects acts independently from the distance D, which, in facts, does not appear in (6.4), i.e. the formula used for map design.

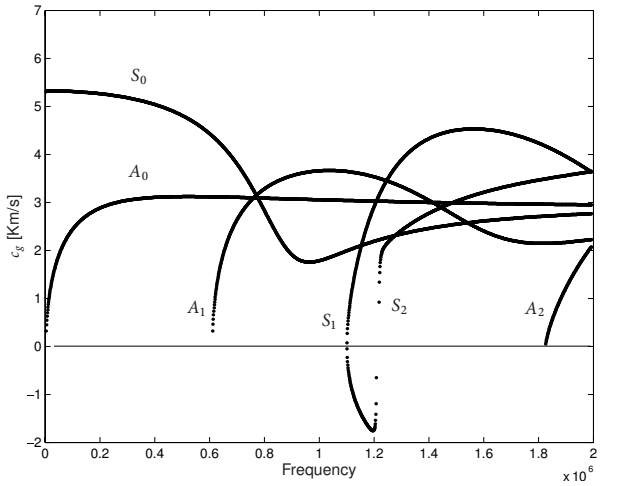

(a)

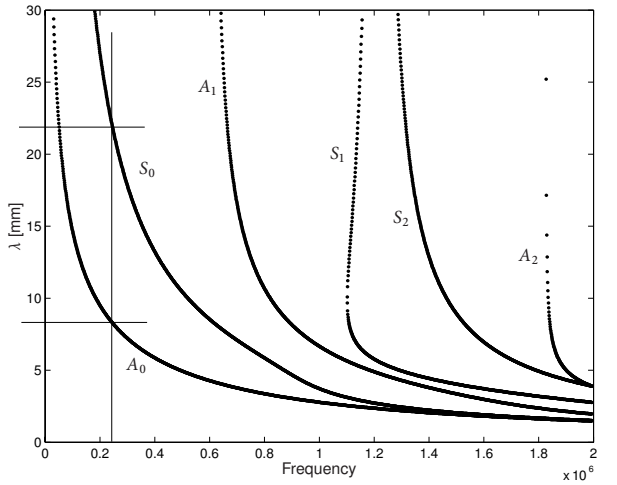

(b)

Figure 6.3: Lamb waves dispersion curves for an aluminum 2.54 mm - thick plate. (a) group velocity $c_g(f)$, (b) wavelength $\lambda(f)$.

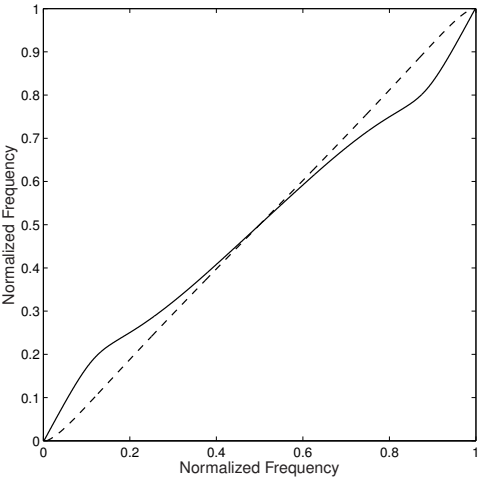

Figure 6.4: Warping maps designed according to (6.4): by using the S_0 mode $c_g(f)$ (continuous line) and A_0 mode $c_g(f)$ (dashed line).

6.2.3 Group Velocity Dispersion Curves

The analysis method formulated in (6.5) is based on the group velocity dispersion curve $c_g(f)$ of a particular guided wave. Such curve can be predicted for the considered waveguide by using analytical, semi-analytical or pure numerical formulations [33, 34]. In particular, for a given frequency in input, the wave equation formulated as in [33] provides the wavelengths, i.e. the phase velocity, and the group velocity of all the existing guided waves. For example, in Fig. 6.3(a) and (b) are represented the dispersion curves in terms of group velocity $c_g(f)$ and wavelength $\lambda(f)$, respectively, for the Lamb waves existing in the $[0 \div 2]$ MHz frequency range for a $h = 2.54$ mm thick aluminium plate (Young modulus $E = 69$ GPa, Poisson's coefficient, $\nu = 0.33$, density $\rho = 2700$ kg/m^3). These curves were obtained by using the semi-analytical Finite Element (SAFE) formulation proposed in [33].

As clearly shown, in the considered frequency range, up to six waves can exist, namely the fundamental A_0 and S_0 waves, and four higher order waves. Below 600 kHz only the two fundamental waves can propagate.

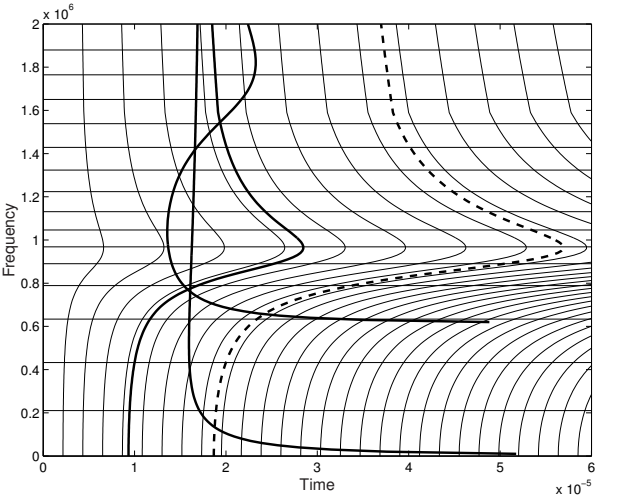

(a)

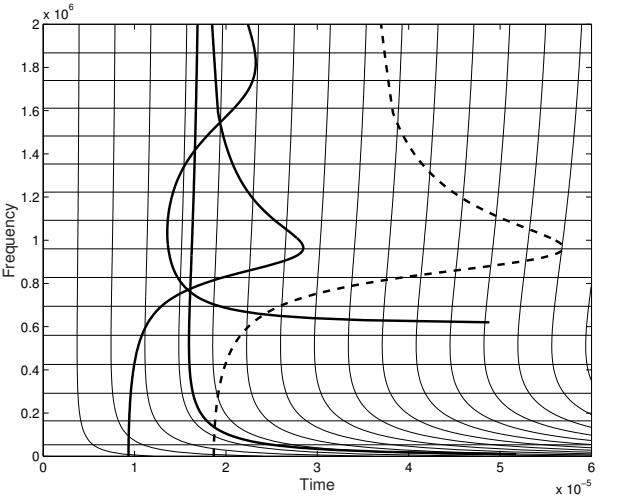

(b)

Figure 6.5: Tiling of the time-frequency plane produced by using the warping map designed on the S_0 group velocity dispersion curve (continuous line of Fig. 6.4) and on the A_0 group velocity dispersion curve (dashed line of Fig. 6.4).

6.2.4 Warping maps and Warpograms

The predicted $c_g(f)$ branches are used to design the warping maps according to Eq. (6.4). In Fig. 6.4, where these maps for the A_0 and S_0 are plotted, it can be seen that just a slight bending of the frequency axis is required.

In Fig. 6.5(a) the tiling of the time-frequency plane shaped according to the warping map for the S_0 wave (continuous line in Fig. 6.4), is presented. It is worth noting how the atoms inclination varies in frequency following closely the mode dispersive behavior. This guarantees to the warpogram enhanced sparsify if compared to the others TFRs. In addition, the atoms change their shape versus time in agreement to the dispersive properties of the mode as clearly visible in Fig. 6.5(a) for a distance source-receiver of 50 mm (continuous line) and 100 mm (dashed line). This allows to the warpogram the desired group covariant property. Similar considerations can be drawn on the tiling built on the A_0 mode warping map (dashed line in Fig. 6.4) shown in Fig. 6.5(b).

A case study on the signal s_{disp}, represented in Fig. 6.6(a) and Fig. 6.7(a), is proposed. This signal was generated synthetically by imposing the group delay shift of the modes depicted in Fig. 6.1 to a Dirac Delta. In Fig. 6.6 are shown the steps used to obtain the Warpogram of s_{disp} tuned on the S_0 mode. The warping effect can be clearly seen in Fig. 6.6(b). Roughly speaking, a guided wave whitin a signal is approximatively reconverted into the incipient pulse (i.e. the Dirac Delta) at a distance from the origin which is proportional to the distance traveled by the mode, thus compensating the mode dispersive behavior. For instance, the two delta in Fig. 6.6(b) correspond to the S_0 mode at 100 mm distance (continuous line in Fig. 6.1) and at 200 mm distance (dashed line in Fig. 6.1), respectively. This important effect can be also fruitfully exploited for defect localization procedures [35]. Processing the signal $\mathcal{W}s_{disp}$ with the STFT yields the Fig. 6.6(c) that is next converted to the warpogram of Fig. 6.6(d) by reparametrizing the axes to provide the corred time frequency alignment. As it can be seen from Fig. 6.6(d) the WFT produces a sparse representation of the acquired signals. It is worth to notice that the mode acquired repeatedly is sparsely represented in both cases (as warpograms are GDSC). Similar considerations can be made for the Warpogram tuned on the mode A_0, for the dispersive signal s_{disp}, in Fig. 6.7(d).

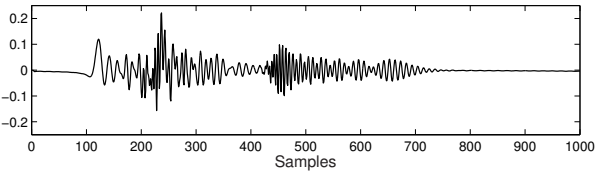

(a) Acquired signal: s_{disp}

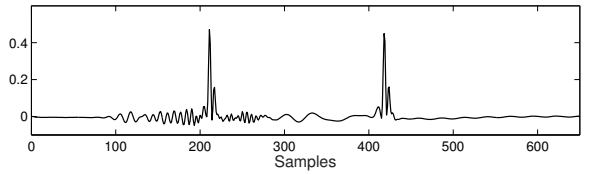

(b) Warped signal: $\mathcal{W}s_{disp}$

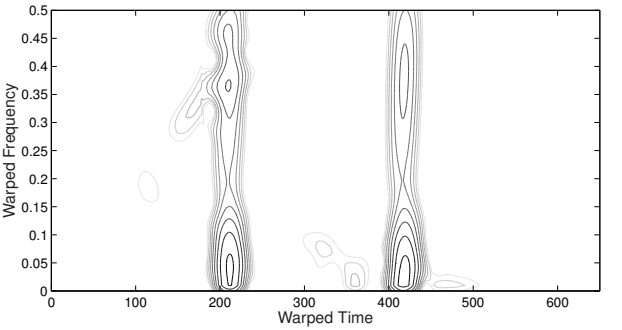

(c) Spectrogram of the warped signal:$STFT(\mathcal{W}s_{disp})$

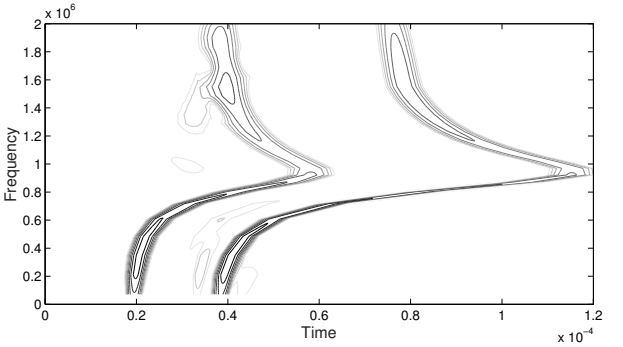

(d) Warpogram: $STFT(\mathcal{W}s_{disp})(tKc_g(f), w^{-1}(f))$

Figure 6.6: Warpogram calculation steps as described in Section 6.2.4. The depicted Warpogram is calibrated to extract the S_0 mode from the synthetic signal of Fig. 6.1.

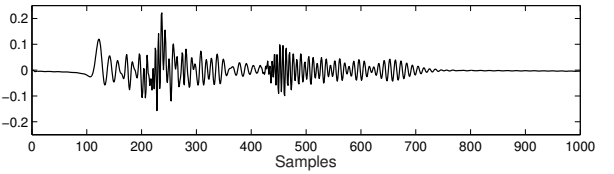

(a) Acquired signal: s_{disp}

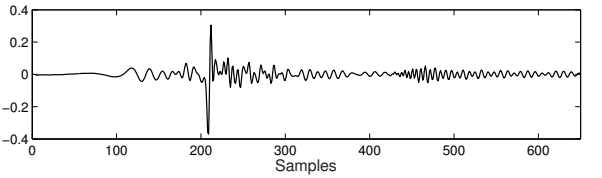

(b) Warped signal: $\mathcal{W}s_{disp}$

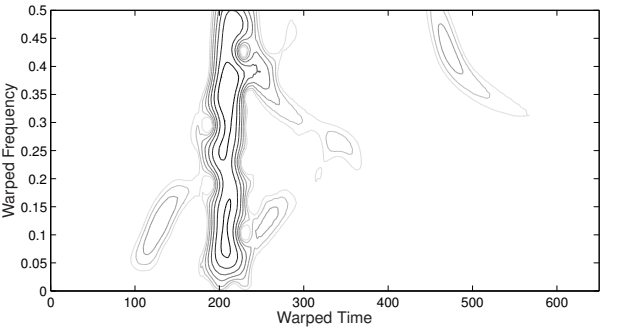

(c) Spectrogram of the warped signal: $STFT(\mathcal{W}s_{disp})$

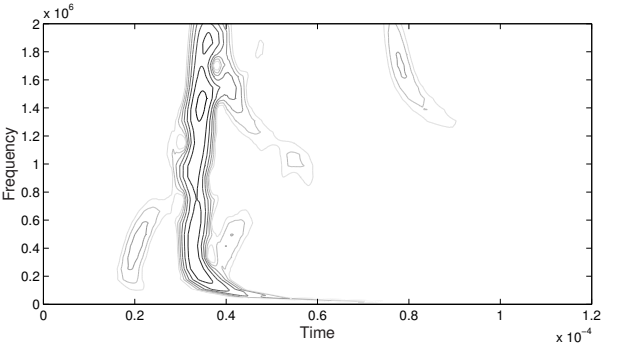

(d) Warpogram: $STFT(\mathcal{W}s_{disp})(tKc_g(f), w^{-1}(f))$

Figure 6.7: Warpogram calculation steps as described in Section 6.2.4. The depicted Warpogram is calibrated to extract the A_0 mode from the synthetic signal of Fig. 6.1.

6.3 Numerical and Experimental Results

6.3.1 Finite Element simulation results

A transient Finite Element analysis with a commercial software is carried out to simulate Lamb waves propagating in an isotropic plate. The effectiveness of conventional finite element packages for modeling elastic waves propagating in structural components has been shown in the past [36].

The three dimensional wave propagation problem is reduced to a bidimensional one by assuming a plane strain condition. An isotropic aluminum plate of length 1220 mm and thickness 2.54 mm has been considered. The aluminum properties have been taken as those used in section 6.2.3. Lamb waves were excited by imposing an inclined concentrated unitary force $P(t)$, acting on the left hand edge of the plate.

The force has been shaped in time as a triangular window with total duration equal to 0.7 μs to excite consistent Lamb waves up to 1.5 MHz. In order to satisfy the requirements for simulation accuracy, the integration time step was set equal to 0.02 μs and the plate was discretized by using linear 4-node plate elements of dimension 0.25×0.254 mm [36]. In Fig. 6.8 the out-of-plane displacement $u(t)$, occurring at a point on the top side of the plate located at 150 mm away from the left edge, is represented. This time-waveform is next used to test the suitability of the WFT in comparison with other TFRs. For example, the spectrogram and the scalogram of the time-waveform $u(t)$ are shown in Fig. 6.9(a) and 6.9(b), respectively. As it can be seen from these figures, the finite time-frequency resolution produces interference patterns and limits the capability of distinguishing closely spaced Lamb modes.

This is particular evident for both TFRs at about 700 kHz where the fundamental A_0 and S_0 modes cross each other. In addition, it can be seen that the scalogram presents lower capability to distinguish the energy content of different waves at very low frequency due to its poor time resolution.

In order to extract the energy content of the S_0 mode from the signal $u(t)$ via the proposed WFT, first the warping map must be set. Next, the application of Eq. (6.5) gives the warpogram tuned on the S_0 mode as represented in Fig. 6.9(c). It can be seen from this figure that the S_0 mode is well captured all over the excited frequency range, while the A_0 mode, as desired,

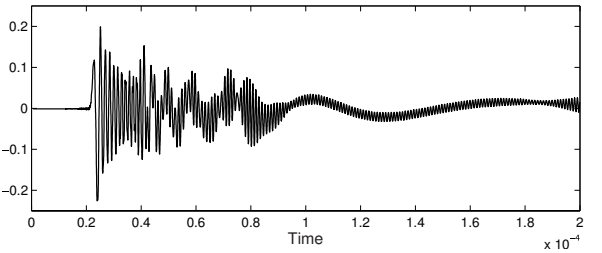

Figure 6.8: Time-waveform $u(t)$ extracted for further TFR post-processing.

is barely visible. Similarly, shaping the map on the dispersion curve of the A_0 mode and applying the proposed GDSC TFR, yields the warpogram of Fig. 6.9(d). Also the A_0 mode is well defined in this plot, even if in this case the presence of the S_0 mode is still consistent. This is true in particular in the frequency range where both the A_0 and S_0 modes have low dispersive behavior, for which the maps designed via Eq. (6.4) present similar aspects.

6.3.2 Experimental results

Experimental tests were carried out to generate and detect Lamb wave propagating in an aluminum plate 2.54 mm thick. A Q-switched Nd:YAG pulsed laser operating at 1064 nm with an 8 ns pulse duration was used to excite the plate. The laser beam, through conventional optics, was focused to deliver a 30 × 0.5 mm line normally to the plate surface. The line source was created to effectively generate directional and broadband guided waves propagating perpendicular to the line with minimum geometrical spreading. To enhance the signal-to-noise ratio, ablative generation conditions were produced by applying a layer of water to the plate irradiated area [37], [38]. A broadband surface-bonded piezoelectric sensor (PWAS) of $d = 14$ mm diameter was used to detect the propagating Lamb waves 300 mm away from the illuminated spot. The ultrasonic signals were amplified by using Panametrics pre-amp set at 40 dB connected to an oscilloscope and sampled at 20 MHz. In Fig. 6.11(a) and 6.11(b) the spectrogram and the scalogram of the experimental signal are shown, respectively. Instead, in Fig. 6.11(c) and

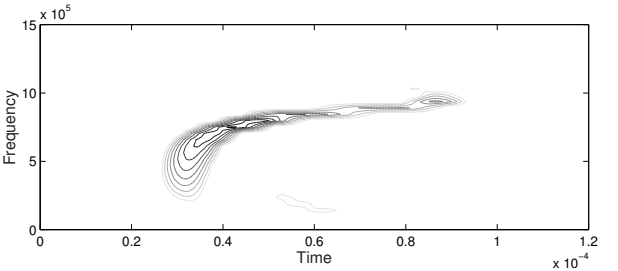

(a) Spectrogram of $u(t)$

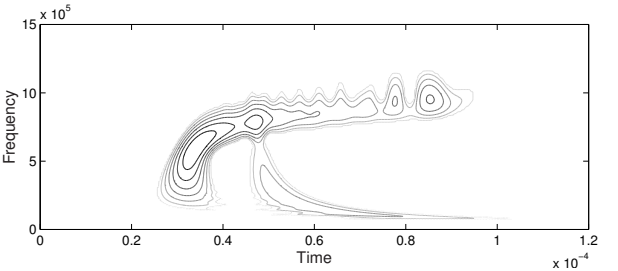

(b) Scalogram of $u(t)$

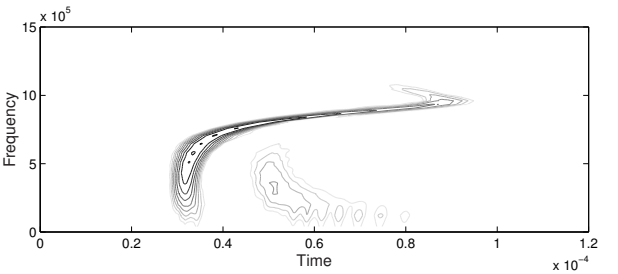

(c) Warpogram of $u(t)$ calibrated on the S_0 mode

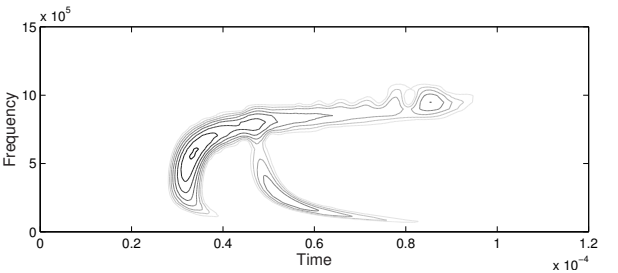

(d) Warpogram of $u(t)$ calibrated on the A_0 mode

Figure 6.9: Spectrogram, scalogram and warpograms of the experimental signal $u(t)$.

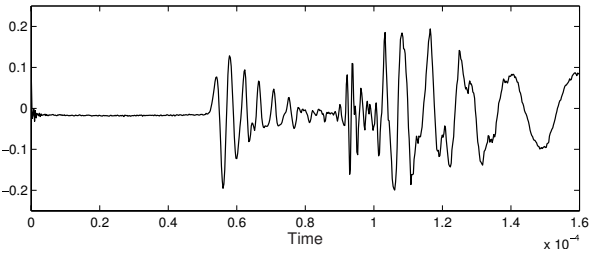

Figure 6.10: Experimental signal $e(t)$.

6.11(d) the warpograms tuned on the S_0 and A_0 group velocity dispersion curves are presented.

It can be seen from Fig. 6.11(c) and 6.11(d), where the theoretical SAFE dispersion curves are overlapped with the contour maps obtained from both the S_0 and A_0 warpogram, the benefit of the proposed WFT. In fact, as it can be seen by comparing them with Fig. 6.11(a) and 6.11(b), classical TFRs barely reveal the presence of the fundamental modes, while warpograms clearly extract the energy content of both S_0 and A_0 modes. For characterization purposes, where the extraction of the dispersion modes is crucial, the sparse representation of the WFT limiting the interference patterns can yield to consistent results in a broaded frequency range if compared to others TFRs. The appealing energy mode extraction over a wide frequency range, as the one obtained in Fig. 6.9(c) and 6.9(d) for the numerical signal, is here partially lost due to the finite dimension of the adopted sensor. In fact, due to the *wavelength tuning* effect the sensor output is maximum when the sensor diameter d equals an odd multiple of half the Lamb wave wavelength $\lambda/2$ and minimum when it equals an even multiple of the half wavelength [39]. Some energy maxima emerges in the TF plane since several Lamb modes, each with its own different wavelength, coexist at the same time. Fig. 6.11(c) and 6.11(d) show the remarkable fact that, at 250 kHz, the amplitude of the A_0 mode goes through zero, while that of the S_0 is close to its peak. At this frequency, in fact, as it can be seen in Fig. 6.3(b) the A_0 mode has a wavelength around 8 mm while the S_0 mode approximately 22 mm.

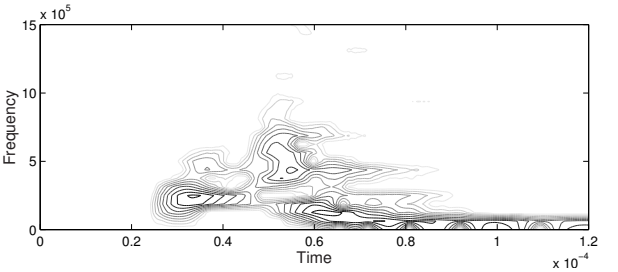

(a) Spectrogram of $e(t)$

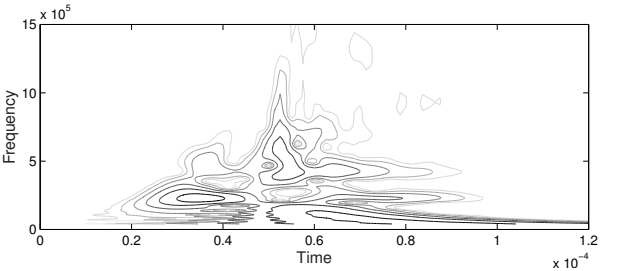

(b) Scalogram of $e(t)$

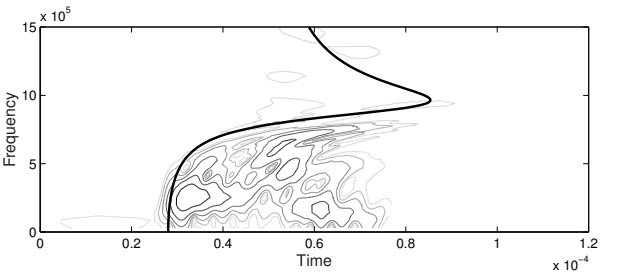

(c) Warpogram of $e(t)$ calibrated on the S_0 mode

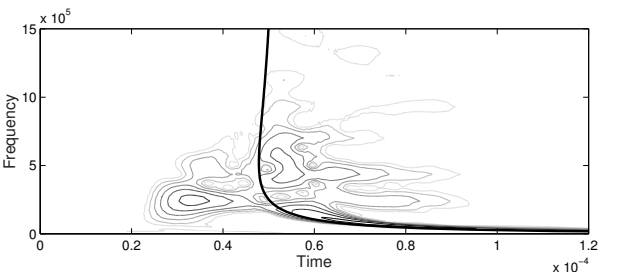

(d) Warpogram of $e(t)$ calibrated on the A_0 mode

Figure 6.11: Spectrogram, scalogram and warpograms of the experimental signal $e(t)$.

6.4 Conclusions

In this chapter we presented a new TFR matched to the time-frequency structures of Lamb waves. The new tool efficiently represents the different GWs with non-linearly frequency modulated atoms. An application to propagating GWs in a single layer isotropic aluminum plate was presented to show the potential of the proposed procedure. Transient events obtained from both dedicated finite element (FEM) simulations and experimentally were considered to prove the reliability of the new tool. The main difference from the experimental numerical and FEM based signals was due to the effect of a finite dimension transducer, revealing the so called wavelength tuning effect in the experimental signals.

In general, the results showed that: i) the WFT produces a sparser representation of a particular guided wave pattern that can be suitable for identification and characterization purposes; ii) the energy peaks extraction is a simpler task and can be performed to obtain reliable mode representation; iii) the quality of the energy peaks extraction is independent on the distance waves source - waves receiver, thanks to the group velocity covariant property. In conclusion the WFT thanks to its suitable time-frequency support can be considered a powerful tool for the analysis of dispersive systems.

Conclusions

Frequency warping has been presented in this work in the framework of time–frequency transformations. First, operators related to frequency warping have been recalled focusing on the problems of perfect reconstruction and flexible design. Then, some computational issues have been treated, such as the definition of a mathematical model for the accurate and fast calculation of the considered transforms. Finally, a promising application of frequency warping on ultrasonic waves propagation has been presented.

More in details, we accurately introduced frequency warping starting from continuous Fourier operators and then performing sampling operations on time and frequency axis. By doing so, frequency warping operators for discrete-time signals have been identified as well. The design procedure has been guided by the attempt to make them satisfy the unitary property. Nevertheless, it turned out that this unitary property is not feasible for a practical use, so new operators belonging to the class of frames have been considered.

As far as the computation is concerned, we presented an algorithm for the fast calculation of nonuniform Fourier transform, which is directly employed in the calculation of the frequency sampled frequency warping, and an algorithm for the fast calculation of compensating the aliasing which occurs in the frequency sampled frequency warping because of the sam-

pling operation. This algorithm has been theoretically and experimentally shown to be effective in eliminating aliasing and increasing the reconstruction accuracy.

Finally, a possible innovative application of warped time-frequency techniques has been shown. In particular, we focused on the capability of frequency warping analysis techniques to match the physical characteristics of the propagation of guided waves. In fact, through the employment of frequency warping a sparser representation of guided wave patterns have been obtained, which can be usefully exploited for features extraction and propagation characterization.

Bibliography

[1] B. de Smit and H. Lenstra Jr., "The mathematical structure of escher's print gallery," *Notice of the AMS*, vol. 50, pp. 446–451, 2003.

[2] M. Vetterli and J. Kovacevic, *Wavelets and Subband Coding*. Prentice Hall PTR, April 1995.

[3] G. Strang and T. Nguyen, *Wavelets and Filter Banks*. Wellesley College, 1996.

[4] A. Papandreou-Suppappola, R. Murray, B.-G. Iem, and G. Boudreaux-Bartels, "Group delay shift covariant quadratic time-frequency representations," *Signal Processing, IEEE Transactions on*, vol. 49, no. 11, pp. 2549–2564, Nov 2001.

[5] S. Franz, S. K. Mitra, and G. Doblinger, "Frequency estimation using warped discrete fourier transform," *Signal Processing*, vol. 83, no. 8, pp. 1661 – 1671, 2003.

[6] R. Baraniuk and D. Jones, "Unitary equivalence: a new twist on signal processing," *IEEE Trans. Signal Processing*, vol. 43, no. 10, pp. 2269–2282, 1995.

[7] G. Evangelista and S. Cavaliere, "Discrete frequency warped wavelets: theory and applications," *IEEE Trans. Signal Processing*, vol. 46, no. 4, pp. 874–885, 1998.

[8] G. Evangelista, "Dyadic warped wavelets," *Advances in Imaging and Electron Physics*, vol. 117, pp. 73–171, 2001.

[9] A. Oppenheim and D. Johnson, "Discrete representation of signals," *Proc. IEEE*, vol. 60, no. 6, pp. 681–691, 1972.

[10] A. Makur and S. Mitra, "Warped discrete-fourier transform: Theory and applications," *Circuits and Systems I: Fundamental Theory and Applications, IEEE Transactions on*, vol. 48, no. 9, pp. 1086–1093, Sep 2001.

[11] U. Laine and T. Altosaar, "An orthogonal set of frequency and amplitude modulated (FAM) functions for variable resolution signal analysis," in *Proc. IEEE International Conference on Acoustics, Speech, and Signal Processing*, Albuquerque, NM, 1990, pp. 1615–1618.

[12] A. Dutt and V. Rokhlin, "Fast fourier transforms for nonequispaced data," *SIAM Journal on Scientific Computing*, vol. 14, no. 6, pp. 1368–1393, 1993.

[13] Q. Liu and N. Nguyen, "An accurate algorithm for nonuniform fast fourier transforms (NUFFT's)," *IEEE Microwave Guided Wave Lett.*, vol. 8, no. 1, pp. 18–20, 1998.

[14] ——, "The regular Fourier matrices and nonuniform fast Fourier transforms," *SIAM Journal on Scientific Computing*, vol. 21, no. 1, pp. 283–293, Jan. 1999.

[15] J. Fessler and B. Sutton, "Nonuniform fast fourier transforms using min-max interpolation," *IEEE Trans. Signal Processing*, vol. 51, no. 2, pp. 560–574, 2003.

[16] R. Duffin and A. Schaeffer, "A class of nonharmonic fourier series," *Trans. Amer. Math. Soc.*, pp. 341Ű–366, 1952.

[17] I. Daubechies, "The wavelet transform, time-frequency localization and signal analysis," *IEEE Trans. Inform. Theory*, vol. 36, no. 5, pp. 961–1005, 1990.

[18] S. Caporale, L. De Marchi, and N. Speciale, "An accurate algorithm for fast frequency warping," in *Proc. IEEE International Symposium on Circuits and Systems*, 2007, pp. 1811–1814.

[19] ——, "Analytical computation of fast frequency warping," in *Proc. IEEE International Conference on Acoustics, Speech and Signal Processing*, 2008, pp. 3793–3796.

[20] ——, "Fast operators for arbitrary warping maps," in *Proc. IEEE International Symposium on Circuits and Systems*, 2008.

[21] ——, "A SVD-based algorithm for dense nonuniform fast fourier transform," in *Proc. EURASIP European Signal Processing Conference*, 2007, pp. 2120–2125.

[22] M. Do and M. Vetterli, "The contourlet transform: an efficient directional multiresolution image representation," *IEEE Trans. Image Processing*, vol. 14, no. 12, pp. 2091–2106, 2005.

[23] D. Alleyne and P. Cawley, "A two-dimensional Fourier transform method for the measurement of propagating multimode signals," *J. Acoust. Soc. Am.*, vol. 89, p. 1159, 1991.

[24] W. Prosser, M. Seale, and B. Smith, "Time-frequency analysis of the dispersion of Lamb modes," *The Journal of the Acoustical Society of America*, vol. 105, p. 2669, 1999.

[25] A. Papoulis, *Signal analysis*. McGraw-Hill New York, 1984.

[26] M. Niethammer, L. Jacobs, J. Qu, and J. Jarrzynski, "Time-frequency representations of lamb waves," *J. Acoust. Soc. Am.*, vol. 109(5), pp. 1841–1847, 2001.

[27] O. Kotte, M. Niethammer, and L. J. Jacobs, "Lamb wave characterization by differential reassignment and nonlinear anisotropic diffusion," *NDT & E International*, vol. 39, pp. 96–105, 2006.

[28] S. Mallat and Z. Zhang, "Matching pursuits with time-frequency dictionaries," *IEEE Trans. Signal Process.*, vol. 41, no. 12, pp. 3397–3415, 1993.

[29] H. Kuttig, M. Niethammer, S. Hurlebaus, and L. J. Jacobs, "Model-based analysis of dispersion curves," *J. Acoust. Soc. Am.*, vol. 119, pp. 2122–2130, 2006.

[30] A. Raghavan and C. Cesnik, "Guided-wave signal processing using chirplet matching pursuits and mode correlation for structural health monitoring," *Smart Materials and Structures*, vol. 16, no. 2, p. 355, 2007.

[31] T. Claasen and W. Mecklenbrauker, "The Wigner distributionŮa tool for time-frequency signal analysis. II. Discrete time signals," *Philips Jl Research*, vol. 35, pp. 276–300, 1980.

[32] A. Papandreou-Suppappola, R. Murray, B. Iem, and G. F. Boudreaux-Bartels, "Group delay shift covariant quadratic time-frequency representations," *IEEE Trans. Signal Process.*, vol. 49, no. 11, pp. 2549–2564, 2001.

[33] I. Bartoli, A. Marzani, F. Lanza di Scalea, and E. Viola, "Modeling wave propagation in damped waveguides of arbitrary cross-section," *Journal of Sound and Vibration*, vol. 295, pp. 685–707, 2006.

[34] A. Marzani, "Time-transient response for ultrasonic guided waves propagating in damped cylinders," *International Journal of Solids and Structures*, vol. 45, no. 25-26, pp. 6347 – 6368, 2008.

[35] L. De Marchi, A. Marzani, S. Caporale, and N. Speciale, "A defect localization procedure based on warped lamb waves," in *Accepted to Proc. International Symposium on Acoustical Imaging*, 2009.

[36] I. Bartoli, F. Lanza di Scalea, M. Fateh, and E. Viola, "Modeling guided wave propagation with application to the long-range defect detection in railroad tracks," *NDT and E International*, vol. 38, pp. 325–334, 2005.

[37] S. Wooh and Q. Zhou, "Behavior of laser-induced ultrasonic waves radiated from a wet surface. Part I. Theory," *Journal of Applied Physics*, vol. 89, p. 3469, 2001.

[38] ——, "Behavior of laser-induced ultrasonic waves radiated from a wet surface. Part II. Experimental work," *Journal of Applied Physics*, vol. 89, p. 3478, 2001.

[39] F. Lanza di Scalea, H. Matt, and I. Bartoli, "The response of rectangular piezoelectric sensors to Rayleigh and Lamb ultrasonic waves," *J. Acoust. Soc. Am.*, vol. 121, p. 175, 2007.